10-16-2012 12:00 AM

Development of a Novel Handheld Device for Active Compensation of Physiological Tremor

Abhijit Saxena
The University of Western Ontario

Supervisor
Dr. Rajni V. Patel
The University of Western Ontario

Graduate Program in Electrical and Computer Engineering
A thesis submitted in partial fulfillment of the requirements for the degree in Master of Engineering Science

Recommended Citation

Saxena, Abhijit, "Development of a Novel Handheld Device for Active Compensation of Physiological Tremor" (2012). *Electronic Thesis and Dissertation Repository*. 914.
https://ir.lib.uwo.ca/etd/914

Development of a Novel Handheld Device for Active Compensation of Physiological Tremor

(Spine title: A Handheld Device for Active Compensation of Physiological Tremor)

(Thesis format: Monograph)

by

Abhijit Saxena

Graduate Program in Electrical and Computer Engineering

A thesis submitted in partial fulfillment
of the requirements for the degree of
Master of Engineering Science

The School of Graduate and Postdoctoral Studies
The University of Western Ontario
London, Ontario, Canada

THE UNIVERSITY OF WESTERN ONTARIO
School of Graduate and Postdoctoral Studies

CERTIFICATE OF EXAMINATION

Supervisor	Examiners
Dr. Rajni Patel	Dr. Ken McIsaac
	Dr. Shaun Salisbury
	Dr. Samuel F. Asokanthan

The thesis by

Abhijit Saxena

entitled:

Development of a Novel Handheld Device for Active Compensation of Physiological Tremor

is accepted in partial fulfillment of the
requirements for the degree of
Master of Engineering Science

Date	Chair of the Thesis Examination Board

Abstract

In microsurgery, the human hand imposes certain limitations in accurately positioning the tip of a device such as scalpel. Any errors in the motion of the hand make microsurgical procedures difficult and involuntary motions such as hand tremors can make some procedures significantly difficult to perform. This is particularly true in the case of vitreoretinal microsurgery. The most familiar source of involuntary motion is physiological tremor. Real-time compensation of tremor is, therefore, necessary to assist surgeons to precisely position and manipulate the tool-tip to accurately perform a microsurgery. In this thesis, a novel handheld device (AID) is described for compensation of physiological tremor in the hand. MEMS-based accelerometers and gyroscopes have been used for sensing the motion of the hand in six degrees of freedom (DOF). An augmented state complementary Kalman filter is used to calculate 2 DOF orientation. An adaptive filtering algorithm, band-limited multiple Fourier linear combiner (BMFLC), is used to calculate the tremor component in the hand in real-time. Ionic Polymer Metallic Composites (IPMCs) have been used as actuators for deflecting the tool-tip to compensate for the tremor.

Keywords

microsurgery, physiological tremor, active handheld device, inertial measurement unit, tremor modeling, Kalman filter, adaptive filtering technique, Ionic Polymer Metallic Composites (IPMCs)

Acknowledgments

I would like to express my foremost gratitude to my supervisor Dr. Rajni Patel for his guidance, support, patience and encouragement throughout my graduate studies and during writing of this thesis. I would also like to thank him for the opportunity to work on an exciting project. The brainstorming sessions during the research will always be remembered for many years to come.

I would like to thank my colleagues at Canadian Surgical Technologies and Advanced Robotics for their suggestions and assistance. In particular, I would like to thank Christopher Ward and Abelardo Escoto for their assistance in the fabrication of the device.

I would also like to thank my friend Anand Gupta for his constant encouragement during the course of this research. I also want to mention my friends at Western in providing motivation throughout my studies.

Special thanks to my brother, Dr. Ashutosh Saxena for providing valuable suggestions and motivating me throughout the course of the thesis.

Finally, I wish to express my deepest gratitude to my family for their constant support, belief and encouragement.

Dedicated to

my father, Dr. Anand Prakash

and

my uncle, Shailesh Chandra

Table of Contents

List of Tables

List of Figures

List of Appendices

List of Acronyms

AID:	Accuracy Improvement Device
ACKF:	Augmented State Complementary Kalman Filter
ADC:	Analog to Digital Converter
BMFLC:	Bandlimited Multiple Fourier Linear Combiner
CM:	Capacitive Method
DAC:	Digital to Analog Converter
DBS:	Deep Brain Simulation
DOF:	Degrees of Freedom
EAC:	Electroactive Ceramic
EAP:	Electroactive Polymer
EM:	Electromagnetic
ERI:	Environmental Robots Inc.
ET:	Essential Tremor
FFT	Fast Fourier Transform
FLC:	Fourier Linear Combiner
GUI:	Graphic User Interface
IMU:	Inertial Measurement Unit
INSTAR:	INertially Stabilized Rifle
IPMC:	Ionic Polymer Metallic Composite

IR:	Infrared
IRS:	Inertial Reticle System
LED:	Light Emitting Diode
LPF:	Low Pass Filter
MEMS:	Microelectromechanical Systems
NEAT:	New England Affiliated Technologies
PD:	Parkinson's Disease
PZT:	Lead Zirconate Titanate
RAMS:	Robot Assisted Microsurgery
RF:	Radio Frequency
rms	Root-mean Squared
SHR:	Steady Hand Robotic System
SMA:	Shape Memory Alloy
US:	Ultrasound
WFLC:	Weighted-frequency Fourier Linear Combiner
w.r.t	with respect to

List of Symbols

y_a	Vector containing the total acceleration sensed by the tri-axial accelerometer
y_g	Vector containing the total angular rate sensed by the gyroscopes
${}^{G1}y_g$	Vector containing the signals measured by the gyroscope, IDG500
${}^{G2}y_g$	Vector containing the signals measured by the gyroscope, MLX90609
${}^{B}A$	Vector containing the linear acceleration w.r.t frame $\{B\}$
${}^{B}\tilde{A}$	Vector containing the acceleration w.r.t frame $\{B\}$ due to tremor and noise
${}^{S}A$	Vector containing the acceleration at the needle tip
${}^{S}\tilde{A}$	Vector containing the acceleration w.r.t frame $\{S\}$ due to tremor and noise
${}^{S}A_{tremor}$	Vector containing the acceleration at the needle tip due to tremor
${}^{B}G$	Vector containing the gravity force w.r.t frame $\{B\}$
${}^{W}G$	Vector containing the gravity force w.r.t frame $\{W\}$
g	Acceleration due to gravity (9.804 m/s^2)
${}^{B}\omega$	Vector containing the angular velocity w.r.t frame $\{B\}$
${}^{B}\tilde{\omega}$	Vector containing the angular velocity w.r.t frame $\{B\}$ due to tremor and noise
${}^{B}\omega'$	Vector containing the angular velocity about X_B and Y_B axes
${}^{B}\alpha$	Vector containing the angular acceleration w.r.t frame $\{B\}$

${}^{W}R_{B}$	Rotation matrix describing the orientation of frame $\{B\}$ w.r.t frame $\{W\}$
ϕ	Angular rotations about X_B axis (roll)
θ	Angular rotations about Y_B axis (pitch)
φ	Angular rotations about Z_B axis (yaw)
Ψ	Vector containing the angular rotations about X_B, Y_B and Z_B axes
Θ	Vector containing the angular rotations about X_B and Y_B axes
${}^{B}P_{tip}$	Position of frame $\{S\}$ w.r.t frame $\{B\}$
${}^{S}P_{tremor}$	Position of needle tip w.r.t frame $\{S\}$ due to tremor
b	Vector containing the varying gyro bias in dual-axis gyroscope, IDG 500
b_0'	Constant gyro bias in single-axis gyroscope, MLX 90609
x	State vector
A	State transition matrix
Q	Process noise covariance matrix
z	Measurement vector
H	Measurement matrix
R	Measurement noise covariance matrix
P	Projected error covariance
$\tilde{K}$	Kalman gain
${}^{C}P$	Control input to IPMC controller

${}^{C}V$	Voltage needed by IPMC actuator to deflect the needle tip
${}^{C}\tilde{V}$	Voltage to IPMC actuator; limited to ±3.6V
K	Transformation factor in IPMC controller
T	Sampling time

Chapter 1

1 Introduction

Human tremor is an involuntary motion of body part(s) that is associated with both healthy individuals and individuals having movement disorders. For individuals suffering with movement disorders, tremor leads to degrading the quality of life. Mundane tasks such as lifting a cup are significantly difficult for such individuals. Essential tremor, Parkinson's disease and cerebellar lesion are the leading cause of movement disorders. Tremor in healthy individuals is known as physiological tremor. It puts a limitation on positional accuracy of tasks requiring motion in sub-millimeter range.

Physiological tremor is intrinsic to all healthy individuals. It degrades the performance of procedures which require micromanipulation such as military targeting, photography and microsurgery. In the latter, even small amounts of tremor can be fatal for the patient. A high degree of positional accuracy (in the range of microns) is required to effectively perform such tasks.

There are various approaches for compensating tremor. These include medication or surgical procedures depending on the severity of the tremor and the side-effects associated with each treatment modality. Pharmacological treatments have varying success in reducing the tremor and surgical approaches are invasive, costly and can impose harmful side-effects. In addition, various assistive devices such as external damping devices, prosthetic devices, telerobotic systems or active handheld devices exist which suppress pathological tremor or cancel or filter out physiological tremor. External damping devices, prosthetic devices and telerobotic systems suffer from bulky size, high cost and less user acceptance. On the other hand, active handheld devices have advantages such as portability, low cost and high user acceptance.

A hand-held device for active tremor cancellation is a promising solution; however, it is difficult to implement due to various strict constraints on weight, size, frequency range and stroke of actuators. Overcoming these constraints involves the right combination of actuators and sensors. Conventional actuators and sensors cannot be used as they are relatively heavy and bulky in size for small and compact applications. Smart materials, particularly, Ionic Polymer Metallic Composites (IPMCs) present a viable solution as they can be manufactured in small sizes and are light in weight along with the capability to produce high speed cyclic motion. IPMCs, however, have certain limitations, such as low force output, which must be resolved before they can be effectively employed as actuators.

Thus, the goal of this thesis project was to develop an active hand-held device which can measure and compensate for physiological tremor in the surgeon's hand during microsurgery and enhance the accuracy of performing a microsurgical procedure.

1.1 Tremor

Tremor is defined as a rapid back-and-forth undesired movement of a body part. It is intrinsic to all humans, both healthy and those having movement disorder as a pathological symptom [1].

1.1.1 Sources of Tremor

Motion of any body part is produced by muscles. Muscles are connected to the central nervous system through reflex loops. Muscles contain muscle spindles which are made up of fibers sensitive to changes in length. Whenever there is a change in length, they produce a signal which is fed to the reflex loops. Reflex loops carry the signals from the muscle spindles to the central nervous system where they are processed and signals are sent back to the muscles using the reflex loops.

Figure 1.1 shows the influence of the central nervous system on the muscles through these loops. In [1] and [2], it was reported that tremor has three sources: mechanical, reflex and central oscillations.

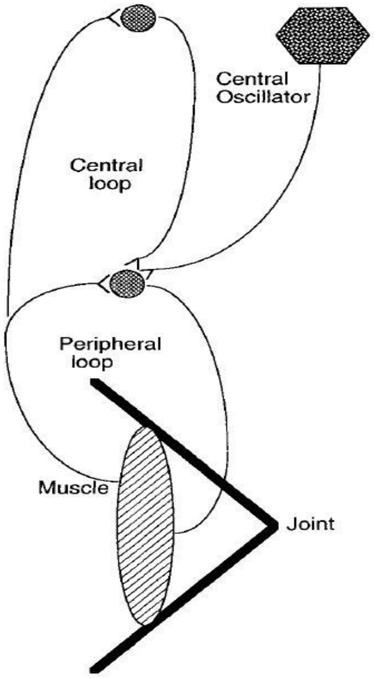

Figure 1.1: Influence of central nervous system on a limb [2] (Copyright © 1998 Movement Disorders Society)

1.1.1.1 Mechanical oscillations

Any movement is physically produced by the joints and the muscles. A joint is a mechanical structure which obeys the rules of physics [2]. Muscles have been modeled as three-element mechanical structures, each comprising of a neural input processor, springs and internal damping. A mechanical system oscillates at its resonant frequency under the action of any disturbance. In the human body, one such disturbance occurs due to blood ejection during cardiac systole [2]. The pulsatile perturbations cause the joints to oscillate at a frequency governed by the following equations [1] [2]:

$$\begin{aligned} f_0 &= \frac{1}{2\pi}\sqrt{\frac{K}{J}} \\ \omega &= \sqrt{\frac{K}{I}} \end{aligned} \tag{1.1}$$

where K is the stiffness of the joint, I is the inertia of the joint and J is the moment of inertia of the joint. It is evident from the above equations that the mechanical component of tremor is highly dependent on the mechanical properties of the bones, muscles and soft tissues. It can be inferred from the above equations that the frequency of mechanical component will change under an external load on the body part [1] [2].

1.1.1.2 Reflex oscillations

Reflex loops are divided into 2 types: peripheral loops and central loops. Peripheral loops run from muscle fiber to the spinal cord and back. Central loops run from the periphery of the spinal cord to the supraspinal levels including the brainstem, the cerebellum, the basal ganglia and the cerebral cortex [2]. These loops run over time with certain time delays. Reflex oscillations occur in reflex loops if the loops are under-damped and the frequency of such oscillations is the inverse of the double time delay [1] [2]. When the frequencies of mechanical oscillations and reflex oscillations are equal, they are augmented to a single frequency known as the mechanical reflex [2]. Reflex oscillations are independent of the mechanical properties of the body. However, if the body part is under any external load, it increases the loop delay which reduces the frequency of the reflex oscillations [1].

1.1.1.3 Central oscillations

Central oscillations are produced due the neural activity pertaining to the properties of individual neuron, neuronal networks or a combination of both. It follows a rhythmic behavior [2]. Central oscillations are independent of the mechanical properties of the body and are not affected by external loading of the body part [1].

1.1.2 Tremor Classification

The cause of tremor is either physiological or pathological. Physiological tremor is intrinsic to all humans [3]. Pathological tremor is either idiopathic or occurs secondary to a disorder such as a brain tumor, alcohol or drug withdrawal or multiple sclerosis [4]. Unlike physiological tremor, it is a nonlinear and non-stationary movement [5] [6]. In most cases, a study of the amplitude is sufficient to differentiate between physiological and pathological tremors [7]. Tremor has been classified in different ways. In [3], it was classified as rest or action tremor. Action tremor was further divided into postural, isometric and kinetic tremor. The clinical point of view uses the classification of: rest, postural and kinetic tremors [5]. These three types of tremor are collectively known as action tremors.

Table 1.1: Classification of tremor and associated diseases [5]

Type	Tremor Frequency (Hz)	Diseases associated
Rest	3 - 6	Parkinson's disease Drug-induced Parkinsonism Stroke Posttraumatic tremor
Postural	4 - 12	Essential tremor Physiological tremor Cerebellar diseases Multiple sclerosis Posttraumatic tremor Metabolic diseases
Kinetic	<5	Cerebellar Lesion Essential tremor Multiple sclerosis

Rest tremor occurs when a body part is maintained at rest (e.g., resting the hand on a table). It usually disappears during voluntary movements of the limbs [5] [6] [8]. However, in [9], the authors reported that it may also be present with lower amplitude during posture and movement. It usually originates at the distal end and extends to the proximal end of the body parts [8]. It has also been reported that it may increase with mental stress or contralateral motion [5]. Frequency of rest tremor ranges from 3 to 6 Hz. The most common disease associated with rest tremor is Parkinson's disease (PD).

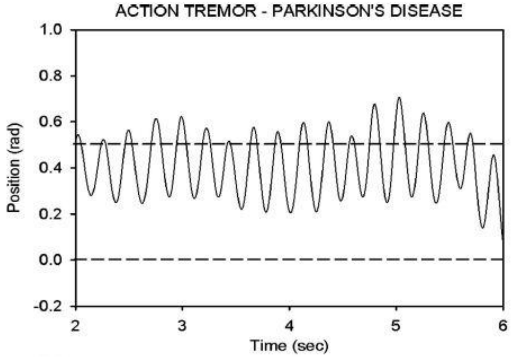

Figure 1.2: Parkinsonian Tremor in a patient [5] (Copyright © 2008 Morgan and Claypool)

Postural tremor occurs while maintaining a position against gravity (e.g., holding a cup). The frequency of postural tremor varies between 4 and 12 Hz. Kinetic tremor occurs during any kind of limb movement. Undesired motion due to kinetic tremor is perpendicular to the direction of the desired motion. Essential tremor (ET) is the most typical cause of postural and kinetic tremor. Cerebellar lesions also account for these two tremors. Physiological tremor has also been considered to be a peculiar form of postural tremor [5] [6]. Figure 1.3 shows drawings of Archimedes' spiral by 2 patients suffering from essential tremor.

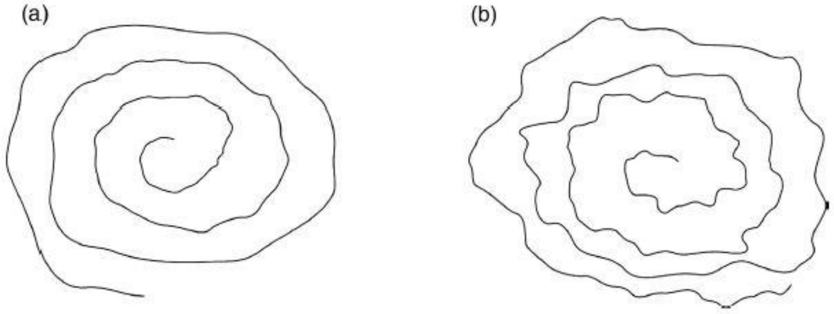

Figure 1.3: Essential tremor in 2 patients (a) with mild ET (b) with severe ET [5] (Copyright © 2008 Morgan and Claypool)

In addition to the above mentioned types of tremor, there are various other forms of tremor. These include isometric tremor, psychogenic tremor, task-specific tremor, dystonic tremor, Holmes' tremor, cortical tremor, orthostatic tremor, palatal tremor and tremor after a peripheral nerve injury [5]. Isometric tremor occurs during contraction against stationary objects. Psychogenic tremor may be continuous or intermittent with varying frequency and amplitude and is a combination of rest, postural and kinetic tremor. Task-specific tremor occurs during given actions (e.g., writing). Dystonic tremor is an extreme case of postural or kinetic tremor or occurs in a body part suffering from dystonia. Holmes' tremor (or midbrain tremor) predominantly affects proximal segments and has a frequency of less than 4.5 Hz. It occurs at rest and increases during movement and goal-directed tasks. Cortical tremor is a characteristic of a rare disorder, familial cortical myoclonic tremor. Orthostatic tremor occurs at higher frequencies ranging between 13 and 18 Hz and mainly affects the legs and the trunk. Palatal tremor occurs at the soft palate with a frequency range from 0.3 to 100 Hz (usually 1.5 to 3 Hz). It may affect the eyes, face, larynx, neck, shoulder and diaphragm. Tremor after a peripheral nerve injury occurs due to a lesion in the peripheral nervous system.

1.1.3 Treatments of tremor

Pathological tremor such as essential tremor, Parkinson's disease and other types of movement disorders make simple everyday tasks such as eating or holding a cup significantly difficult for individuals experiencing tremor with high amplitudes. This degrades the quality of life and causes social embarrassment. In extreme cases, individuals such as artists or surgeons are forced to quit their jobs [10]. Treatment for attenuating tremor can be categorized into three categories - pharmacological treatment, surgical treatment and external assistive devices. The treatment is chosen based on the severity of tremor and the side-effects associated with each treatment.

1.1.3.1 Pharmacological treatment

Medication is the first choice of treatment for those reporting movement disorders. Postural essential tremor can be reduced by primidone or propranolol [4] [5]. Ethanol is used as a clue for the diagnosis of essential tremor and not as a treatment due to adverse effects. Essential tremor in limbs is generally treated with β-blockers (propranolol). Drugs such as topiramate have been shown to improve functionalities affected by essential tremor such as writing or speaking [5]. Parkinson's disease is generally treated by dopamine agonists such as levodopa, pramipexole or ropinirole [4] [5]. Pharmacological treatment has varying success in abating tremor and side-effects of drugs can be severe. For instance, β-blockers may cause reduced blood pressure, confusion, dizziness or drowsiness [5]. The side-effects associated with dopamine agents are memory impairment, hallucinations, dry mouth, urinary difficulties and blurred vision [4].

1.1.3.2 Surgical treatment

The surgical approach is followed for individuals exhibiting a high degree of tremor or in cases where medication was found to be ineffective. The two most prominent surgical treatments for suppressing tremor are thalamic deep brain stimulation (DBS) and radiofrequency thalamotomy.

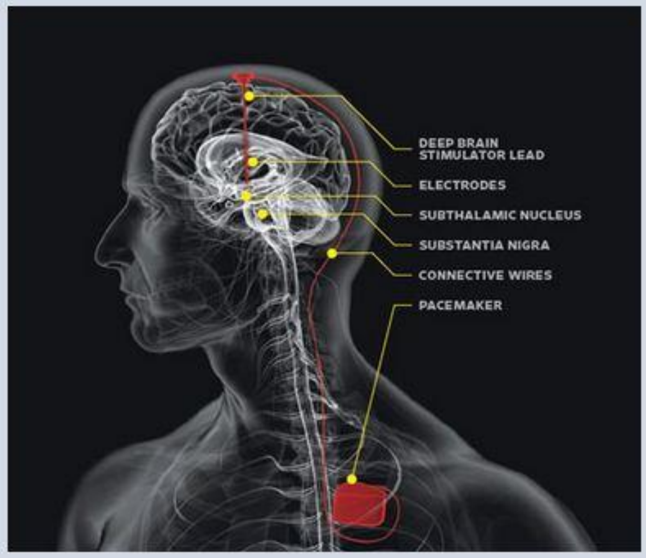

Figure 1.4: Representation of Deep Brain Stimulation (DBS) [11] (Copyright © Brown University)

DBS, shown in Figure 1.4, is a reversible procedure which involves implantation of a brain pacemaker which stimulates specific parts of the brain [5] [11]. Radiofrequency thalamotomy is an invasive procedure involving ablating certain portions of thalamus. While DBS is usually a safe procedure, however, side-effects such as permanent neurologic deficit, infections, depression, cognitive impairment, mania or behavior changes are still associated. It has also been reported in some studies that patients treated with DBS have higher suicidal rates. Patients treated with thalamotomy may develop side-effects such as aphasia, partial visual field deficit or speech disturbance [5]. The most serious risk with both the procedures is intracranial hemorrhage which may cause stroke leading to permanent weakness or death.

Gamma knife (γK) radiosurgery is an alternative approach in treating Parkinson's disease or essential tremor in patients who are not fit for radiofrequency thalamotomy or DBS. Unlike radiofrequency thalamotomy or DBS, it is a minimally invasive procedure.

However, side-effects such as delayed neurological deficit or patients developing complex disabling movement after γK thalamotomy are still present [5].

1.1.3.3 Assistive Devices

Patients with severe uncontrollable tremor who cannot be treated with medication or surgery due to high risks are treated using external assistive devices, prosthetic devices, or devices employing human-computer interaction.

The MIT damped joystick [12] and Neater eater [13] are the examples of external devices which suppress tremor to assist users in controlling an electronic wheel chair and in eating respectively. These devices implement a grounded force-feedback system and reduces tremor by viscous dampers.

Figure 1.5: Neater Eater [13] (Copyright © Neater Solutions)

Unlike stationary and passive systems such as MIT damped joystick and Neater Eater, the DRIFT project (WOTAS) is a prosthetic device for suppressing tremor in upper limb by actively controlling the forces [14] [15] [16] as shown in Figure 1.6. One of the main drawbacks of passive systems is that the dissipative force also restricts patient's voluntary motion. User comfort is also an issue as significant forces are applied to the user [16]. Wearable prosthetic and external devices require improvements in terms of appearance, size, shape, cosmetics and functional aspects [5].

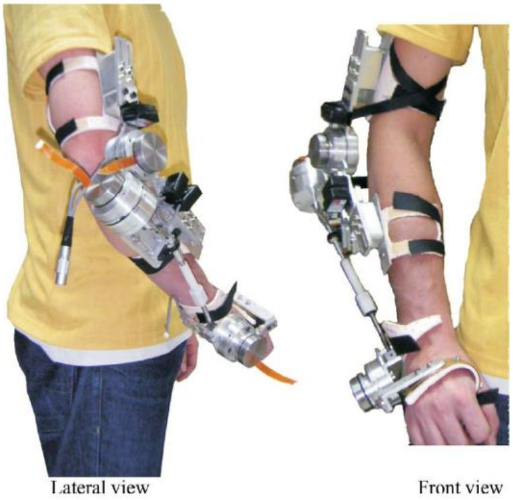

Figure 1.6: WOTAS device for the upper limb [14] (Copyright © 2007, IEEE)

In systems employing human-computer interaction, motion from the affected area is recorded and filtered using a digital filtering algorithm in real time to compute the tremor in the signal. A computer mouse, developed by IBM R&D [17], uses an adapter between the mouse and the computer which estimates the tremor acting on the mouse and provides smooth motion of the mouse on the screen. Micron, shown in Figure 1.7, is an active hand-held microsurgical device developed at Carnegie Mellon University which uses an adaptive filtering algorithm to compensate for hand tremor during microsurgery [18].

Figure 1.7: Micron, an active hand-held device for tremor cancellation [18] (Copyright © The Robotics Institute, Carnegie Mellon University)

1.2 Physiological Tremor

Unlike pathological tremor, physiological tremor is inherent in all humans. It is an involuntary, approximately rhythmic and roughly sinusoidal movement. It is composed of two distinct oscillations namely mechanical reflex and a central neurogenic component superimposed upon a background of irregular fluctuations in muscle force and limb displacements [19] [20]. The mechanical reflex component is the larger of the two oscillations. It is produced by irregularities in the motor-unit firing and by the force of the blood entering the body part during cardiac systole [21] [22].

Since physiological tremor has a mechanical reflex component which is dependent on the elasticity and inertia of joints, the characteristics of physiological tremor is highly dependent on the body parts [19]. For instance, the frequency of tremor in the elbow ranges from 3 to 5 Hz. On the other hand, tremor in the metacarpophalangeal joint has a frequency as high as 17 to 30 Hz. Table 1.2 shows the frequency of tremor associated with different body parts. As the frequency depends on the inertia of the joint, it is evident that the frequency of physiological tremor decreases when an inertial load is added to the limb.

Table 1.2: Tremor in different body parts [21] [23] [24] [25] [26] [27]

Bodily Region	Tremor Frequency (Hz)
Wrist	8-12
Elbow	3-5
Body (Standing position)	1.5
Ocular (Eye)	35-40

The amplitude of the physiological tremor increases while maintaining a position, for instance while standing. It is also age dependent: elderly persons tend to have more physiological tremor [5]. Mental stress increases the amplitude of physiological tremor; however, it reduces the frequency of the oscillations [28]. It is amplified by anxiety, fatigue and mental stress. Various metabolic conditions such as thyrotoxicosis or hypoglycaemia and drugs such as amiodarone, cinnarizine, antithistamine, nicotine or donezepil enhance physiological tremor. Under these situations, it is called enhanced or exaggerated physiological tremor [5].

1.2.1 Areas affected by Physiological Tremor

Physiological tremor is benign for everyday tasks such as walking, drinking or eating. However, any task requiring fine muscle control is susceptible to physiological tremor. Particularly, areas such as military targeting, optical instruments (e.g., cameras) and microsurgery are affected by physiological tremor and the performance is significantly degraded due to the involuntary motions.

1.2.1.1 Military Targeting

Physiological tremor creates a problem during tasks such as targeting or range-finding. During combat, soldiers experience high level of stress due to incoming fire, loud noises, fear of death and uncertainty. It has been reported that soldiers experience rapid breathing and increased heart beat (300 beats per minute). These factors amplify physiological tremor making it significantly more difficult for soldiers to aim at a target. This results in decreasing the chances of survival for the soldiers, mission success and civilian lives [29]. Conventionally, these problems are addressed by extensive training given to the soldiers which includes physical conditioning to build physical strength and stamina, mental conditioning to control psychological effects and marksmanship training which trains soldiers to control breathing, assume and maintain a steady position and properly squeeze the trigger. During actual combat, even the best trained soldiers exhibit some level of physiological tremor leading to performance degradation. Various techniques have been implemented to compensate for tremor. One such technology is the Inertial-Reticle System (IRS) [30], shown in Figure 1.8, developed at the Army Research Laboratory (Aberdeen Proving Ground MD). It uses a video screen to locate the target. The system tracks the motion of the rifle using inertial sensors and automatically fires when the target is aligned with the barrel of the rifle. The system is expensive and extremely bulky, thus lacking portability.

The INertially Stabilized Rifle (INSTAR) [29] developed by Intelligent Automation employs piezoceramic materials and cancels tremor in 1 degree of freedom. INSTAR lacks practical application because it is not robust due to the use of piezoceramic materials.

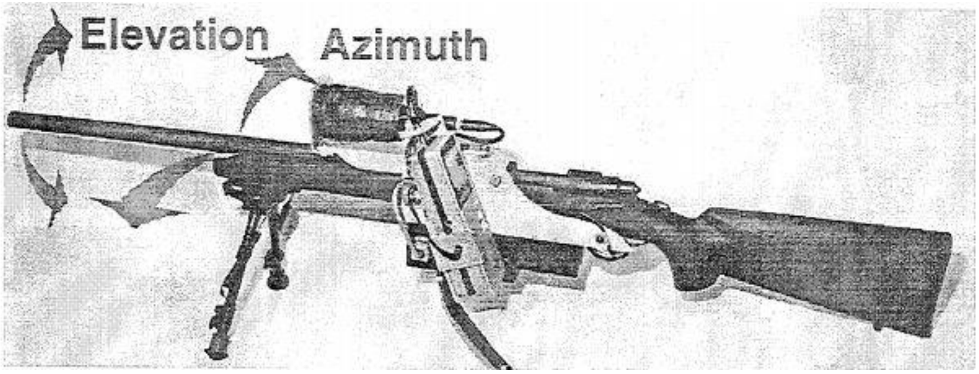

**Figure 1.8: Inertial Reticle System (IRS) on Remington 700 Sniper Rifle [30]
(Copyright © 1996 Army Research Lab, USA)**

1.2.1.2 Optical Instruments

The quality of images from instruments such as still cameras, video cameras or binoculars are vulnerable to physiological tremor. Camera shake due to tremor can cause blurring of images. In the case of photography, effectively exposing a film (or digital sensor in case of a digital camera) to take a photograph depends on the shutter speed, aperture (which is a function of a focal length) and film (or digital sensor) sensitivity (ISO). Blurred images are common in images taken with slower shutter speeds or with telephoto lenses. In videos, blurring might appear in individual frames or the tremor might have a cumulative effect over time causing frame-to-frame jitter.

Canon patented an image stabilization technology in 1976 entitled "Image stabilizing optical system having a variable prism" [31]. Canon also commercially introduced image stabilization enabled lenses in 1995. Currently, various digital single lens reflex cameras (DSLRs), video cameras, binoculars and point-and-shoot cameras use image stabilization technology to reduce image blur.

Most of the cameras use MEMS-based gyroscopes to measure motion in two axis, pitch and yaw. There are two types of technologies to cancel hand tremor: lens-based or body-based. Nikon and Canon use lens based technology. In the lens-based cancellation, lens is moved orthogonally to the optical axis of the lens using an electromagnetic linear motor or voice coil as shown in Figure 1.9. In body-based stabilization, the sensor is moved to compensate for the motion of the camera as shown in Figure 1.10.

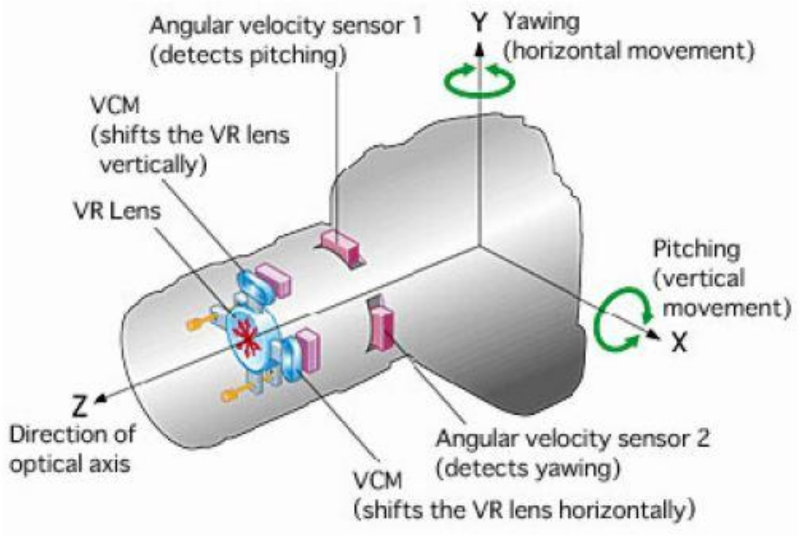

Figure 1.9: Lens-based Image Stabilization using voice coils in a Nikon lens [32] (Copyright © Nikon)

Figure 1.10: Body-based Image Stabilization in Konica Minolta camera [33]

In video cameras, digital image stabilization is used which shifts the image by a certain number of pixels in real-time using an adaptive motion computation scheme instead of shifting the lens or the image sensor [34].

The image stabilization technology in the cameras reduces tremor in the range of ±1°. It assists in taking hand-held photographs at much slower shutter speeds [35].

Figure 1.11: (Left) Image blur without image stabilization; (Right) Sharp image with image stabilization by Canon

1.2.1.3 Medical

Surgical procedures which require precise positioning or micromanipulation of tool-tip are always vulnerable to physiological tremor. The imprecision in positioning the tool-tip makes microsurgical procedures such as ophthalmological, orthopedic, microvascular, neurological and inner ear surgery difficult and makes some procedures impossible. One such procedure is vitreoretinal surgery which involves removing tissues as thin as 20 µm from the retina. Another example is intraocular cannulation which includes inserting a micropipette into 100 µm retinal vein and delivering anticoagulants to treat occlusions. Both of these procedures are difficult to perform without tremor cancellation [36] [37].

The accuracy of microsurgical procedures depends on the experience of the surgeons and the dexterity of the surgeon's hands. Conventionally, surgeons use an operating microscope to visualize surgical instruments along with resting their arm and wrist [38]. It has also been reported that surgeons control their sleep and caffeine intake and/or take beta-blockers prior to surgery to reduce tremor amplitude [39] [40].

In [41], the authors reported that the root-mean-square (rms) amplitude of a tool-tip during vitreoretinal surgery was 24 µm, 22 µm and 20 µm along the x, y and z axis respectively as shown in Figure 1.12.

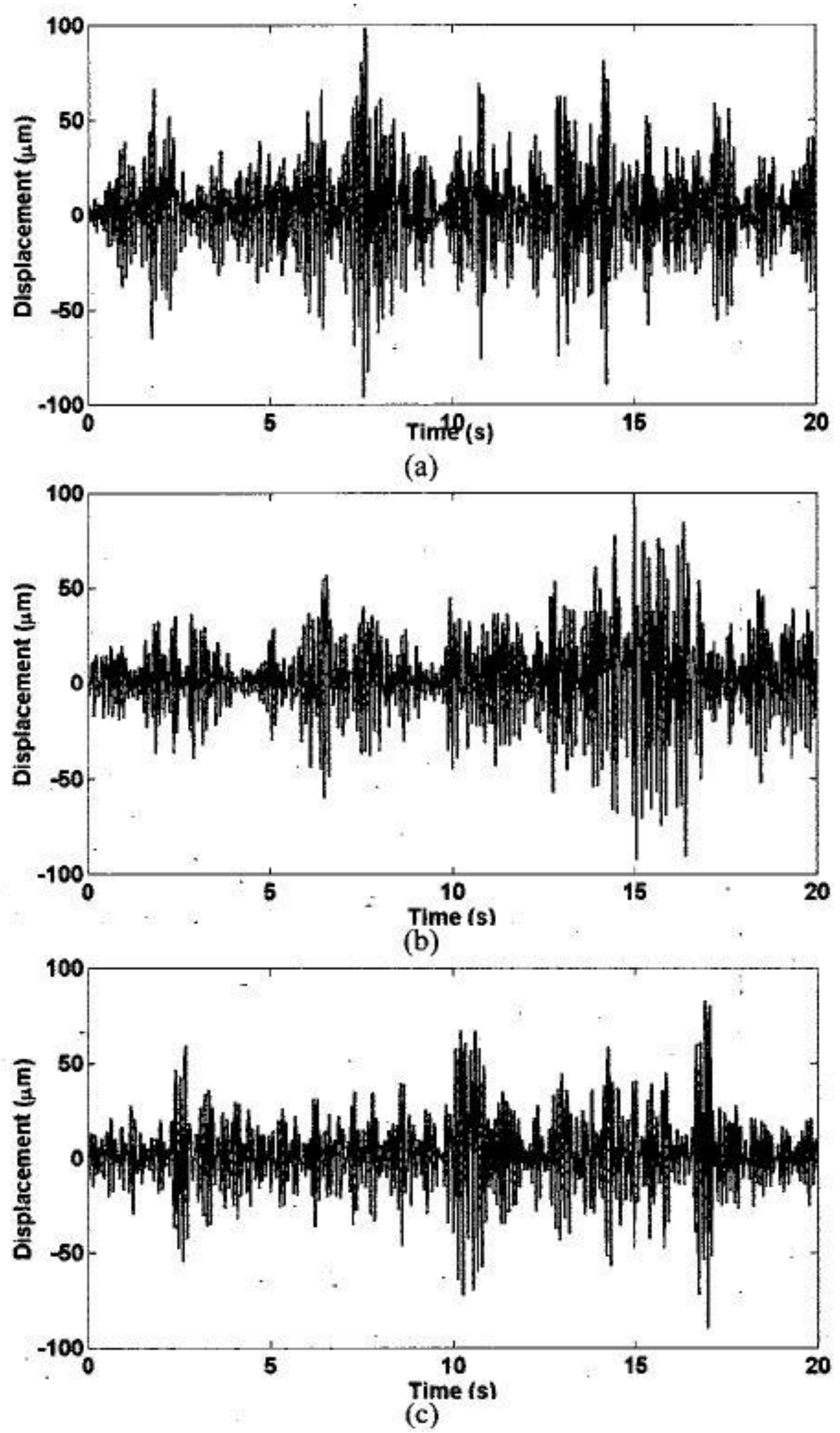

(a)

(b)

(c)

Figure 1.12: Amplitude of a physiological tremor during vitreoretinal microsurgery. (a) X axis. (b) Y axis. (c) Z axis [41] (Copyright © 2002, IEEE)

1.3 Tremor Cancellation Technologies in Ophthalmology

Various technologies exist for micromanipulation of microsurgical devices which assists surgeons to accurately position the tool-tip during ophthalmological microsurgery. The most prominent technologies are Robot Assisted Microsurgery (RAMS), Steady-hand Robotic System (SHR) and Micron.

1.3.1 Robot Assisted Microsurgery (RAMS)

RAMS was developed by researchers at Jet Propulsion Lab in 1994 [42] [43] [44] [45] [46]. It is a dual-arm 6 degrees of freedom (DOF) master-slave telerobotic system as shown in Figure 1.13.

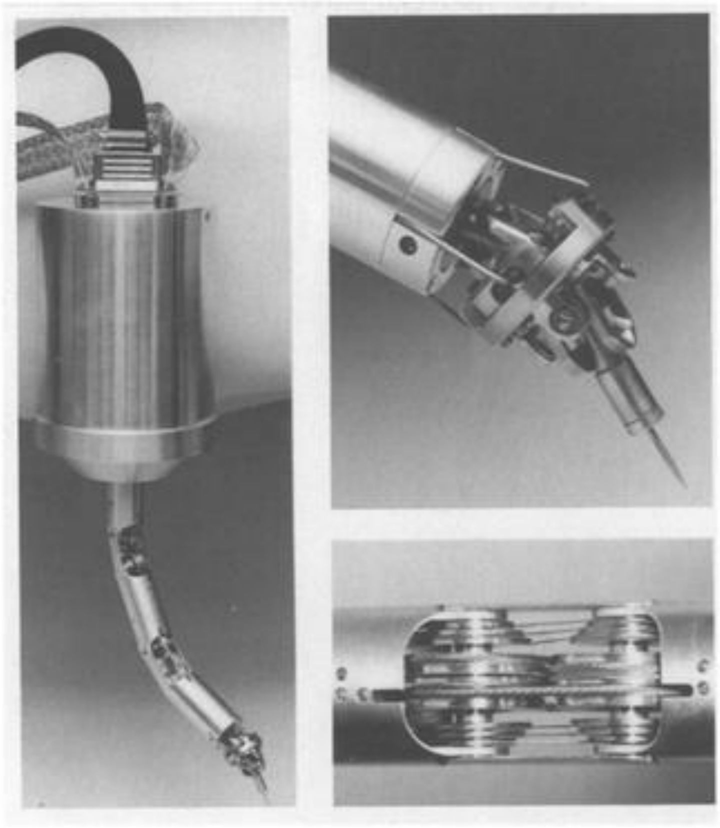

Figure 1.13: Robot Assisted Microsurgery (RAMS) [44] (Copyright © 2006 Springer Berlin/Heidelberg)

The actuation mechanism is a revolute-joint and cable-driven double-jointed mechanism having all the joints decoupled. Five of the 6 DOF have zero backlashes and the sixth has about 20 µm. The torso can achieve 165 degrees of motion while both the shoulder and elbow have a full 360 degrees of motion. The wrist has 180 degrees of pitch and yaw with 540 degrees of roll. It is 25 cm long in full extension and 2.5 cm in diameter. The base of the robot is 17.75 cm long and 12 cm in diameter. The entire robot weighs 5.5 lbs. The motor/encoder unit can be removed from the base which allows for sterilization of robot.

A graphical user interface (GUI) is offered on a UNIX workstation which also hosts a VxWorks real-time control environment. A Delta Tau Data Systems PMAC board on VME chassis directly reads the robot sensor outputs and drives the motors to control the six axes of the robot. A MC 68040 board, installed in VME chassis, implements the VxWorks-based kinematic & joint controls. The GUI is based on X Windows and OSF/Motif Libraries. It offers various control modes which a user can select.

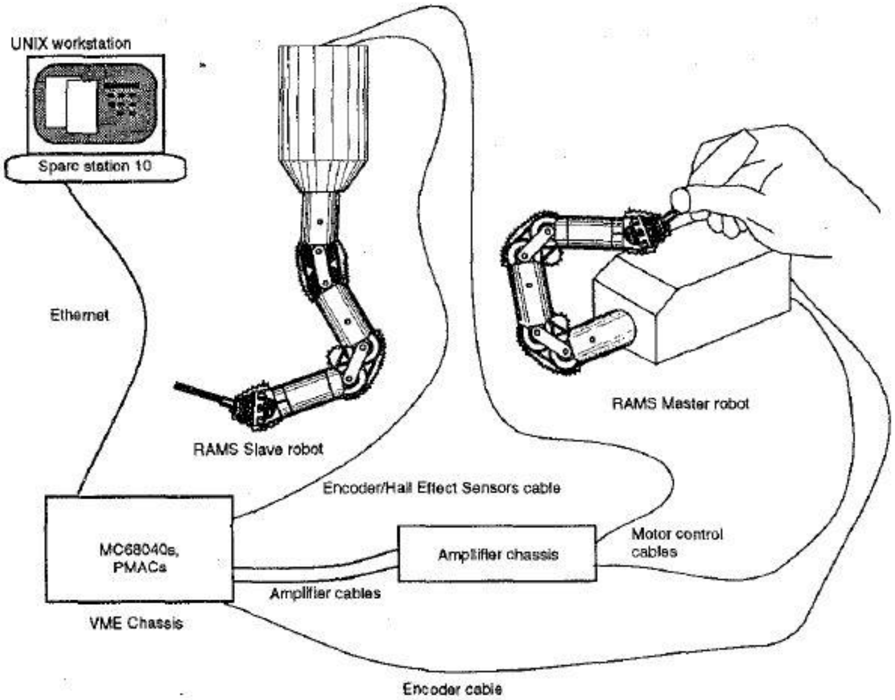

Figure 1.14: RAMS System [46] (Copyright © 1997, IEEE)

In preliminary experiments, the tip of the slave robot was reported to achieve a repeatable relative positioning of 25 µm [42] [43] [44]. In a simulated eye microsurgery procedure, RAMS was found to successfully remove 0.015 inch diameter particles from a simulated eyeball [46]. A pilot study was conducted to compare the performance of RAMS against manual instrument positioning [47]. The study consisted of three groups of subjects: 7 second year medical students, 7 ophthalmology surgeons and 9 robotics engineers. It was found that RAMS increased the time of positioning the tool. Medical students and engineers were found to perform better with the use of RAMS. However, surgeons did not have a significant advantage using the system. In [48] and [49], the authors reported that the RAMS workstation occupies 35% of the operating table as compared to 10 to 15% in human-assisted procedures and takes longer set-up time. The surgeons also need training to operate the system [49]. In a feasibility study reported in [50], the authors tested the use of RAMS in microvascular anastomosis in neurosurgery by performing carotid arteriotomies in 10 rats by RAMS as well as conventional microsurgical techniques. The precision, technical quality and error rate of telerobotic surgery were found similar to the conventional microsurgery. It was also reported in [50] that the procedures conducted with RAMS were longer in duration than with conventional procedures.

1.3.2 Steady Hand Robotic System

A Steady Hand Robotic System (SHR) was developed by researchers at Johns Hopkins University [51] [52]. In this system, the tool is held simultaneously by the operator's hand and the robot arm. The robot provides a tremor-free positional control of the tool by augmenting the force exerted by the user on the tool and by the tool on the environment.

Figure 1.15 shows the first prototype of the Steady Hand Robot [51]. It is a 7 DOF manipulator consisting of an XYZ translation base for coarse positioning, a shoulder having two rotational DOF, instrument insertion and rotational stages. A positional accuracy of 10 µm was achieved with the prototype as reported in [51]. In [53], various experiments were described to test the performance of the Steady-hand Robot in positioning and following straight lines and curves. Lines and curves were followed autonomously, unassisted (direct user control) and in augmented mode (user and robot) by detecting lines and curves through an endoscopic camera mounted on the robot.

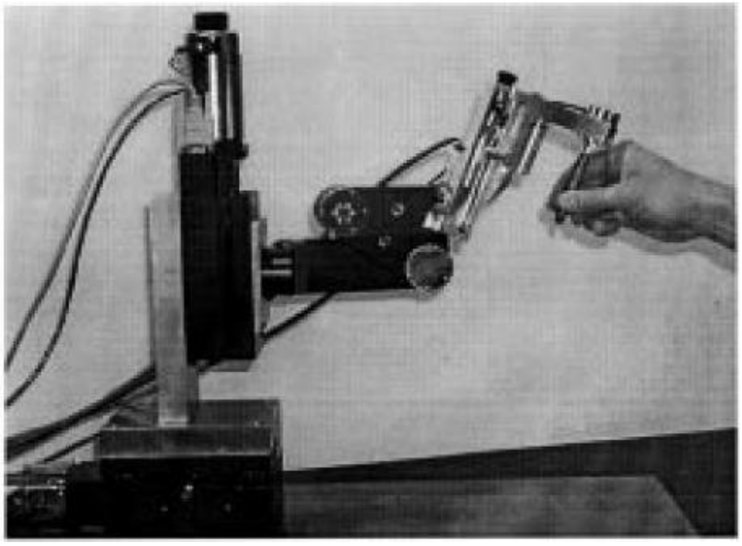

Figure 1.15: First prototype of the Steady Hand Robot [51] (Copyright © 1999, SAGE Publications)

The authors in [53] reported that the accuracy in following the lines and curves in augmented and autonomous mode was improved with the use of the Steady-hand Robot. In [54], the authors tested the ability of humans to position a 10-0 microsurgical needle to 250, 200 and 150 µm accuracy using the Steady-hand Robot. Similar to the experiments in [53], the accuracy was compared in three modes: unassisted, augmented and autonomous. It was reported that the success rate improved from 43% in unassisted mode to 79% in augmented mode and 96.5% in autonomous mode for 150 µm holes. In [52], it was reported that the first prototype was not a useful clinical system due to various limitations, particularly having a bulky mechanism near the patient which rendered the system ergonomically inconvenient for surgeons.

An improved prototype of the Steady Hand Robot (SHR) was reported in [52]. It consists of 4 parts: XYZ mechanism, roll mechanism, tilt mechanism and tool holder. The XYZ translation assembly is formed by using off-the-shelf motorized micrometer stages from New England Affiliated Technologies (NEAT), Lawrence, MA. A single axis Z stage (NEAT: LM-400) is mounted orthogonal to a dual axis X-Y table (NEAT: XYR-6060) to form an XYZ mechanism. The positional resolution is less than 2.5 µm with a stroke of 100 mm along each axis. The roll mechanism is achieved by incorporating a rotary table, B5990TS from Velmex Inc. The range of motion is ±180 degrees with repeatability of 1 arc-second. Figure 1.16 and 1.17 shows the prototype of the SHR as reported in [52].

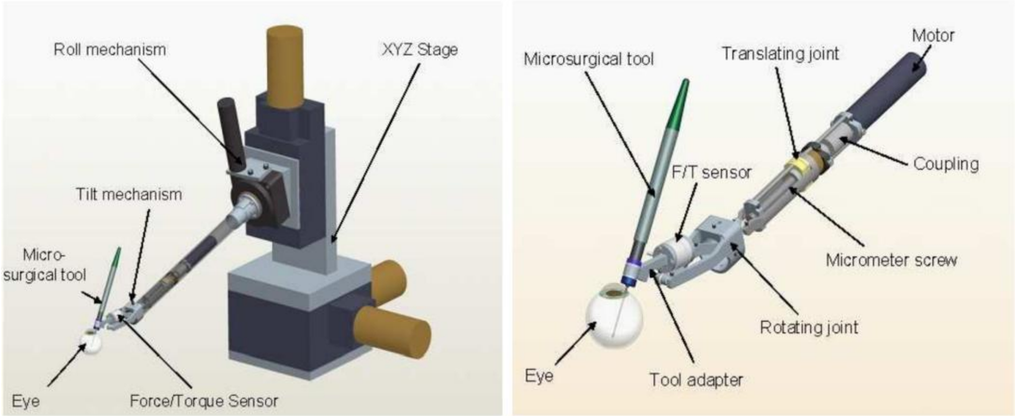

Figure 1.16: Prototype of the SHR as reported in [52] (Copyright © 2007, IEEE)

The tilt mechanism is a slider crank mechanism and is attached to the roll mechanism using a carbon fiber tube. It consists of a high precision lead screw from Newport Corporation, a DC Maxon motor (RE 16), planetary gearhead (GP 16 A) and Digital MR Encoder. The range of motion of the tilt mechanism is ±30 degrees relative to the vertical tool position. The tilt mechanism also hosts a force sensor, NANO-17 from ATI Industrial Automation. The tool holder can hold various tools required during microsurgery such as forceps, needle and scissors.

Figure 1.17: Tilt mechanism of the second prototype of SHR [52] (Copyright © 2007, IEEE)

In [52], the authors tested the SHR for vein cannulation on chicken embryos and reported that an experienced user of the robot cannulate ~80 µm vein in under a minute using the SHR. During freehand (i.e., simply holding the tool without the help of the robot) cannulation by an experienced user, significant damage to the vein and the surrounding tissue was reported. The system also enabled maintaining the cannulation for an indefinite time as compared to the finite length of time for freehand cannulation.

1.3.3 Micron

The Micron [18], developed at Carnegie Mellon University, is an active hand-held device. The instrument senses its own motion, filters between voluntary and involuntary motions, and deflects its tip to compensate for the involuntary part of the motion.

Figure 1.18 shows the first prototype of the Micron [55] [56] [57] [58]. It is 210 mm long with an average diameter of 22 mm and weighs 170 g. Three gyroscopes (Tokin Corp., CD-16D) and three tri-axial accelerometers (Crossbow Technology Inc., CSXL02LF3) have been used for motion sensing in six DOF. A nonlinear adaptive noise canceling algorithm, Weighted-frequency Fourier Linear Combiner (WFLC) [59], and a cascaded neural networks algorithm with extended Kalman filtering have been employed to calculate the erroneous motion by filtering the signals from the sensors. Three piezoelectric stacks, each with seven piezoelectric elements (TS 18-H5-202, Piezo Systems Inc.) forms the actuator module.

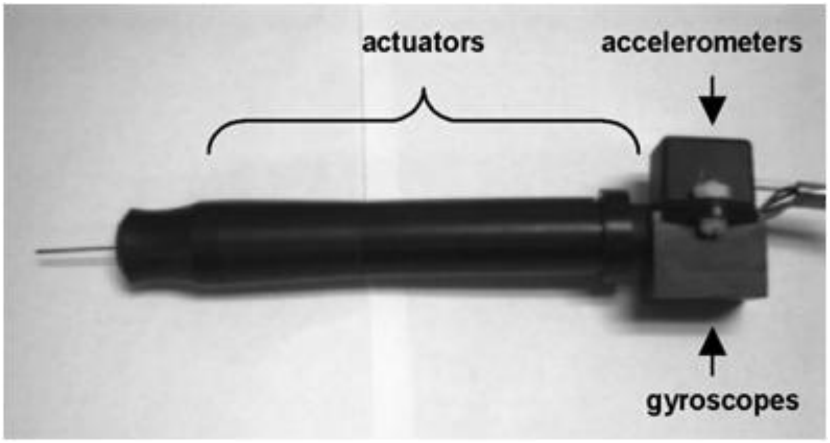

Figure 1.18: First prototype of the Micron [58] (Copyright © 2003, IEEE)

In [55] [56] [57] [58], the maximum tip displacement and velocity was reported to be 560 µm and 11.2 µm/µs in x & y axes and 100 µm and 2 µm/µs in z axis respectively. In [56] and [57], the authors tested the performance of the Micron in canceling tremor in 1-D (axial) and 3-D. The device was attached to a testbed oscillator which simulated tremor in the hand and an optical tracking system, ASAP [60], was used to measure the motion of the instrument tip. In 1-D cancellation tests described in [56] and [57], it was reported that the Micron reduced the average erroneous motion from 50.6 µm p-p at 9Hz to 27.7 µm p-p, representing a reduction of 45.3% and from 51 to 25 µm p-p, a reduction of 51% in similar 1-D tests conducted in [58]. In 3-D tests, a reduction of 37.2% in 10 trials was reported in [56], 34.3% in 10 trials in [57] and 34% in 12 trials in [58].

Figure 1.19: Prototype of the Micron as reported in [61] (Copyright © 2004, IEEE)

Further improvements in the work of [58] were reported in [61]. In this work, the authors modified the design and reduced the number of piezoelectric elements from 21 to 3. Figure 1.19 shows the prototype reported in [61]. This prototype weighs less than 100g. It is 180 mm long and has an average diameter of 20 mm with a diameter of 16 mm at the grasping section. The sensing unit consists of three dual-axis accelerometers (Analog Devices ADXL 203) and a three-axis magnetometer (Honeywell HMC-2003). Augmented state Kalman filtering algorithm has been used for tracking the orientation of the device and the tremor is estimated using WFLC. In [61], the prototype was tested in tracking 3-D motion. The authors reported a reduction of 51.9% over 10 trials in tracking 3-D motion of rms amplitude 24.7 µm at 9 Hz using the Micron. In [62], the authors reported a flexure based manipulator module to increase the stroke of piezoelectric actuators in the Micron. The maximum stroke of the flexure-based manipulator was reported to be 350 µm along the x-axis, 425 µm along the y-axis and 80 µm along the z-axis. The rms error in tracking a sinusoidal waveform along the x-axis was reported to be 6.5 µm and the rms error in 3D tracking was reported to be 12.1 µm in [62].

In [63] and [64], the authors presented a new prototype of the Micron. This prototype consists of a tip manipulator with four LEDs and a custom optical tracking system, ASAP [60]. The manipulator is composed of piezoelectric bender actuator (Thunder TH-10R, Face Technologies) with a range of motion of approximately 0.5 mm axially and 1.8 mm transversely. The optical tracking system consists of position-sensitive detectors (PSDs) to detect the four LEDs mounted on the handle and the manipulator to measure the position of the tool-tip in six DOF. Tremor is calculated based on the information from the optical tracking system and compensated for by the manipulator. The user manipulates the device by visualizing the tip under a stereo operating microscope or through a 3D computer display. Figure 1.20 shows the prototype reported in [64].

Figure 1.20: Prototype of the Micron as reported in [64] (Copyrights © 2009, IEEE)

In [65] and [66], the authors tested the performance of the prototype of the Micron as reported in [63] and [64] for retinal photocoagulation procedure. Two scenarios were compared: aided and unaided. In the aided scenario, the Micron actively targeted the location and fired the laser automatically based on the information from the stereo cameras (which tracked the finder beam and the target) and ASAP (which tracked the tip and pose of the Micron). In the unaided scenario, clinician targeted the location and fired the laser. It was reported that the accuracy of laser photocoagulation increased with the assistance of the Micron and the duration of the procedure was reduced. The success rate in cannulating veins of diameter 40-60 μm was reported to be higher with the use of the Micron as compared to unaided cannulation [67].

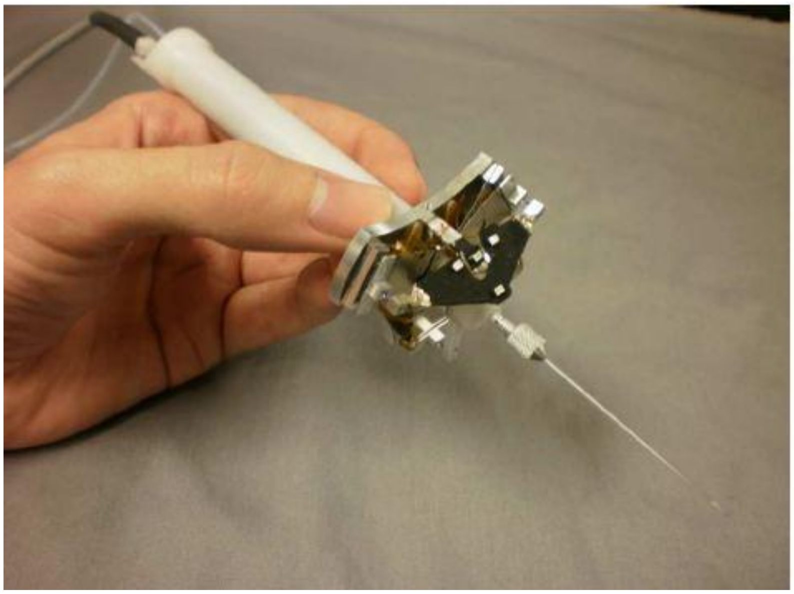

Figure 1.21: Prototype of the Micron as reported in [68] (Copyright © 2010, IEEE)

In [68], the Micron was tested for micromanipulation of cells. The authors reported that the accuracy of micromanipulating the cells increased when the Micron was used. However, the size of manipulator and the range of its motions were found to be the limitations in micromanipulation tasks.

1.4 Thesis Outline and Organization

In the research reported in this thesis, a novel handheld device, AID, has been developed for active compensation of physiological tremor in the hand that is light in weight, compact in size and cost effective. The primary issue of a handheld device for active tremor cancellation lies in its implementation. The device must be able to sense the hand motion, calculate the tremor and produce a sufficient amount of actuation at required frequencies to cancel the tremor component in the hand motion, yet remain light weight so as to reduce fatigue resulting from holding the instrument for prolonged periods during the procedure. It is necessary that it be compact and similar in design to the current standard microsurgical instruments to give surgeons a sense of familiarity.

One of the most important aspects of an active tremor cancellation system is zero phase shift. The hand motion is composed of desired motion and involuntary motion (tremor). The device should sense the motion, differentiate between the desired motion and the erroneous motion and estimate the tremor component followed by producing an equal but opposite motion at the tool-tip. MEMS based accelerometers and gyroscopes have been employed to sense hand motion in six DOF because they are compact in size and light in weight. However, the disadvantage of using rate grade gyroscope and MEMS based accelerometers is the notorious integration drift due to the noise present in the sensor signals. Therefore, an augmented state complementary Kalman filter has been developed to calculate real-time 2 DOF orientation of the device by fusing the gyroscope and the accelerometer signals. A zero-phase adaptive filter, Band-limited Multiple Fourier Linear Combiner (BMFLC) algorithm, has been implemented to calculate the tremor component in the hand motion. To avoid the integration drift in calculating the position of the needle tip, the acceleration has been analytically double integrated inside the BMFLC algorithm using the rhythmic nature of the tremor.

In Chapter 2, we present the selection procedure of the sensors followed by presenting an algorithm to sense physiological tremor in 3 DOF using tri-axial accelerometer and gyroscopes. This chapter also includes a brief literature review on orientation tracking using Kalman filtering technique followed by describing the proposed augmented state complementary Kalman filter. The last section of the Chapter 2 presents various adaptive filtering techniques followed by describing the band-limited multiple Fourier linear combiner algorithm (BMFLC) that has been employed to filter the tremor component.

Since the device must be light in weight and compact in size, conventional actuators such as electrical, hydraulic or pneumatic are difficult to use because they are heavy and their performance degrades for compact applications. Smart materials, particularly Ionic

Polymer Metallic Composites (IPMCs) provide a good solution because they can be easily manufactured, can actuate with high frequencies along with sufficient stroke to cancel tremor and are light in weight. Chapter 3 presents the selection process of the actuators followed by development of an open-loop controller to drive the IPMC actuator.

Chapter 4 presents the design of the hand-held device, AID, and a description of all the hardware and software components of AID followed by presenting an overview of the system.

Chapter 5 presents the experimental set-up to test AID and its subsystems. Various experiments have been conducted and results have been discussed to validate the effectiveness of the AID in compensating tremor.

Finally, Chapter 6 provides concluding remarks followed by a brief discussion of ideas for future work to improve the system.

Chapter 2

2 Design of Sensing System of AID

This chapter describes the design of the sensing system of the AID. Section 2.1 presents the system requirements of the sensing system and the selection procedure for the sensors. Section 2.2 provides a description of the inertial measurement unit (IMU) incorporated in the current implementation. The kinematics of the device to calculate the tremor at the needle tip are presented in Section 2.3. A zero-phase adaptive filtering technique, Band-limited Multiple Fourier Linear Combiner (BMFLC) has been used to estimate the tremor component in the sensed motion of the device. Section 2.5 presents various adaptive filters followed by a description of BMFLC. An augmented state complementary Kalman filter has been used to calculate 2 DOF orientation of the device and is presented in Section 2.4.

2.1 Sensing System Requirements

The most important aspect of the sensing system is that it should accurately detect small changes in motion incurred due to the physiological tremor. Therefore, it should have a high resolution and bandwidth higher than the frequency of the physiological tremor. The sensing module should also be light in weight and small in size so that it can be easily accommodated in a compact hand-held device. Moreover, the sensing system should not be affected by other electronic or surgical equipment. Since tremor in the hand is approximately sinusoidal with frequency ranging from 8-12 Hz, we assume it to be a perfect sinusoidal function with frequency 12 Hz and amplitude 70 µm peak-to-peak to define the system requirements. Based on this, the sensing system should meet the following the specifications:

- Resolution: ~7 µm (10% of 70 µm)
- Bandwidth: ≥13 Hz
- Sampling rate > 840 Hz

2.1.1 Sensor Selection

Motion tracking sensors can be categorized into two kinds: externally referenced and internally referenced. Externally referenced sensors include external active sources and receivers to track motion. Typically, they work using electromagnetic (EM), infrared (IR), radio frequency (RF), ultrasound (US), etc. The performance specifications, resolution, size and weight of some of the externally referenced sensors are shown in Table 2.1.

Table 2.1: List of externally referenced motion tracking systems

System	Aurora (NDI)	Polaris (NDI)	laserBIRD 2 (Ascension)	Fastrak (Polhemus)	Liberty (Polhemus)
Type	EM	IR	IR	EM	EM
Accuracy (deg)	0.2/0.3	-	0.5	0.15	0.15
Accuracy (µm)	700/480	350	700	710	710
Resolution (deg)	-	-	0.05	0.026	0.0004
Resolution (µm)	-	-	100	58.42	1.4
Sampling Rate (Hz)	40	60	240	120	240
Weight (gm)	0.7	< 10	40	9.1	9.1
Size (mm)	9 x Ø0.8	Ø6	100 x 90 x 40	22.8 x 28.2 x 15.2	22.8 x 28.2 x 15.2

Internally referenced sensors are self-contained and do not require interaction with external sources or receivers. Typically, these sensors use an inertial measurement unit (IMU), which is composed of accelerometers and gyroscopes that measure the motion in 6 DOF. With known initial conditions, IMU can calculate linear velocity, angular velocity, position and orientation of the body. The performance specifications, resolution, size and weight of some of the gyroscopes and accelerometers are shown in Table 2.2 and 2.3 respectively.

Table 2.2: List of gyroscopes

Model	GG 1320AN (Honeywell)	CG- L53 (Tokin)	IDG 500 (InvenSense)	MLX 90609 (Melexis)
Class	Navigation	Rate Grade	Rate Grade	Rate Grade
Type	Ring Laser	Piezoelectric	MEMS	MEMS
No. of axes	1	1	2	1
Range (deg/s)	±450	±90	±500/110	±75/150/300
Noise@15 Hz	0.813 deg/h	1.4 deg/s	0.4 deg/s	0.116 deg/s
Bias Stability	0.0035 deg/h	-	-	-
Sampling Rate	2 kHz (max)	> 1 kHz	> 1 kHz	>1 kHz
Size (mm)	45 x Ø88	6 x 10 x 2.5	4 x 5 x 1.2	10.6 x 10.6 x 2.9
Weight (gm)	454	1	< 1	1

Since the specifications of gyroscopes and accelerometers are defined in deg/s and g (gravity acceleration) respectively, we need to convert the required specifications of our sensing system to equivalent units of an IMU in order to compare the sensors. Since we have assumed tremor to have a sinusoidal profile having frequency (f) 12 Hz and amplitude (A) 70 µm p-p, we can write displacement due to tremor as:

$$d(t) = A\sin(2\pi f t) \tag{2.1}$$

Other inertial quantities such as velocity, acceleration and angular velocity can be derived using equation 2.1 and are shown in Table 2.4.

Table 2.3: List of accelerometers

Make	ADXL 335 (Analog Devices)	CXL02TG3 (Crossbow)	Model 4332-020 (Measurement Specialties)	8395A2 (Kistler)
Type	Capacitive MEMS	Capacitive MEMS	Capacitive MEMS	Capacitive MEMS
No. of axes	3	3	3	3
Range (g[1])	±3	±2	±2	±2
Noise (mg)	1.16 rms @ 15 Hz	0.3 rms @ 15 Hz	0.08	0.09 rms @ 15 Hz
Sampling Rate kHz	> 1	>1	> 1	> 1
Size (mm)	4 x 4 x 1.45	28 x 56 x 36	34.5 x 34.5 x 31.2	21.6 x 21.6 x 22.1
Weight (gm)	< 1	110	< 100	30

Using the maximum value specified in Table 2.4, the required specifications for the inertial measurement unit are:

---

[1] g is the gravity force sensed by the accelerometer

- Acceleration: 4.05 mg
- Angular Velocity: 0.3 deg/s

Table 2.4: Inertial quantities of motion due to tremor

Inertial Quantity	Function	Maximum Value
Velocity	$v(t) = A.2\pi f.\cos(2\pi ft)$	$v_{\max} = 5.28\,\mathrm{mm/s}$
Acceleration	$a(t) = -A.(2\pi f)^2 \sin(2\pi ft)$	$a_{\max} = 387.94\,\mathrm{mm/s}^2 = 40.56\ \mathrm{mg}$
Angular Velocity[2]	$\omega(t) = v(t) / D$	$\omega_{\max} = v_{\max} / D = 3.02\,\mathrm{deg/s}$

All the externally referenced sensors listed in Table 2.1 except Liberty (Polhemus) have resolution lower than the required resolution of 7 µm. Although Liberty Polhemus has the necessary resolution, the maximum sampling frequency of the system is 240 Hz which is less than the required sampling frequency needed for our sensing system. Hence, externally referenced sensors are not suitable for our application.

For accelerometers and gyroscopes, output noise floor limits the resolution of the sensors. The noise in the gyroscopes, Honeywell GG 1320AN and Tokin CG-L53 listed in Table 2.2, is much higher than 0.3 deg/s; therefore, they cannot be selected for our application. The noise in the MEMS-based rate grade gyroscopes, Invensense IDG 500 and Melexis MLX90609 listed in Table 2.2, is close to or lower than 0.3 deg/s. They are more applicable for a hand-held device because they are small and light in weight compared to a navigation grade gyroscope (Honeywell GG1320AN). The specifications of all the accelerometers listed in Table 2.3 match the required specifications of our sensing system. ADXL 335 has been chosen since it is light and small in size.

---

[2] D is the distance between the needle tip and the instrument center of mass. Although, it is unknown, it is assumed to be 100 mm in order to compare and select the gyroscopes.

2.2 Inertial Measurement Unit (IMU)

The IMU for the device is composed of a dual-axis gyroscope (IDG 500), a single axis gyroscope (MLX 90609) and a triple axis accelerometer (ADXL 335) as shown in Figure 2.1.

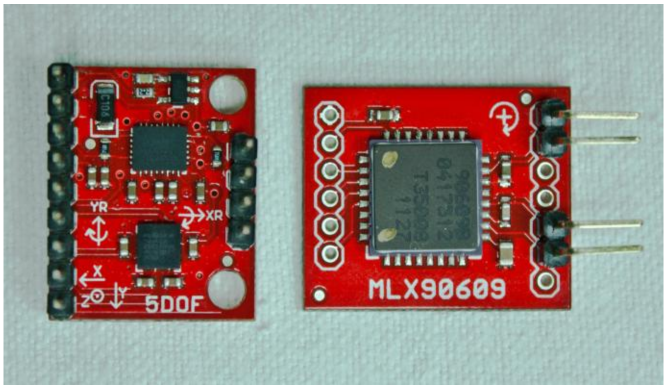

Figure 2.1: IMU boards. (L) Board containing IDG 500 and ADXL 335, (R) Board containing MLX 90609

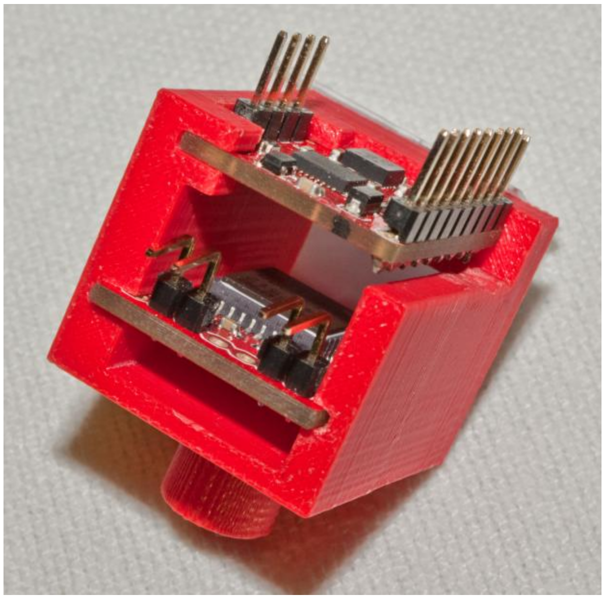

Figure 2.2: Sensor module containing IMU boards

The IMU boards also contain capacitors that limit the bandwidth of the sensors to 50 Hz. The IMU boards are attached to the sensor module as shown in Figure 2.2 and the sensor module is located at the distal end of the device as shown in the Figure 2.3.

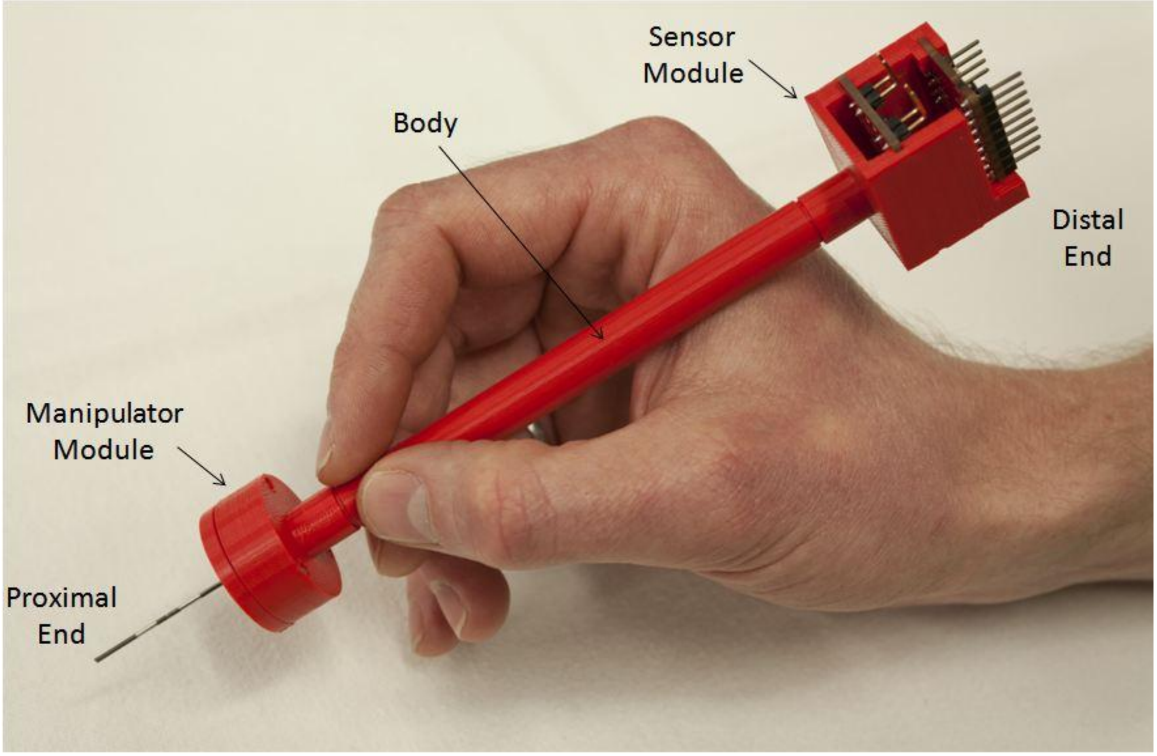

Figure 2.3: The sensor module in the AID is located at the distal end

2.3 Sensing Kinematics

This section presents the kinematics of the device to calculate the 3 DOF position of the needle tip due to tremor using the sensor measurements.

We attach a body frame $\{B\}$ at the location of tri-axial accelerometer as shown in Figure 2.4 such that the sensing axes of the accelerometer are coincident with the principal axes of the body frame, X_B, Y_B and Z_B. We also attach a gyro frame $\{G1\}$ and $\{G2\}$ at the location of the dual-axis gyroscope (IDG 500) and single gyroscope (MLX 90609) respectively such that the sensing axes of the IDG 500 and MLX 90609 are coincident with the principal axes of $\{G1\}$ and $\{G2\}$ respectively. Note that the axes Z_{G1}, X_{G2} and Y_{G2} are not shown in Figure 2.4 since IDG 500 only measures angular velocity about X_{G1} and Y_{G1} and MLX 90609 only measures angular velocity about Z_{G2}. Also, note that Z_{G2}, X_{G1} and Y_{G1} axes are opposite in direction to that of Z_B, X_B and Y_B respectively. We also attach a frame $\{S\}$ at the "non-tremulous" location of the needle tip. The orientation of $\{S\}$ is the same as that of $\{B\}$.

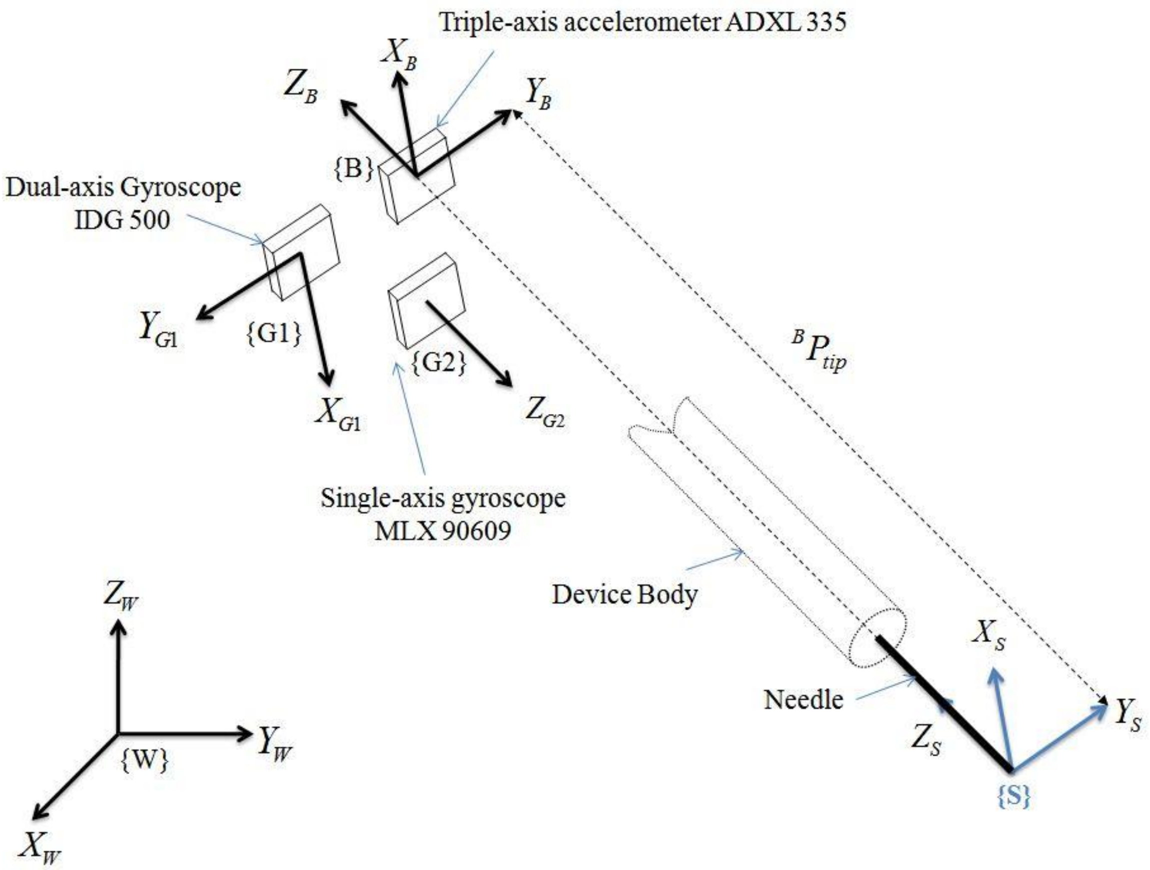

Figure 2.4: Kinematic representation of AID

The total acceleration (y_a) sensed by the triple-axis accelerometer, ADXL 335, is composed of inertial acceleration of the body (^BA) and gravity sensed by the accelerometer (^BG):

$$y_a = {}^BA + {}^BG \tag{2.2}$$

$$^BA = [\,^Ba_x \quad ^Ba_y \quad ^Ba_z]^T \tag{2.2a}$$

where ^Ba_x, ^Ba_y and ^Ba_z are inertial accelerations in the X_B, Y_B and Z_B axes respectively.

The angular velocity of the device with respect to $\{B\}$ can be written as:

$$ {}^{B}\omega = \begin{bmatrix} {}^{B}\omega_x & {}^{B}\omega_y & {}^{B}\omega_z \end{bmatrix}^T \tag{2.3}$$

where ${}^{B}\omega_x$, ${}^{B}\omega_y$ and ${}^{B}\omega_z$ are the angular velocities about the X_B, Y_B and Z_B axes respectively.

The dual axis gyroscope, IDG 500, measures the angular velocity about the X_{G1} and Y_{G1} axes:

$$ {}^{G1}\omega = \begin{bmatrix} {}^{G1}\omega_x & {}^{G1}\omega_y \end{bmatrix}^T \tag{2.4}$$

The single axis gyroscope, MLX 90609, measures the angular velocity about the Z_{G2} axis:

$$ {}^{G2}\omega = {}^{G2}\omega_z \tag{2.5}$$

Since the X_{G1}, Y_{G1} and Z_{G2} axes are in opposite direction to the directions of X_B, Y_B and Z_B axes respectively and the angular velocity is an intrinsic property of a rigid body, the angular velocity of the device with respect to $\{B\}$ is given by:

$$ {}^{B}\omega_x = -({}^{G1}\omega_x),\ {}^{B}\omega_y = -({}^{G1}\omega_y) \text{ and } {}^{B}\omega_z = -({}^{G2}\omega_z) \tag{2.6}$$

At t = 0, the principal axes of frame $\{B\}$ are assumed to be coincident with the principal axes of the world coordinate system $\{W\}$.

2.3.1 3 DOF Tremor at the Needle Tip

The aim of this section is to calculate the tremor at the tip of the needle that can be used as an input to the manipulator controller (described in Chapter 3). The accelerometer signals are composed of low frequency voluntary signals (< 1 Hz), gravity (<1 Hz), tremor (8 - 12 Hz) and noise (>15 Hz). Since there is a difference in the frequencies and only tremor component is of interest, other components need to be filtered out from the accelerometer measurements. One way is to pass the accelerometer signal through a normal band-pass filter such as a Butterworth filter with a pass-band of 7-13 Hz.

However, conventional filters change the phase of the input signal that obstructs the purpose of true real-time tremor compensation. Therefore, zero-phase adaptive band-pass filters such as the Band-limited Multiple Fourier Linear Combiner (BMFLC) [69] have been used to filter the tremor. Section 2.5 presents a detailed explanation of such filtering algorithms.

The conventional method to calculate tremor at the needle tip is to calculate the position of the needle tip with respect to the world coordinate frame {*W*} using kinematic relationships and then filter the tremor component using adaptive filters such as BMFLC. In this approach, first the orientation is calculated using gyroscopes. Using the orientation, the gravity component from the accelerometer signals is then removed to calculate the effective acceleration. The effective acceleration of the body frame {*B*} with respect to the world frame {*W*} can be written as:

$$ {}^{W}A = {}^{W}R_{B}\, y_{a} - {}^{W}G \tag{2.7}$$

where ${}^{W}G$ is the gravity vector with respect to the frame {*W*} and is given by $g[0 \quad 0 \quad 1]^{T}$. g is the gravity constant and is equal to 9.804 m/s^2. ${}^{W}R_{B}$ is the rotation matrix which describes the orientation of the body frame {*B*} with respect to the world frame {*W*}.

The velocity of {*B*} with respect to {*W*}, in the discrete-time format, can be calculated by integrating the effective acceleration of the body frame:

$$ {}^{W}V_{B,k} = {}^{W}V_{B,k-1} + {}^{W}A_{k}T \tag{2.8}$$

where *T* is the sampling time. Integrating equation (2.8), we get the position of {*B*} with respect to {*W*}:

$$ {}^{W}P_{B,k} = {}^{W}P_{B,k-1} + {}^{W}V_{B,k}\, T \tag{2.9}$$

The position of needle tip with respect to {*W*} can be written as:

$$ {}^{W}P_{tip,k} = {}^{W}P_{B,k} + {}^{W}R_{B}\,{}^{B}P_{tip} \tag{2.10} $$

where ${}^{B}P_{tip}$ is the position of the needle tip with respect to the body frame $\{B\}$. ${}^{W}P_{tip}$ is sent to BMFLC to estimate the position of the needle due to tremor.

One of the issues with this approach is that the errors in calculating the position of the needle tip grow quadratically after double integration (equations 2.8 - 2.10) due to the noise in accelerometer signals [70]. Since the motion of the tremor is rhythmic, the integration drift in calculating the position can be avoided by analytically double integrating the effective acceleration (${}^{W}A$) inside the BMFLC as proposed in [70].

It can be noticed from the above equations that 3 DOF orientation of the device should be known for calculating ${}^{W}A$. The 3 DOF orientation can be calculated by integrating the angular velocity measured using the gyroscopes. However, due to the noise in the gyroscope signals, the error in orientation grows linearly using this approach. Gyroscopes are seldom used alone in calculating orientation due to the integration drift. A complimentary sensor is used to calculate the orientation and the data is fused using a Kalman filter to compensate for the integration drift and correct the orientation calculated using the gyroscopes. The orientation can also be calculated using a tri-axial accelerometer. However, the estimation of orientation using a tri-axial accelerometer is noisy and vulnerable to vibrations and it only provides 2 DOF orientation. To calculate the orientation in 3 DOF, generally, a tri-axial magnetometer is used along with a tri-axial accelerometer and a tri-axial gyroscope. The measurements from these three sensors are, then, fused by the Kalman filter to provide a drift-free estimation of the orientation. The problem associated with this approach is that it makes the orientation estimation process computationally inefficient due to a larger size of the state vector of the Kalman filter and requires a tri-axial magnetometer.

In [71], the authors presented an algorithm to calculate tremor in which calculation of the orientation of the device is not required to sense the physiological tremor in 3 DOF. 3

MEMS based dual-axis accelerometers are used in the sensing module. Figure 2.5 shows the working of the algorithm.

First, accelerometer readings are sent through a low pass filter (LPF) which filters the low frequency components such as voluntary motion, gravity and jerks. The output from the LPF is subtracted from the original input (respective accelerometer reading) to obtain acceleration due to tremor, noise and residual low frequency acceleration. It was shown that this step is not the same as using a high-pass filter. Unlike a high-pass filter which produces a phase lead, the phase of the output signal obtained from the subtraction of the LPF output with the original input remained the same. However, an offset in magnitude compared to tremor was reported. The output of the subtraction is sent to BMFLC to estimate acceleration of the body frame due to tremor. Acceleration of the needle tip due to tremor is calculated using kinematic equations. Using the rhythmic nature of tremor, the position of needle tip due to tremor is calculated by analytical double-integration.

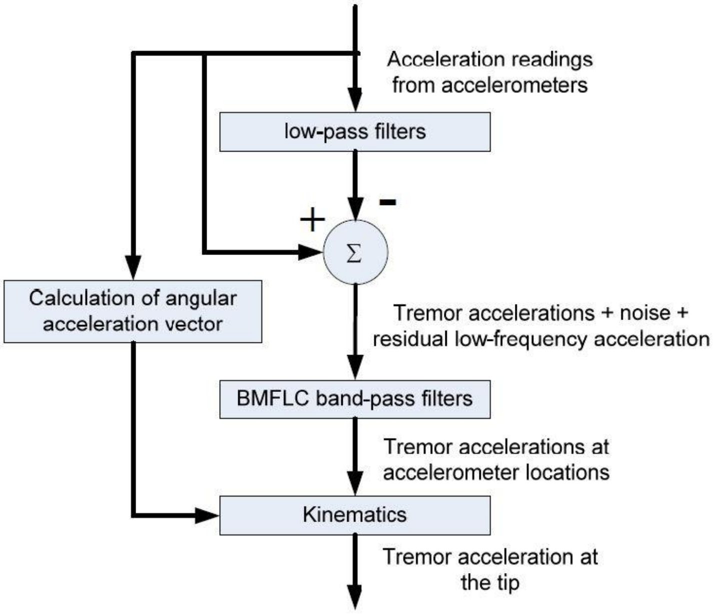

Figure 2.5: Algorithm as reported in [71] to calculate tremor (Copyright © 2009, IEEE)

The following section describes the proposed algorithm to calculate the physiological tremor using the sensed motion from the tri-axial accelerometer and the gyroscopes.

2.3.1.1 Algorithm for calculating real-time physiological tremor

The algorithm is similar in approach to the one reported in [71] with the following modifications: (1) instead of using three dual-axis accelerometer to sense the motion, the IMU presented in Section 2.2 has been used, (2) the gravity factor from the accelerometer measurements has been removed using 2 DOF orientation and (3) the orientation has been estimated using an augmented state Kalman filter. The tremor component in the sensed motion has been calculated using the BMFLC and is defined with respect to the frame $\{S\}$. Figure 2.6 shows the block diagram of the proposed algorithm to calculate the physiological tremor in the hand.

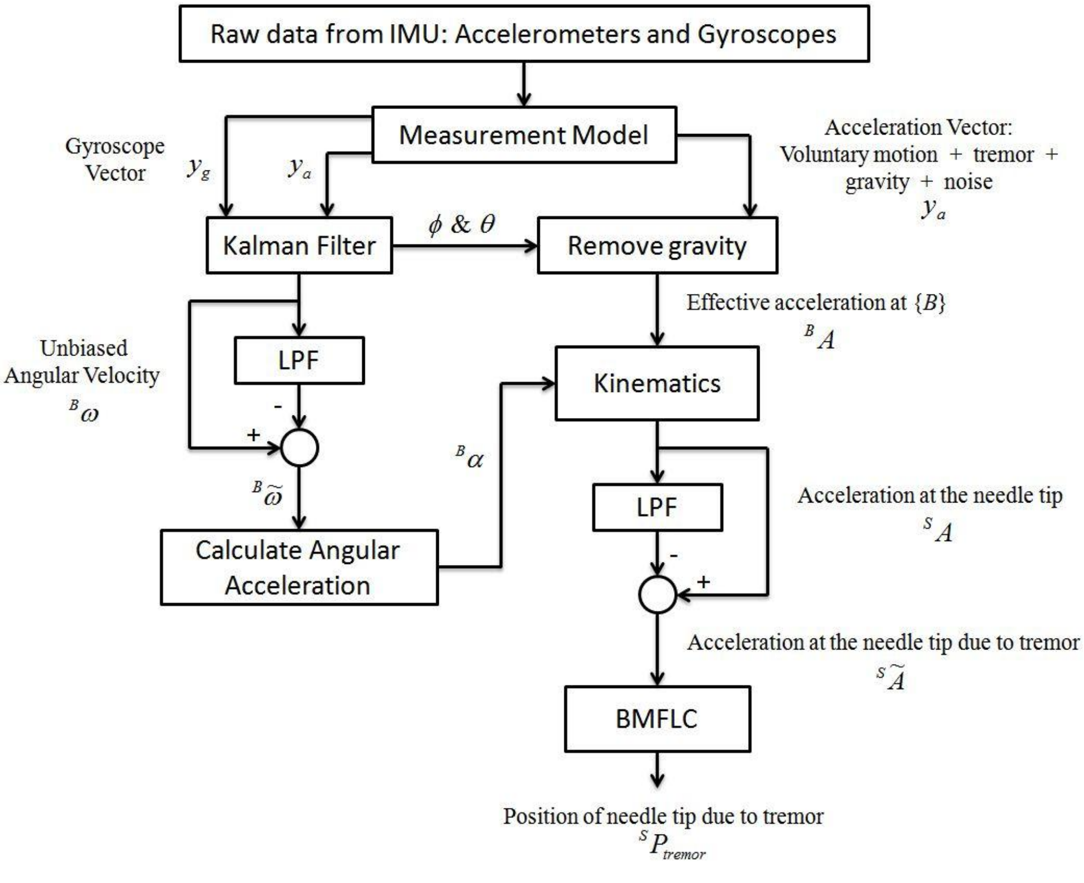

Figure 2.6: Block diagram of the proposed algorithm to calculate physiological tremor.

First, the raw data from the IMU is sent to the measurement model, described in Appendix A, to form acceleration vector y_a (in m/sec^2) and gyroscope vector y_g (in rad/sec). To avoid integration drift in calculating orientation, an augmented state complementary Kalman filter has been developed and is presented in Section 2.4. The Kalman filter provides a drift-free orientation by fusing the accelerometer and gyroscope signals (y_g and y_a). Using the orientation, the gravity vector (${}^{B}G$) is computed and the gravity component in the accelerometer measurements is removed to calculate the effective acceleration as shown in equation 2.11. The effective acceleration with respect to {*B*} can be written as:

$$ {}^{B}A = y_a - {}^{B}G \tag{2.11} $$

$$ {}^{B}A = y_a - ({}^{W}R_B)^{-1}\,{}^{W}G \tag{2.11a} $$

${}^{B}A$ is composed of the acceleration at the body frame {*B*} due to the voluntary motion, the tremor, the residual gravity and the accelerometer noise. As mentioned is the previous section, ${}^{W}R_B$ is the rotation matrix that describes the orientation of body frame {*B*} with respect to world frame {*W*}. The Z-Y-X Euler angle notation has used to describe the rotation matrix since the sensors rotate with the device. It is given by [72]:

$$ \begin{gathered} {}^{W}R_{B,(ZYX)} = R_Z(\varphi)R_Y(\theta)R_X(\phi) \\ {}^{W}R_{B,(ZYX)} = \begin{bmatrix} c\varphi c\theta & c\varphi s\theta s\phi - s\varphi c\phi & c\varphi s\theta c\phi + s\varphi s\phi \\ s\varphi c\theta & s\varphi s\theta s\phi + c\varphi c\phi & s\varphi s\theta s\phi - c\varphi s\phi \\ -s\theta & c\theta s\phi & c\theta c\phi \end{bmatrix} \end{gathered} \tag{2.12} $$

$$ {}^{W}R_{B,(ZYX)} = \begin{bmatrix} {}^{B}X_W & {}^{B}Y_W & {}^{B}Z_W \end{bmatrix}^T \tag{2.12a} $$

where $c\varphi = \cos\varphi, s\varphi = \sin\varphi$ and so on. ϕ, θ and φ (roll, pitch and yaw) represent Euler angles which are defined as angular rotations about X_B, Y_B and Z_B respectively. In a vector form, the Euler angles can be written as: $\Psi = [\theta \quad \phi \quad \varphi]^T$.

Considering that ${}^{W}G$ is given by $g[0 \quad 0 \quad 1]^T$ and the inverse of the rotation matrix is its transpose, equation 2.11a becomes:

$$\begin{bmatrix} {}^{B}a_x \\ {}^{B}a_y \\ {}^{B}a_z \end{bmatrix} = \begin{bmatrix} y_{a,x} \\ y_{a,y} \\ y_{a,z} \end{bmatrix} - g\begin{bmatrix} -s\theta \\ c\theta s\phi \\ c\theta c\phi \end{bmatrix} \tag{2.13}$$

It is clear from equation 2.13 that removing the gravity factor from the accelerometer measurements only depends on 2 DOF orientation, θ and ϕ. The acceleration at the needle tip with respect to $\{S\}$ is composed of the acceleration of the device at $\{B\}$, centripetal acceleration and tangential acceleration:

$${}^{S}A = {}^{B}A + {}^{B}\omega \otimes ({}^{B}\omega \otimes {}^{B}P_{tip}) + {}^{B}\alpha \otimes {}^{B}P_{tip} \tag{2.14}$$

where ${}^{B}P_{tip}$ is given by $[0 \quad 0 \quad 0.19]^T$ and ${}^{B}\alpha$ is the angular acceleration vector and is given by $\left[{}^{B}\alpha_x \quad {}^{B}\alpha_y \quad {}^{B}\alpha_z\right]^T$. For microsurgical procedures, the centripetal acceleration term ($\left|{}^{B}\omega^2\right|$) is very small and can be ignored. Therefore, equation 2.14 becomes:

$${}^{S}A = {}^{B}A + {}^{B}\alpha \otimes {}^{B}P_{tip} \tag{2.15}$$

Equation 2.15 can be written as:

$$\begin{bmatrix} {}^{S}a_x \\ {}^{S}a_y \\ {}^{S}a_z \end{bmatrix} = \begin{bmatrix} {}^{B}a_x \\ {}^{B}a_y \\ {}^{B}a_z \end{bmatrix} + 0.19\begin{bmatrix} -{}^{B}\alpha_y \\ {}^{B}\alpha_x \\ 0 \end{bmatrix} \tag{2.16}$$

${}^{S}A$ is composed of the acceleration at the needle tip due to voluntary motion, tremor, residual gravity and accelerometer noise. In [71], the authors reported that the BMFLC produces inaccurate results if the magnitude of the frequency components outside the pass-band is larger compared to the magnitude of the frequency components within the pass-band. Since the magnitude of the acceleration due to the voluntary motions can be larger than the magnitude of the acceleration due to tremor, ${}^{S}A$ is first sent to a fourth-order low pass filter (LPF) with a cut-off frequency of 4 Hz. The output of the LPF is subtracted from its original input (${}^{S}A$) as shown in Figure 2.6. This step removes the acceleration due to the voluntary motions and the residual gravity factor without changing the phase of the signal and provides acceleration due to tremor, residual low frequency components and the accelerometer noise (${}^{S}\tilde{A}$). ${}^{S}\tilde{A}$ is sent to the BMFLC which estimates the acceleration of the needle tip with respect to $\{S\}$ due to the tremor. The position of the needle tip due to the tremor with respect to $\{S\}$ is calculated by analytical double integration inside the BMFLC algorithm using the rhythmic nature of tremor and is described in Section 2.5.2.

It is clear from equations 2.13 and 2.16 that the orientation in 2 DOF (θ and ϕ) and the angular acceleration about X_B and Y_B axes (${}^{B}\alpha_x$ and ${}^{B}\alpha_y$) are required to calculate the acceleration at the needle tip with respect to $\{S\}$. The angular acceleration is calculated using the angular velocity measured by the gyroscopes:

$$ {}^{B}\alpha_{i,k} = \frac{{}^{B}\omega_{i,} - {}^{B}\omega_{i,k-1}}{T} \tag{2.17} $$

where $i = x$ and y. The orientation in 2 DOF is estimated using an augmented state complementary Kalman filter and is presented in Section 2.4. Since the gyroscopes suffer with bias drift, the angular velocity measured using the gyroscopes drifts over time. The proposed Kalman filter models for the bias and provides the un-biased angular velocity about X_B and Y_B axes (${}^{B}\hat{\omega}_x$ and ${}^{B}\hat{\omega}_y$). It is composed of the angular velocity due to the voluntary motions, the involuntary motions, residual bias and the noise. The angular velocity provided by the Kalman filter is, first, sent to a fourth order LPF with a cut-off frequency of 4 Hz. The output of the LPF is subtracted from its original input (the angular velocity provided by the Kalman filter) as shown in Figure 2.6. This step removes the angular velocity due to the voluntary motions and the residual bias without changing the phase of the signal and provides angular velocity (${}^{B}\tilde{\omega}_x$ and ${}^{B}\tilde{\omega}_y$) that only contains components due to the tremor, residual low frequency components and the noise. This is used to calculate the angular acceleration about X_B and Y_B axes using equation 2.17.

2.4 Orientation using gyroscopes and accelerometers

2.4.1 Literature Review

Extensive research has been conducted to calculate orientation during human body movements using inertial sensors. Depending on the type and number of sensors used, a few studies were focused on tracking orientation in 3 DOF, while others on 2 DOF. This section presents a brief literature review on the related work.

In [73], the authors reported 2 commercial sensing modules to track orientation in 3 DOF. Both were composed of a triad of accelerometers, a triad of rate gyroscopes and a triad of magnetometers to track head mounted displays. Orientation was calculated using a complementary separate bias Kalman filter [74]. The filter relied solely on gyroscopes to estimate orientation during body movements and the drift was corrected only during stationary periods using accelerometers and magnetometers. The state vector contained orientation errors and bias errors. However, the gyro bias was not explicitly modeled. The process and measurement error covariance matrices were calculated by experimental tweaking.

The authors in [75] presented a 9 DOF sensing module called MARG to track orientation in 3 DOF. MARG is composed of a triple axis magnetometer, a triple axis gyroscope and a triple axis accelerometer. A quaternion-based complementary filter was used to calculate the 3 DOF orientation. In [76], the complementary filter was replaced with a quaternion-based extended Kalman filter. Further improvements to this were reported in [77] and [78]. A reduced-order Gauss-Newton method was used to obtain the quaternion to make Kalman filter computationally efficient. In [79], the authors replaced the reduced-order Gauss Newton method by two algorithms named- QUEST [80] and Factored Quaternion Algorithm [81] [82], that take a set of accelerometer and magnetometer measurements to calculate the quaternion. The covariance matrices were obtained through experimental observations. Lag and overshoots were reported in [79] during fast motion.

Using triple axis gyroscopes and a triple axis accelerometer, authors in [83] [84] [85] presented a complementary Kalman filter for estimating orientation in 3 DOF. The accelerometer was used to correct for the drift in roll and pitch. The drift in yaw was corrected using a kinematic human body model and the gyro bias was modeled as a Gauss Markov process. The authors in [86] incorporated magnetometers and extended the work described in [84] to compensate for drift in yaw and magnetic disturbances. This significantly improved the orientation estimates in comparison to no compensation for magnetic disturbances or using gyroscopes only. Further improvements to this work were reported in [87] and [88].

The authors in [89] presented a sensing module that eliminated gyroscopes and used six accelerometers and magnetic sensors to calculate complete 3 DOF orientation. In [90], the authors presented a quaternion-based Kalman Filter. The TRAID algorithm [80], which uses both accelerometer and magnetometer measurements, was used to obtain the orientation. The noise characteristics of the sensors were determined using Allan variance analysis. The process covariance matrix was obtained using a scaled unscented transformation and the measurement covariance matrix was derived analytically.

In [91], the authors presented a Kalman filter to estimate orientation in 2 DOF (roll and pitch) by using a triple axis gyroscope and a triple axis accelerometer. Two Kalman filters were used, one for motion during low acceleration and the other during high acceleration. A switching mechanism, which detected acceleration, was used to drive the corresponding Kalman filter. Moreover, the gyro bias was not modeled in this work.

In the current implementation of AID, we have employed an augmented state complementary Kalman filter to estimate 2-DOF orientation (ϕ and θ) and is presented in the following section.

2.4.2 Augmented State Complementary Kalman Filter

An augmented state complementary Kalman filter has been designed to estimate 2 DOF orientation of the device ($\theta \,\&\, \phi$) by fusing gyroscope and accelerometer signals. The flowchart showing the working of the Kalman filter is shown in Figure 2.7. Θ is the orientation vector containing θ and ϕ, and b is a vector containing the gyro biases. A hat on top denotes an estimate, a minus superscript denotes an *apriori* estimate and a plus superscript denotes an estimate corrected by the Kalman filter. A term without a hat denotes an actual value.

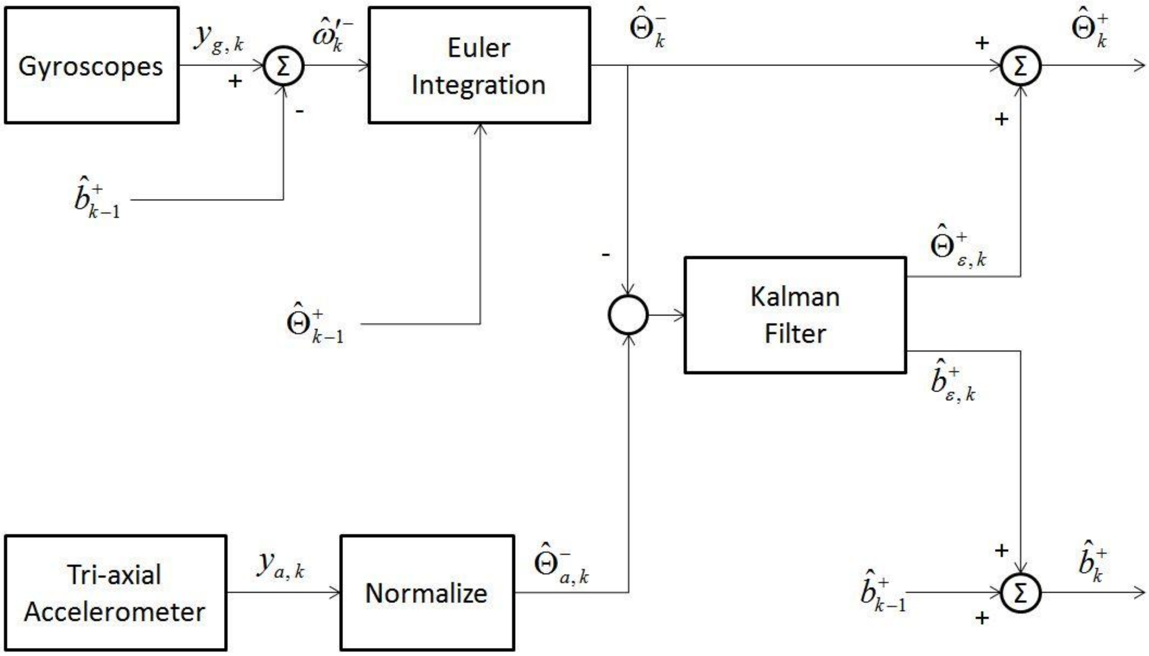

Figure 2.7: Block diagram of the augmented state complementary Kalman filter

The orientation is estimated by both gyroscopes and tri-axial accelerometer, each with some amount of error. The orientation estimated using the gyroscopes is used as reference. The orientation estimated using the gyroscopes suffers from integration drift and the orientation estimated using the tri-axial accelerometer is noisy and vulnerable to vibrations. The difference in orientation estimates ($\hat{\Theta}_{a,k}^- - \hat{\Theta}_k^-$) is used as an input for the Kalman filter to estimate the orientation and bias errors ($\hat{\Theta}_{\varepsilon,k}^+$ & $b_{\varepsilon,k}^+$). These errors are then used to correct the orientation estimated using the gyroscope and the gyro biases respectively.

2.4.2.1 Sensor Model

The signal measured by the tri-axial accelerometer (y_a) is modeled as a sum of inertial acceleration (${}^{B}A$), gravity (${}^{B}G$) and white Gaussian noise (v_a):

$$y_{a,k} = {}^{B}A_k + {}^{B}G_k + v_{a,k} \tag{2.18}$$

where $y_a = [y_{a,x} \quad y_{a,y} \quad y_{a,z}]^T$ and ${}^{B}A = [{}^{B}a_x \quad {}^{B}a_y \quad {}^{B}a_z]^T$.

The signal measured by the dual-axis gyroscope (${}^{G1}y_g$), IDG 500, is modeled as a sum of angular velocity (${}^{G1}\omega$), slowly varying gyro bias (b) and white Gaussian noise (${}^{G1}v_g$):

$${}^{G1}y_{g,k} = {}^{G1}\omega_k + b_k + {}^{G1}v_{g,k} \tag{2.19}$$

where ${}^{G1}y_g = \left[{}^{G1}y_{g,x} \quad {}^{G1}y_{g,y}\right]^T$, ${}^{G1}\omega = \left[{}^{G1}\omega_x \quad {}^{G1}\omega_y\right]^T$, $b = \left[b_x \quad b_y\right]^T$ and ${}^{G1}v_g = \left[{}^{G1}v_{g,x} \quad {}^{G1}v_{g,y}\right]^T$.

The gyro bias (b) is modeled as a realization of a first order Gauss-Markov process driven by white Gaussian noise (w_b):

$$b_k = b_{k-1} + w_{b,k} \tag{2.20}$$

where $w_b = \left[w_{b,x} \quad w_{b,y}\right]^T$.The signal measured by the single-axis gyroscope (${}^{G2}y_g$), MLX 90609, is modeled as a sum of angular velocity (${}^{G2}\omega$), a constant gyro bias (b'_0) and white Gaussian noise (${}^{G2}v_g$):

$${}^{G2}y_{g,k} = {}^{G2}\omega_k + b'_0 + {}^{G2}v_{g,k} \tag{2.21}$$

where ${}^{G2}\omega = {}^{G2}\omega_z$. The initial bias for the gyroscopes is obtained during the calibration of the IMU and is presented in Appendix A. The white Gaussian noises v_a, ${}^{G1}v_g$, ${}^{G2}v_g$ and w_b are assumed to be non-correlated. The angular velocity of the device with respect to $\{B\}$ can be written as:

$${}^{B}\omega = \left[{}^{B}\omega_x \quad {}^{B}\omega_y \quad {}^{B}\omega_z\right]^T \tag{2.22}$$

Since the principal axes of gyro frames {*G1*} and {*G2*} are opposite in direction to the direction of the principal axes of the body frame {*B*}, the angular velocity with respect to {*B*} can be written as:

$$^{B}\omega = \begin{bmatrix} -^{G1}\omega_x & -^{G1}\omega_y & -^{G2}\omega_z \end{bmatrix}^T \tag{2.23}$$

$$^{B}\omega = \begin{bmatrix} ^{B}\omega' & ^{B}\omega_z \end{bmatrix}^T \tag{2.23a}$$

Using equations 2.23 and 2.19, $^{B}\omega'$ can written as:

$$^{B}\omega'_k = -^{G1}y_{g,k} + b_k + ^{G1}v_{g,k} \tag{2.24}$$

where $^{B}\omega' = \begin{bmatrix} ^{B}\omega_x & ^{B}\omega_y \end{bmatrix}^T = \begin{bmatrix} -^{G1}\omega_x & -^{G1}\omega_y \end{bmatrix}^T$.

2.4.2.2 State Space Model

A complementary Kalman filter works on a state-space model that describes the relationship between input (difference in orientation estimate) and states (orientation and bias errors). Such a filter operates on the errors in predicting the 2 DOF orientation (ϕ and θ) and gyro biases (b_x and b_y).

The discrete state-space model used by the filter to estimate the orientation and gyro bias errors is given by:

$$x_{\varepsilon,k} = A_k x_{\varepsilon,k-1} + \xi_k \tag{2.25}$$

$$z_{\varepsilon,k} = H_k x_{\varepsilon,k} + \zeta_k \tag{2.26}$$

Equation 2.25 is the process model and equation 2.26 is the measurement model. x_ε is the error state vector and A is the state propagation matrix. z_ε is the measurement vector and H is the measurement matrix. ξ_k is the zero mean Gaussian white process noise with covariance Q_k. ζ_k is the zero mean Gaussian white measurement noise with covariance R_k. In the following sections, we derive the process and measurement models.

2.4.2.3 Process Model

The relationship between angular velocity (${}^{B}\omega = \left[{}^{B}\omega_x \quad {}^{B}\omega_y \quad {}^{B}\omega_z\right]^T$) of the device and the rate of change of Euler angles ($\dot{\Psi} = \left[\dot{\phi} \quad \dot{\theta} \quad \dot{\varphi}\right]^T$) is given by:

$$\dot{\Psi} = L\,{}^{B}\omega \tag{2.27}$$

where L is a transformation matrix given by:

$$L = \begin{bmatrix} 1 & \sin\phi\tan\theta & \cos\phi\tan\theta \\ 0 & \cos\phi & -\sin\phi \\ 0 & \sin\phi\sec\theta & \cos\phi\sec\theta \end{bmatrix} \tag{2.27a}$$

Equation (2.27) can be written as:

$$\dot{\Psi} = \begin{bmatrix} {}^{B}\omega_x + {}^{B}\omega_y \sin\phi\tan\theta + {}^{B}\omega_z \cos\phi\tan\theta \\ {}^{B}\omega_y \cos\phi - {}^{B}\omega_z \sin\phi \\ {}^{B}\omega_y \sin\phi\sec\theta + {}^{B}\omega_z \cos\phi\sec\theta \end{bmatrix} \tag{2.28}$$

Equation (2.28) is a set of differential equations. The Euler method has been selected to solve equation 2.28. Therefore, in discrete-time format, Ψ can be updated using:

$$\Psi_k = \Psi_{k-1} + L_{k-1}\,{}^{B}\omega_k T \tag{2.29}$$

where T is the sampling time. Equation (2.29) calculates all the three Euler angles. Since only ϕ and θ are required for the algorithm presented in the previous section, we define a 2 DOF orientation vector:

$$\Theta = \left[\phi \quad \theta\right]^T \tag{2.30}$$

The transformation matrix L can be reduced to a 2x3 matrix in order to calculate θ and ϕ:

$$J = \begin{bmatrix} 1 & \sin\phi\tan\theta & \cos\phi\tan\theta \\ 0 & \cos\phi & -\sin\phi \end{bmatrix} \tag{2.31}$$

Θ can be updated using:

$$\Theta_k = \Theta_{k-1} + J_{k-1}\,{}^{B}\omega_k T \tag{2.32}$$

$$\begin{bmatrix} \phi_k \\ \theta_k \end{bmatrix} = \begin{bmatrix} \phi_{k-1} \\ \theta_{k-1} \end{bmatrix} + \begin{bmatrix} 1 & \sin\phi_{k-1}\tan\theta_{k-1} & \cos\phi_{k-1}\tan\theta_{k-1} \\ 0 & \cos\phi_{k-1} & -\sin\phi_{k-1} \end{bmatrix} \begin{bmatrix} {}^{B}\omega_{x,k} \\ {}^{B}\omega_{y,k} \\ {}^{B}\omega_{z,k} \end{bmatrix} T \tag{2.33}$$

Equation 2.33 can also be written as:

$$\begin{bmatrix} \phi_k \\ \theta_k \end{bmatrix} = \begin{bmatrix} \phi_{k-1} \\ \theta_{k-1} \end{bmatrix} + \begin{bmatrix} 1 & \sin\phi_{k-1}\tan\theta_{k-1} \\ 0 & \cos\phi_{k-1} \end{bmatrix} \begin{bmatrix} {}^{B}\omega_{x,k} \\ {}^{B}\omega_{y,k} \end{bmatrix} + \begin{bmatrix} \cos\phi_{k-1}\tan\theta_{k-1} \\ -\sin\phi_{k-1} \end{bmatrix} \begin{bmatrix} {}^{B}\omega_{z,k} \end{bmatrix} \tag{2.34}$$

Using equation 2.23a, equation 2.34 can be written as:

$$\Theta_k = \Theta_{k-1} + J'_{k-1}\,{}^{B}\omega'_k T + J'_{z,k-1}\,{}^{B}\omega_{z,k} T \tag{2.35}$$

Using equations 2.19, 2.21 and 2.23, equation 2.35 becomes:

$$\Theta_k = \Theta_{k-1} + J'_{k-1}(-{}^{G1}y_{g,k} + b_k + {}^{G1}v_{g,k})T + J'_{z,k-1}(-{}^{G2}y_{g,k-1} + b'_0 + {}^{G2}v_{g,k})T \tag{2.36}$$

Using the gyro bias model in equation (2.20), equation (2.36) can be rewritten as:

$$\begin{gathered} \Theta_k = \Theta_{k-1} + J'_{k-1}(-{}^{G1}y_{g,k} + b_{k-1} + w_{b,k} + {}^{G1}v_{g,k})T + \\ J'_{z,k-1}(-{}^{G2}y_{g,k-1} + b'_0 + {}^{G2}v_{g,k})T \end{gathered} \tag{2.37}$$

$$\begin{gathered} \Theta_k = \Theta_{k-1} + J'_{k-1}(-{}^{G1}y_{g,k} + b_{k-1} + w_{b,k})T + \\ J'_{z,k-1}(-{}^{G2}y_{g,k-1} + b'_0)T + J_{k-1}v_{g,k}T \end{gathered} \tag{2.37a}$$

$$\Theta_k = f(\Theta_{k-1}, J'_{k-1}, J'_{z,k-1}, {}^{G1}y_{g,k}, {}^{G2}y_{g,k}, b_{k-1}, b'_0, w_{b,k}, {}^{G1}v_{g,k}, {}^{G2}v_{g,k}, T) \tag{2.38}$$

v_g in equation 2.37a is given by $\begin{bmatrix} {}^{G1}v_{g,x} & {}^{G1}v_{g,y} & {}^{G2}v_g \end{bmatrix}^T$. *f* in equation (2.38) is a non-linear function that relates vector Θ at time step *k* to the vector Θ at previous time step *k-1*.

Consider augmenting the orientation vector (Θ) and the bias vector (b) using equation (2.37) and (2.20):

$$\begin{bmatrix} \Theta_k \\ b_k \end{bmatrix} = \begin{bmatrix} I_{2x2} & J'_{k-1}T \\ 0_{2x2} & I_{2x2} \end{bmatrix} \begin{bmatrix} \Theta_{k-1} \\ b_{k-1} \end{bmatrix} + \begin{bmatrix} -J'_{k-1}T \\ 0_{2x2} \end{bmatrix} {}^{G1}y_{g,k} + \begin{bmatrix} J'_{z,k-1} \\ 0_{2x1} \end{bmatrix} (-{}^{G2}y_{g,k} + b'_0) + \begin{bmatrix} J_{k-1}T & J'_{k-1}T \\ 0_{2x3} & I_{2x2} \end{bmatrix} \begin{bmatrix} v_{g,k} \\ w_{b,k} \end{bmatrix} \tag{2.39}$$

where I_{2x2} is 2x2 identity matrix. 0_{2x2}, 0_{2x1} and 0_{2x3} are 2x2, 2x1 and 2x3 zero matrices respectively. Equation 2.39 can be written in a state-space format as:

$$x_k = a_k x_{k-1} + B_k {}^{G1}y_{g,k} + c_k(-{}^{G2}y_{g,k} + b'_0) + W_k w_k \tag{2.40}$$

Equation (2.40) defines the actual state propagation equation for state x_k. w_k is the zero mean Gaussian white noise with covariance $\tilde{Q}_k$. It should be noted that x_k is the *actual* state vector.

Since the values of $w_{b,k}$ and $v_{g,k}$ are unknown, x_k can be estimated by keeping them zero in equations 2.19, 2.20 and 2.21 and then using equation 2.40. The gyro bias in the dual-axis gyroscope, IDG 500, is estimated using equation 2.20 by keeping $w_{b,k}$ as zero:

$$\hat{b}_k^- = \hat{b}_{k-1}^+ \tag{2.41}$$

The angular velocity vector (${}^B\hat{\omega}_k'^-$) is estimated by keeping white noise ${}^{G1}v_{g,k}$ as zero in equation 2.24:

$${}^B\hat{\omega}_k'^- = -{}^{G1}y_{g,k} + \hat{b}_{k-1}^+ \tag{2.42}$$

Θ_k is estimated using the following equation:

$$\hat{\Theta}_k^- = \hat{\Theta}_{k-1}^+ + \hat{J}'^+_{k-1}\, {}^B\hat{\omega}_k'^- T + \hat{J}'^+_{k-1}\, {}^B\omega_{z,k} T \tag{2.43}$$

Using equations 2.19, 2.20, 2.21, 2.41 and 2.42, equation 2.43 can be written as:

$$\hat{\Theta}_k^+ = \hat{\Theta}_{k-1}^+ + \hat{J}'^+_{k-1}(-{}^{G1}y_{g,k} + \hat{b}^+_{k-1})T + \hat{J}'^+_{z,k-1}(-{}^{G2}y_{g,k-1} + b'_0)T \qquad (2.44)$$

$$\hat{\Theta}_k^- = f(\hat{\Theta}^+_{k-1}, \hat{J}'^+_{k-1}, \hat{J}'^+_{z,k-1}, {}^{G1}y_{g,k}, {}^{G2}y_{g,k}, \hat{b}^+_{k-1}, b'_0, 0,0,0, T) \qquad (2.45)$$

Consider augmenting the orientation vector ($\hat{\Theta}$) and the bias vector ($\hat{b}$):

$$\begin{bmatrix} \hat{\Theta}_k^- \\ \hat{b}_k^- \end{bmatrix} = \begin{bmatrix} I_{2x2} & \hat{J}'^+_{k-1}T \\ 0_{2x2} & I_{2x2} \end{bmatrix} \begin{bmatrix} \hat{\Theta}^+_{k-1} \\ \hat{b}^+_{k-1} \end{bmatrix} + \begin{bmatrix} -\hat{J}'^+_{k-1}T \\ 0_{2x2} \end{bmatrix} {}^{G1}y_{g,k} + \begin{bmatrix} \hat{J}'^+_{k-1} \\ 0_{2x1} \end{bmatrix} (-{}^{G2}y_{g,k} + b'_0) \qquad (2.46)$$

Equation (2.46) can be written in a state space format as:

$$x_k = \hat{a}^+_{k-1}\hat{x}^+_{k-1} + \hat{B}^+_{k-1}\,{}^{G1}y_{g,k} + \hat{c}^+_{k-1}(-{}^{G2}y_{g,k} + b'_0) \qquad (2.47)$$

$\hat{x}_k^-$ is the *predicted* state vector and $\hat{x}^+_{k-1}$ is the *corrected* estimate of the state at time *k-1*.

2.4.2.3.1 Error State Vector

In order to obtain a complementary Kalman filter, an *error* state vector is selected which is defined as the difference between the actual state vector and the predicted state vector:

$$x_\varepsilon = x_k - \hat{x}_k \qquad (2.48)$$

$$\begin{aligned} x_\varepsilon &= \begin{bmatrix} \Theta_\varepsilon & b_\varepsilon \end{bmatrix}^T \\ x_\varepsilon &= \begin{bmatrix} \phi_\varepsilon & \theta_\varepsilon & b_{x,\varepsilon} & b_{y,\varepsilon} \end{bmatrix}^T \end{aligned} \qquad (2.48a)$$

where Θ_ε is the error in predicting Euler angles and b_ε is the error in predicting gyro biases, b_x and b_y.

2.4.2.3.2 Discrete Error State Equation

Since *f* is a non-linear function, the linearized error dynamics for the orientation vector at time step *k* can be obtained by linearizing the orientation vector about equation 2.43 to obtain:

$$x_{\varepsilon,\,k} = A_k\, x_{\varepsilon,\,k-1} + \xi_k \tag{2.49}$$

where the state transition matrix is given by:

$$A_k = \begin{bmatrix} A_{\Theta\Theta} & A_{\Theta b} \\ 0_{(2x2)} & I_{(2x2)} \end{bmatrix} \tag{2.49a}$$

$A_{\Theta\Theta}$ and $A_{\Theta b}$ are the Jacobian matrices of partial derivatives of f with respect to Θ and b respectively:

$$A_{\Theta\Theta} = \frac{\partial f}{\partial \Omega}(\hat{\Theta}^{+}_{k-1}, \hat{J}'^{+}_{k-1}, \hat{J}'^{+}_{z,k-1}, {}^{G1}y_{g,k}, {}^{G2}y_{g,k}, \hat{b}^{+}_{k-1}, b'_0, 0,0,0, T) = I_{2x2} + F_k T \tag{2.50a}$$

$$A_{\Theta b} = \frac{\partial f}{\partial b}(\hat{\Theta}^{+}_{k-1}, \hat{J}'^{+}_{k-1}, \hat{J}'^{+}_{z,k-1}, {}^{G1}y_{g,k}, {}^{G2}y_{g,k}, \hat{b}^{+}_{k-1}, b'_0, 0,0,0, T) = \hat{J}'^{+}_{k-1} T \tag{2.50b}$$

$$F_k = \begin{bmatrix} {}^{B}\hat{\omega}^{-}_{y,k} c\hat{\phi}^{-}_k t\hat{\theta}^{-}_k - {}^{B}\omega_{z,k} s\hat{\phi}^{-}_k t\hat{\theta}^{-}_k & ({}^{B}\hat{\omega}^{-}_{y,k} s\hat{\phi}^{-}_k)/c^2\hat{\theta}^{-}_k + ({}^{B}\omega_{z,k} c\hat{\phi}^{-}_k)/c^2\hat{\theta}^{-}_k \\ -{}^{B}\hat{\omega}^{-}_{y,k} s\hat{\phi}^{-}_k - {}^{B}\omega_{z,k} c\hat{\phi}^{-}_k & 0 \end{bmatrix} \tag{2.50c}$$

where $c\hat{\phi}^{-}_k = \cos\hat{\phi}^{-}_k$, $s\hat{\phi}^{-}_k = \sin\hat{\phi}^{-}_k$, $t\hat{\theta}^{-}_k = \tan\hat{\theta}^{-}_k$ and so on.

2.4.2.3.3 Process Noise Covariance Matrix

ξ_k is the zero mean Gaussian white process noise with covariance Q_k. The process noise covariance matrix is given by:

$$Q_k = W_k \tilde{Q}_k W_k \tag{2.51}$$

$$\tilde{Q}_k = \begin{bmatrix} \sigma^2_{g,x} & 0 & 0 & 0 & 0 \\ 0 & \sigma^2_{g,y} & 0 & 0 & 0 \\ 0 & 0 & \sigma^2_{g,z} & 0 & 0 \\ 0 & 0 & 0 & \sigma^2_{b,x} & 0 \\ 0 & 0 & 0 & 0 & \sigma^2_{b,y} \end{bmatrix} \tag{2.51a}$$

$\sigma^2_{g,x}$, $\sigma^2_{g,y}$ and $\sigma^2_{g,z}$ are the variance of ${}^{G1}v_{g,x}$, ${}^{G1}v_{g,y}$ and ${}^{G2}v_{g,z}$ respectively. $\sigma^2_{b,x}$ and $\sigma^2_{b,y}$ are the variance of $w_{b,x}$ and $w_{b,y}$, respectively.

2.4.2.4 Measurement Model

To estimate the inclination using an accelerometer, the accelerometer data is first normalized (Appendix A). The normalized accelerometer data can be written as:

$$ {}^{B}A_n = \begin{bmatrix} {}^{B}a_{x,n} & {}^{B}a_{y,n} & {}^{B}a_{z,n} \end{bmatrix}^T \tag{2.52}$$

Since, the accelerometer also measures gravity, ${}^{B}Z_W$ can be written as:

$$ {}^{B}Z_W = \frac{{}^{B}A_n}{|\,{}^{B}A_n\,|} = [-s\theta \quad c\theta s\phi \quad c\theta c\phi]^T \tag{2.53}$$

Using equation 2.53, the inclination angles estimated using the accelerometer is given by:

$$ \hat{\theta}_a^- = \operatorname{atan2}\left(\frac{-{}^{B}a_{x,n}}{\sqrt{{}^{B}a^2_{y,n} + {}^{B}a^2_{z,n}}} \right) \tag{2.54a}$$

$$ \hat{\phi}_a^- = \operatorname{atan2}\left(\frac{{}^{B}a_{y,n}}{\sqrt{{}^{B}a^2_{x,n} + {}^{B}a^2_{z,n}}} \right) \tag{2.54b}$$

In vector form, they can be written as:

$$ \hat{\Theta}_a^- = [\hat{\phi}_a^- \quad \hat{\theta}_a^-]^T \tag{2.55}$$

2.4.2.4.1 Measurement Vector

The measurement vector is selected as the difference between the angles calculated using the accelerometer (equation 2.55) and those through Euler integration (equation 2.43):

$$ z_{\varepsilon,k} = \hat{\Theta}_{a,k}^- - \hat{\Theta}_k^- \tag{2.56}$$

2.4.2.4.2 Discrete Measurement Equation

The discrete measurement equation is given by:

$$z_{\varepsilon,k} = Hx_{\varepsilon,k} + \zeta_k \tag{2.57}$$

where ζ is measurement noise vector. Since the measurement vector only contains the orientation errors and not the bias errors, the measurement matrix (*H*) is given by:

$$H = \begin{bmatrix} I_{2x2} & 0_{2x2} \end{bmatrix} \tag{2.58}$$

2.4.2.4.3 Measurement Noise Covariance Matrix

ζ_k is the zero mean Gaussian white measurement noise with covariance R_k. The measurement noise covariance matrix is given by:

$$R_k = \begin{bmatrix} \sigma_\phi^2 & 0 \\ 0 & \sigma_\theta^2 \end{bmatrix} \tag{2.59}$$

where σ_ϕ^2 and σ_θ^2 are the variance of calculating $\hat{\phi}_a^-$ and $\hat{\theta}_a^-$.

2.4.2.5 Kalman Filter

2.4.2.5.1 Predict

Using equation (2.49), the error state is predicted as:

$$\hat{x}_{\varepsilon,k}^- = A_k \hat{x}_{\varepsilon,k-1}^+ \tag{2.60}$$

The projected error covariance is given by:

$$\hat{P}_k^- = A_k \hat{P}_{k-1}^+ A_k^T + Q_k \tag{2.61}$$

2.4.2.5.2 Update

The Kalman gain is obtained using:

$$\tilde{K}_k = \hat{P}_k^- H_k^T (H_k \hat{P}_k^- H_k^T + R_k)^{-1} \tag{2.62}$$

The updated *error* state vector is given by:

$$\hat{x}_{\varepsilon,k}^+ = \hat{x}_{\varepsilon,k}^- + \tilde{K}_k (z_{\varepsilon,k} - H\hat{x}_{\varepsilon,k}^-) \tag{2.63}$$

Equation (2.63) calculates an optimal solution of the error state vector. The updated error covariance is given by:

$$\hat{P}_k^+ = (I - \tilde{K}_k H_k)\hat{P}_k^- \tag{2.64}$$

The *predicted* state vector is corrected using the following equation:

$$\hat{x}_k^+ = \hat{x}_k^- + \hat{x}_{\varepsilon,k}^+ \tag{2.65}$$

Equation (2.65) calculates an optimal value of the orientation and the gyro bias.

2.4.2.5.3 Kalman Filter Initialization

The initialization process sets the initial states and covariances and is run once at the start.

i. At $k = 0$, ϕ_a and θ_a are calculated using the tri-axial accelerometer and used to initialize the orientation vector (Θ_0).

ii. The initial state vector (x_0) is initialized using b_0 and Θ_0.

iii. The initial error state vector ($x_{\varepsilon,0}$) is set to $[0 \quad 0 \quad 0 \quad 0]^T$.

iv. The initial error covariance matrix (P_0) is set to 1000 I where I is a 4x4 identity matrix.

v. The values of variances $\sigma_{g,x}^2, \sigma_{g,y}^2, \sigma_{g,z}^2, \sigma_{b,x}^2, \sigma_{b,y}^2, \sigma_\phi^2$ and σ_θ^2 are set to 3.3e^{-5}, 3.7e^{-5}, 1.5e^{-5}, 1e^{-6}, 1e^{-6}, 7.6e^{-3} and 1e^{-2} respectively.

2.5 Filtering Tremor from Sensed Motion

2.5.1 Introduction

The aim of this section is to estimate the position of the needle tip due to tremor (${}^{S}P_{tremor}$) by filtering the tremor component from acceleration, ${}^{S}\tilde{A}$ and output a negated tremor motion to the manipulator system as control input (${}^{C}P$).

$$ {}^{C}P = -({}^{S}P_{tremor}) \tag{2.66} $$

The conventional filtering techniques such as the Butterworth filter cause a phase change and, thus, cannot be realized for a real-time modeling of physiological tremor. A zero-phase adaptive filter is required to effectively estimate physiological tremor in real-time. An adaptive filter adapts to the variations in frequency and amplitude of the input signal by adjusting its parameters online according to a learning algorithm. One of the popular techniques of adaption is the least mean squares (LMS) algorithm. As physiological tremor is roughly periodic and approximately sinusoidal in nature, a Fourier series model is applicable. The following sections provide a brief overview of Fourier series based zero-phase adaptive filtering algorithms.

2.5.1.1 Fourier Linear Combiner (FLC)

If the frequency of the input signal is *known*, the Fourier Linear Combiner (FLC) algorithm [92] [93] can be used to model the input signal. The FLC is inherently zero phase and has an infinite null [94]. The reference signal is generated by a truncated Fourier series model in which the adaptive filter weights are the Fourier coefficients.

$$ y_k = \sum_{r=1}^{M} [a_r \sin(r\omega_0 k) + b_r \cos(r\omega_0 k)] \tag{2.67} $$

The LMS algorithm is used to update the filter weights. FLC can be written as:

$$ x_{r\,k} = \left\{ \begin{matrix} \sin(r\omega_0 k), & 1 \le r \le M \\ \cos((r-M)\omega_0 k), & M+1 \le r \le 2M \end{matrix} \right\} \tag{2.68} $$

$$\varepsilon_k = s_k - w_k^T x_k \tag{2.69}$$

$$w_{k+1} = w_k + 2\mu x_k \varepsilon_k \tag{2.70}$$

where $w_k = [w_{1_k} \cdots w_{2M_k}]^T$ and $x_k = [x_{1_k} \cdots x_{2M_k}]^T$ are the adaptive weight vector and reference input vector respectively. s_k is the input signal, M is the number of harmonics in the model, μ is an adaptive gain parameter. The algorithm can be viewed as an adaptive notch filter with the width of the notch being directly proportional to μ.

2.5.1.2 Weighted-Frequency Fourier Linear Combiner (WFLC) Algorithm

The FLC algorithm cannot be used to estimate tremor because it only adapts to an input signal of *known* frequency. The authors in [59] and [95] presented an algorithm named, Weighted-frequency Fourier Linear Combiner (WFLC), which is an extension to the FLC, in order to adapt to the input signal of unknown frequencies and amplitude. In contrast to FLC, WFLC also adapts to the frequency of time varying reference signals. WFLC can be written as:

$$x_{rk} = \left\{ \begin{array}{ll} \sin\left((r\sum_{t=0}^{k} \omega_{0_k})\right), & 1 \le r \le M \\ \cos\left((r-M)\sum_{t=0}^{k} \omega_{0_k}\right), & M+1 \le r \le 2M \end{array} \right\} \tag{2.71}$$

$$\varepsilon_k = s_k - w_k^T x_k \tag{2.72}$$

$$\omega_{0_{k+1}} = \omega_{0_k} + 2\mu_0 \varepsilon_k \sum_{r=1}^{M} r\left(\omega_{r_k} x_{M+r_k} - \omega_{M+r_k} x_{r_k}\right) \tag{2.73}$$

$$w_{k+1} = w_k + 2\mu x_k \varepsilon_k \tag{2.74}$$

ω_{0_k} adapts to the unknown frequency of the input signal and w_k estimates the amplitude and phase of the input signal. μ and μ_0 are adaptive gain parameters of amplitude and frequency respectively. In Micron, a combination of WFLC and FLC has been employed to filter the tremor. The amplitude of the input signal is estimated by using x_k from WFLC as the reference input vector in FLC and updating a new set of adaptive weights, $\hat{w}_k$ as shown in the following equations:

$$\hat{\varepsilon}_k = s_k - \hat{w}_k^T x_k \tag{2.75}$$

$$\hat{w}_k = \hat{w}_k + 2\hat{\mu} x_k \hat{\varepsilon}_k \tag{2.76}$$

where $\hat{w}_k = [\hat{w}_{1_k} \cdots \hat{w}_{2M_k}]^T$. While WFLC can adapt to the changes in frequency of the input signal, it was reported in [69] that the performance is degraded by the presence of a modulated signal. In the case of fast variations in frequency in the input signal, the algorithm never gets stabilized and the estimation of the input signal is inaccurate. Also, high frequency noise can change adaptive vectors and thus influence the output of WFLC.

To overcomes the limitations of WFLC, the authors in [69] and [70] presented an algorithm named, Bandlimited Multiple Fourier Linear Combiner (BMFLC) which adapts to multiple frequencies.

2.5.2 Bandlimited Multiple Fourier Linear Combiner (BMFLC) Algorithm

BMFLC [69] [70] is a zero-phase lag adaptive filter which estimates the input signal of unknown multiple frequencies and amplitude. A frequency band is selected with f_0 as the lower cut-off frequency and f as the upper cut-off frequency. The frequency band is divided into a finite number of divisions $L = (f - f_o)G$. G (≥ 1) is the scaling number describing the step-size of the series as shown in Figure 2.8.

The unknown signal is estimated by forming the following series:

$$y_k = \sum_{r=0}^{L} [a_r \sin(2\pi (f_0 + \frac{r}{G}) k) + b_r \cos(2\pi (f_0 + \frac{r}{G}) k)] \tag{2.77}$$

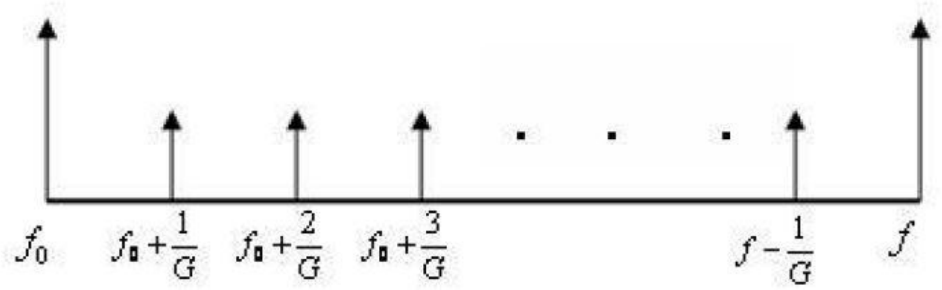

Figure 2.8: BMFLC frequency band and divisions [69] (Copyright © 2007, IEEE)

The LMS algorithm is employed to update the weights a_r and b_r. BMFLC can be written as follows:

$$x_{rk} = \begin{Bmatrix} \sin\left(2\pi\,(f_0 + \frac{r-1}{G})\,k\right), & 1 \le r \le L \\ \cos\left(2\pi\,(f_0 + \frac{(r-L)-1}{G})\,k\right), & L+1 \le r \le 2L \end{Bmatrix} \tag{2.78}$$

$$\varepsilon_k = s_k - w_k^T\, x_k \tag{2.79}$$

$$w_{k+1} = w_k + 2\mu\, x_k\, \varepsilon_k \tag{2.80}$$

where $w_k = [w_{1_k} \cdots w_{2L_k}]^T$ and $x_k = [x_{1_k} \cdots x_{2L_k}]^T$ are the adaptive weight vector and reference input vector respectively. s_k is the input signal and μ is adaptive gain parameter. *G* can be increased depending on the rate of change of frequency in the input signal to enhance the accuracy of estimation.

A comparison between the performance of WFLC and BMFLC was reported in [69]. The following input signal was used for both the algorithms:

$$s_k = 3.5\sin(2\pi f_1 t) + 2.5\cos(2\pi f_2 t) \tag{2.81}$$

The amount of compensation and rms error in adapting to modulated signals using WFLC and BMFLC is shown in Table 2.5.

Table 2.5: Comparison of WFLC and BMFLC [69]

f_1	f_2	WFLC		BMFLC	
		Error (rms)	Compensation (%)	Error (rms)	Compensation (%)
8	8	0.0135	98.7	0.117	96.16
8	8.2	0.5	84.22	0.117	96.16
8	8.6	0.56	81.5	0.116	96.17
8	9	0.765	75.06	0.116	96.17
8	10	1.22	59.83	0.116	96.19
6	12	2.33	23.48	0.124	95.91

Table 2.5 clearly shows that the performance of BMFLC is better in adapting to a modulated signal compared to WFLC. Therefore, we have implemented BMFLC to estimate the tremor component in the sensed motion of the tool-tip.

Since the frequency of physiological tremor ranges from 8 Hz to 12 Hz, f_0 is chosen as 7 Hz and f as 13 Hz with G as 10 so that the resolution is 0.1 Hz. Each element of the acceleration vector at the needle tip with respect to $\{S\}$ (${}^{S}\tilde{A}$) is sent as an input (s_k) to the BMFLC. The acceleration at the needle tip with respect to $\{S\}$ due to tremor is given by:

$$ {}^{S}A_{tremor,k} = \left[{}^{S}A_{tremor,x_k} \quad {}^{S}A_{tremor,y_k} \quad {}^{S}A_{tremor,z_k} \right]^T \tag{2.82} $$

where ${}^{S}A_{tremor,i_k} = w_{i,k}^T x_{i,k}$ ($i = x$, y and z). The position of the needle tip with respect to $\{S\}$ due to tremor is found by analytically double integrating ${}^{S}A_{tremor}$ and is defined as:

$$ {}^{S}P_{tremor,k} = \left[{}^{S}P_{tremor,x_k} \quad {}^{S}P_{tremor,y_k} \quad {}^{S}P_{tremor,z_k} \right]^T \tag{2.83} $$

where ${}^{S}P_{tremor,i_k} = w_{d,i,k}^T x_{i,k}$ and ($i = x$, y and z). The weight for tremor position vector is given by:

$$w_{d,k_r} = \left\{ \begin{array}{ll} \dfrac{-w_{k,r}}{\left(2\pi\,(f_0 + \dfrac{r-1}{G})\right)^2}, & 1 \le r \le L \\ \dfrac{-w_{k,r}}{\left(2\pi\,(f_0 + \dfrac{(r-L)-1}{G})\right)^2}, & L+1 \le r \le 2L \end{array} \right\} \tag{2.84}$$

Chapter 3

3 Design of Actuation System of AID

The chapter presents the design of the actuation system for the Accuracy Improvement Device (AID). Section 3.1 discusses the system requirements of the actuation system. A selection procedure for the actuators is presented in Section 3.2 in which three smart materials- electroactive ceramics (EAC), shape memory alloy (SMA) and ionic polymer metallic composite (IPMC), are compared and IPMC is selected. Section 3.3 presents a review on IPMCs followed by a description of the IPMC-based actuator incorporated in the actuator system of the AID in Section 3.4. The last section, Section 3.5, presents the controller for the IPMC-based actuator.

3.1 System Requirements

In the AID, the tremor is compensated by manipulating the needle-tip in the opposite direction to that of the tremor in real-time. Thus, the goal of the manipulator module is to make the needle tip dynamically track a motion profile that is the negative of the motion profile of the tremor ($-{}^{S}P_{tremor}$).

It was reported in [96] that roughly 75% of the forces measured during retinal microsurgery were less than 7.5 mN with a maximum of 30 mN as shown in Figure 3.1.

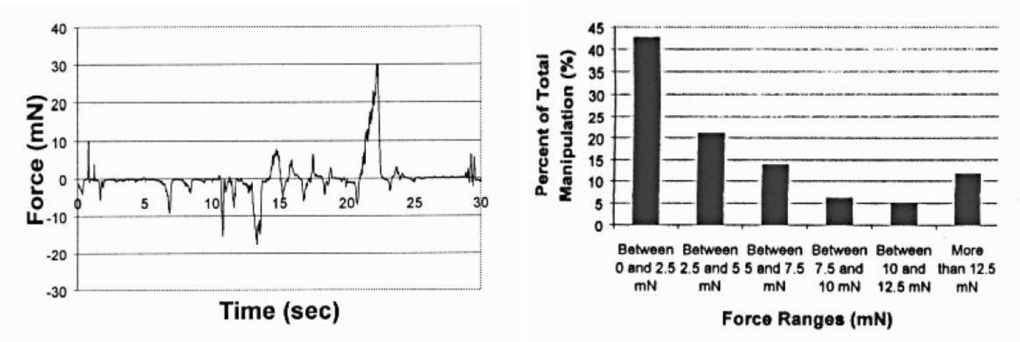

Figure 3.1: Measured forces during retinal microsurgery as reported in [96]. (Left) 30 seconds force trace; (Right) percentage of force ranges (Copyright © 2006, Springer Berlin/Heidelberg)

We again consider tremor having a sinusoidal profile with 8-12 Hz frequency and 70 µm peak-to-peak amplitude to set the system requirements for the manipulator module. The following are the specifications for the actuator:

- Actuator resolution: ≤ 7 µm
- Actuation bandwidth: > 13 Hz
- Actuation force: > 30 mN
- Actuator stroke: ≥ 140 µm

The actuators must also be light and small in size so that a compact manipulator can be designed. Moreover, the actuators must require low power for actuation.

3.2 Actuator Selection

With the system specifications in mind, this section reviews the conventional actuators and the smart materials to identify a potential actuator for the manipulator module of the AID.

3.2.1 Conventional actuators vs. Smart Materials based Actuators

Figure 3.2 shows a graph between the specific actuation stress and the actuation strain for various actuators. Figure 3.3 shows a graph between the blocked stress and the maximum actuation strain for various smart material based actuators. It is evident from Figure 3.2 that hydraulic and pneumatic systems provide the highest specific energy among all the actuators. However, they require bulky equipments such as compressors or pumps which increase the size and the weight of the system. The leakage of fluid in hydraulic systems also poses a serious concern for a medical device.

Although conventional electrical actuators such as solenoids, moving coil transducers or voice coils do not have leakage problems and produce high levels of strain, they do produce significantly less actuation stress compared to smart-material based actuators such as piezoelectric or shape memory alloys (SMA) or ionic metallic polymer composite (IPMC) as shown in Figures 3.2 and 3.3.

Thus, it can be inferred that smart materials can produce the same amount of work as conventional actuators, but with much less weight thereby allowing the hand-held device to be lighter in weight.

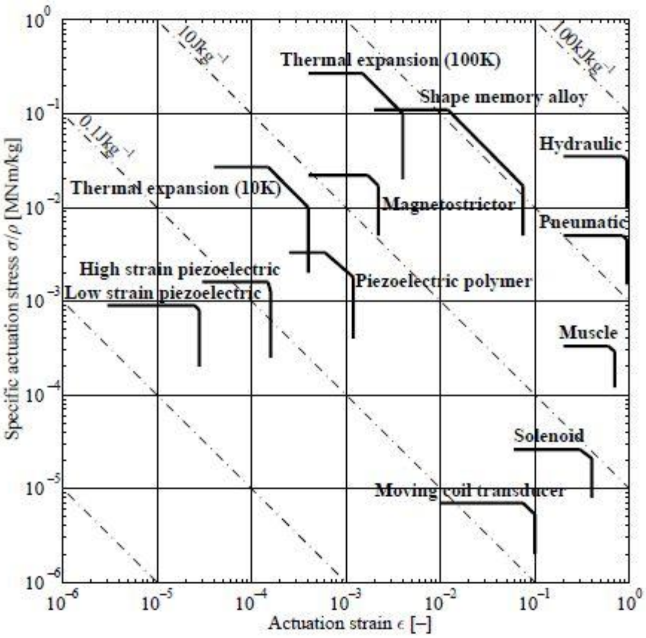

Figure 3.2: Specific actuation stress vs. actuation strain for various actuators [97] (Copyright © 1997, The Royal Society)

Since the size of the actuator is also a design parameter, we now compare the conventional actuators and the smart materials based on volumetric power. Figure 3.4 shows a graph of the power output per unit volume versus efficiency for various actuators. It shows that smart materials such as piezoelectric and SMA can produce higher levels of power per unit volume at the same efficiency compared to solenoids, moving coil transducers or pneumatic systems. This also illustrates that the smart materials can produce the same level of power as conventional actuators, but with less volumes which allows actuators to be incorporated in a small and compact hand-held systems. Since the actuators for a hand-held device must be compact and light in weight and smart materials can produce the same amount of work with smaller size and weight as compared to conventional actuators, smart materials present a viable solution for a hand-held device. The following section presents a comparison between various smart materials and the selection of the most suitable smart material based actuator for our application.

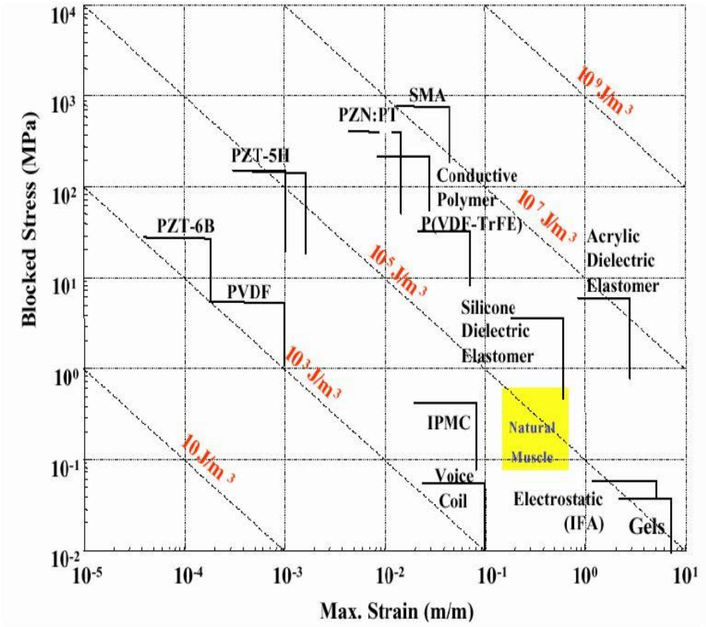

Figure 3.3: Blocked Stress vs. max strain for various smart material actuators [98]

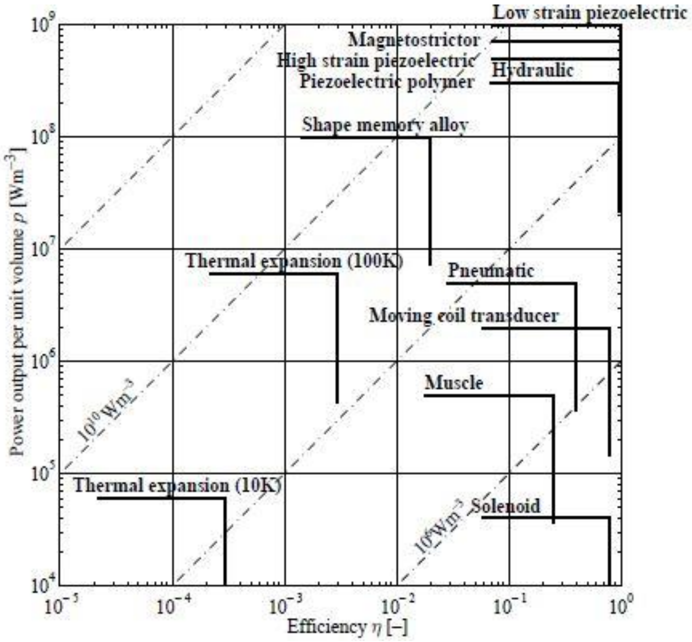

Figure 3.4: Power output per unit volume vs. efficiency for various actuators [97] (Copyright © 1997, The Royal Society)

3.2.2 Smart Materials

Smart materials can be defined as materials that adapt to a change in the physical environment such as electrical, thermal, magnetic, chemical, pH or light environment. Three smart materials: electroactive ceramic (EAC), SMA and IPMC have been selected as potential actuators for the AID and compared based on stroke, bandwidth, force, weight, size, and power requirements. Table 3.1 compares the three actuators on the basis of actuation displacement, force, reaction speed, density, drive voltage and fracture toughness.

Table 3.1: Comparison of IPMC, SMA and EAC [99]

Properties	EAC	SMA	IPMC
Strain	0.1-0.3%	<6%	>3%
Force (MPA)	30-40	~700	10-30
Density (g cm^{-3})	6-8	5-6	2-2.5
Reaction Speed	µs to s	s to min	µs to s
Drive Voltage (V)	50-800	NA	0.1-7
Fracture Toughness	Fragile	Elastic	Resilient, Elastic

EACs (electrostrictor and piezoelectric ceramics) produce mechanical strain in response to an externally applied electrical signal. The maximum strain shown by piezoelectric actuators such as lead zirconate titanate (PZT) is 0.12-0.18% which is significantly lower than the strain shown by IPMCs. EACs have a high actuation bandwidth (upto 1 MHz) [100]. Although EACs can be actuated at the required bandwidth and have necessary stroke (with mechanical amplification) and actuation force, the disadvantages are the high voltage requirement and the higher weight compared to IPMCs as shown in Table 3.1. Moreover, the striction capability of IPMCs can be as high as two orders of magnitude more than EACs [99]. EAC materials are also brittle, and therefore require special packaging and protection. They also exhibit hysteresis upto 10-15% [100].

Shape memory alloys (SMAs) such as Nitinol exhibit a phenomenon, the shape memory effect, which is referred to as the ability to return to the original shape or size from a deformed shape or size under the action of a thermal procedure [101]. SMAs show high level of strain and actuation force as shown in Table 3.1 and Figure 3.3. However, the response time, and thus, the bandwidth is significantly lower than IPMCs as shown in Table 3.1.

Considering the strain, stroke and actuation bandwidth, IPMCs were selected as the actuation modality for the AID. The following section provides a detailed description of IPMCs.

3.3 Ionic Polymer Metallic Composite (IPMC)

3.3.1 Brief History

Although polymer-metal composites were developed in 1939 by precipitation of colloidal silver on prepared substrates, IPMCs were developed in early 1990s as solid electrolyte fuel cell membranes [102]. The authors in [103] reported the actuation capabilities of IPMCs while the authors in [104] showed that the IPMCs could be used as vibration sensors/dampers. Since then, several researchers have worked towards improving the actuation and sensing capabilities of IPMCs.

IPMC is an electroactive polymer (EAP) that shows a relatively large deformation in response to an electrical activation. EAPs are materials that show change in shape and size under an electrical stimulation [102]. EAPs are divided into two categories: electronic and ionic. Electronic EAP materials are driven by an external electric field or Coulomb forces. They require a high voltage (>100 V) and exhibit large forces. They include piezoelectric, electrostrictive and ferroelectric polymer materials. Dielectric polymers also fall under this category [102]. Ionic EAP materials work on the basis of ion/molecule migration in the polymer in response to an external electric field. They require a low voltage (<5 V) and show lower actuation force compared to electronic EAP materials. They include ionic polymer gels, IPMCs, conductive polymers, carbon nanotubes and electrorheological fluids [102].

3.3.2 Actuation Mechanism of IPMC

IPMC consists of a thin strip of perfluorinated ionomer (Nafion^{TM} or Flemion^{TM}) plated with a noble metal such as gold or platinum on both sides. When an electric field is applied across the metal plates, the IPMC bends towards the anode due to the molecular transportation from the movement of cations and water molecules coupled to the cations as shown in Figure 3.5 [105] [106]. Thus, the actuation of an IPMC is caused due to the imbalance of water density in the IPMC.

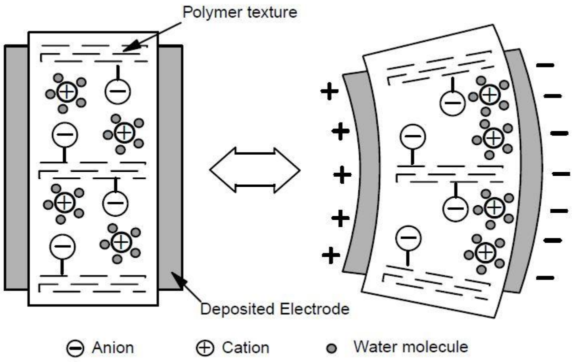

Figure 3.5: Actuation Mechanism of IPMCs [105] (Copyright © 2003, Elsevier)

3.3.3 Characteristics of IPMC

The actuation characteristics of IPMC are influenced by various factors such as the magnitude of voltage, its frequency, its waveform and film shape and size. When a direct voltage is applied across the thickness of an IPMC film, it bends towards the anode. The amount of displacement is directly proportional to the input voltage. An IPMC film creates vibratory motion when an alternating voltage is applied [107]. In the case of an alternating voltage, the displacement is directly proportional to the input voltage and inversely proportional to the frequency of the input voltage [107]. The authors in [105] reported the effect of waveforms and frequencies of the input voltage on the actuation characteristics as shown in Figures 3.6, 3.7 and 3.8.

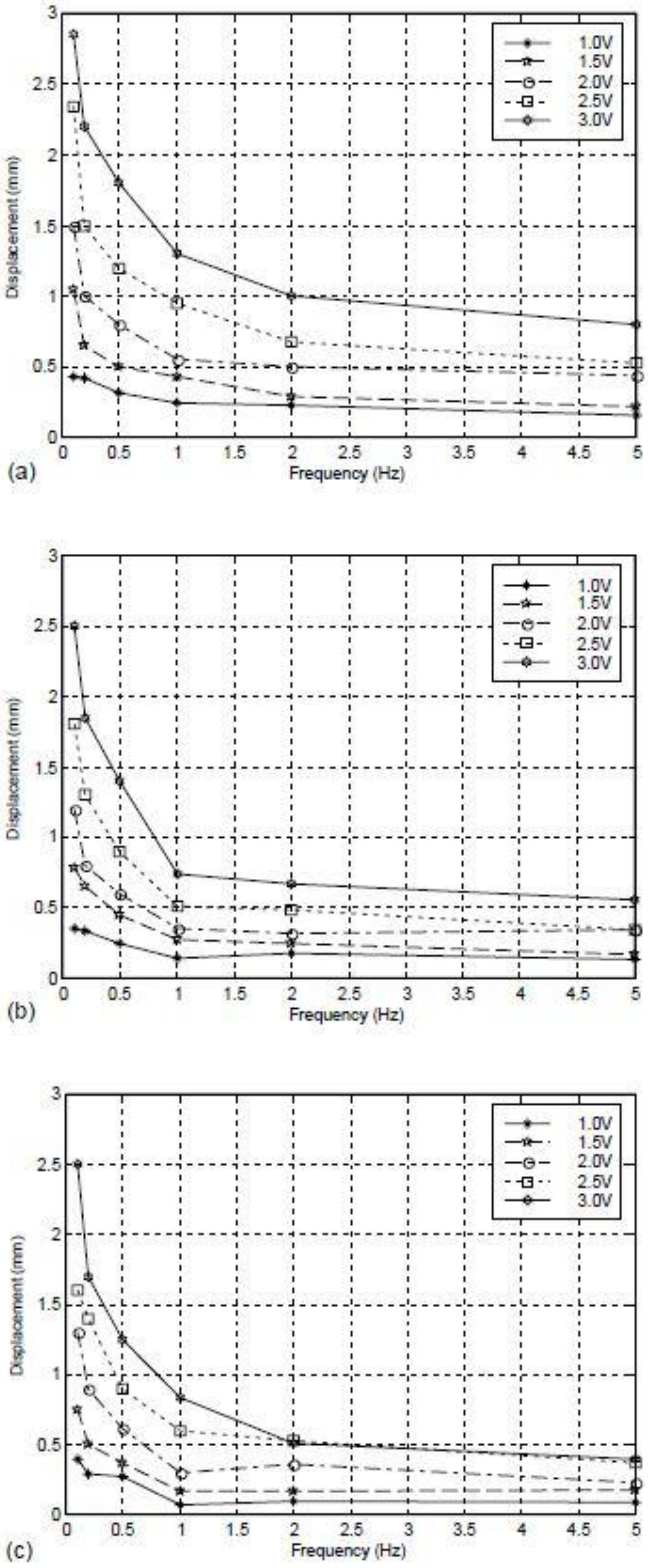

Figure 3.6: Response of IPMC under various waveforms. (a) square wave; (b) sinusoidal wave; (c) triangular wave [105] (Copyright © 2003, Elsevier)

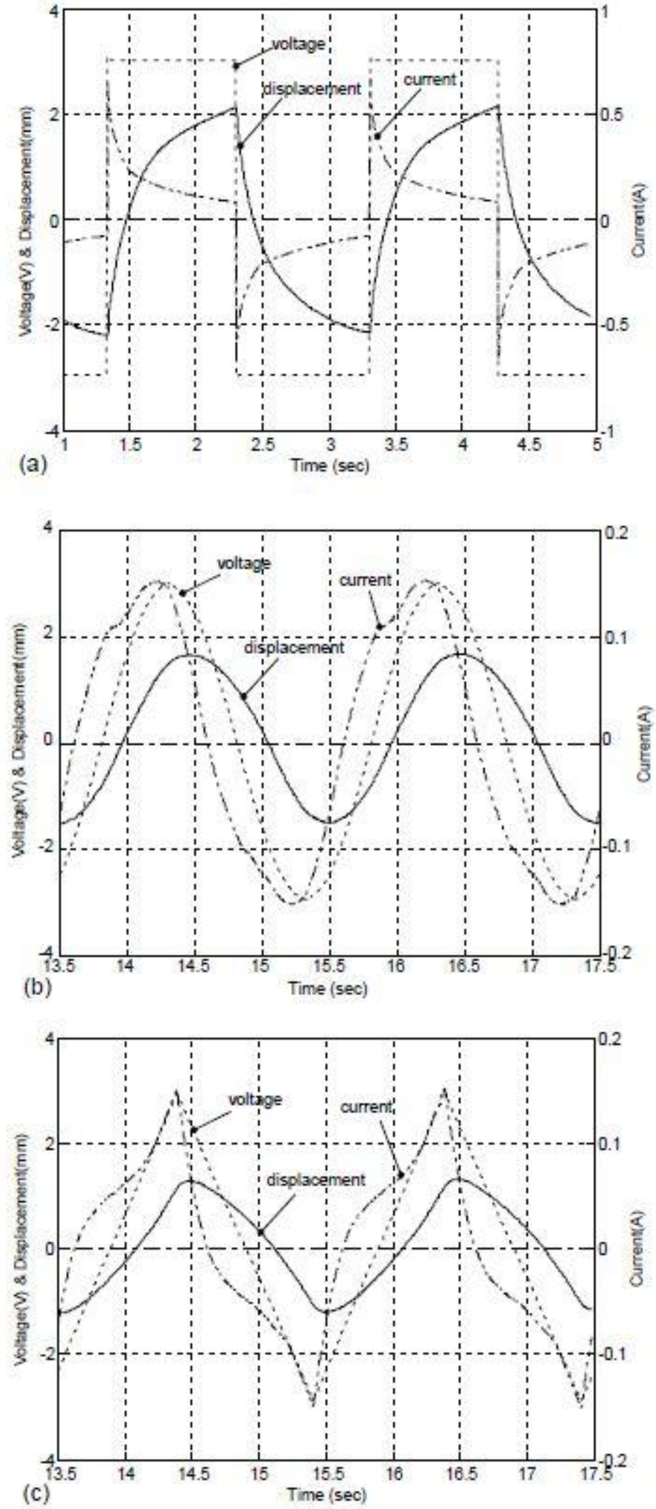

Figure 3.7: Displacement generated and current consumed by IPMC under various waveforms. (a) square wave; (b) sinusoidal wave; (c) triangular wave [105] (Copyright © 2003, Elsevier)

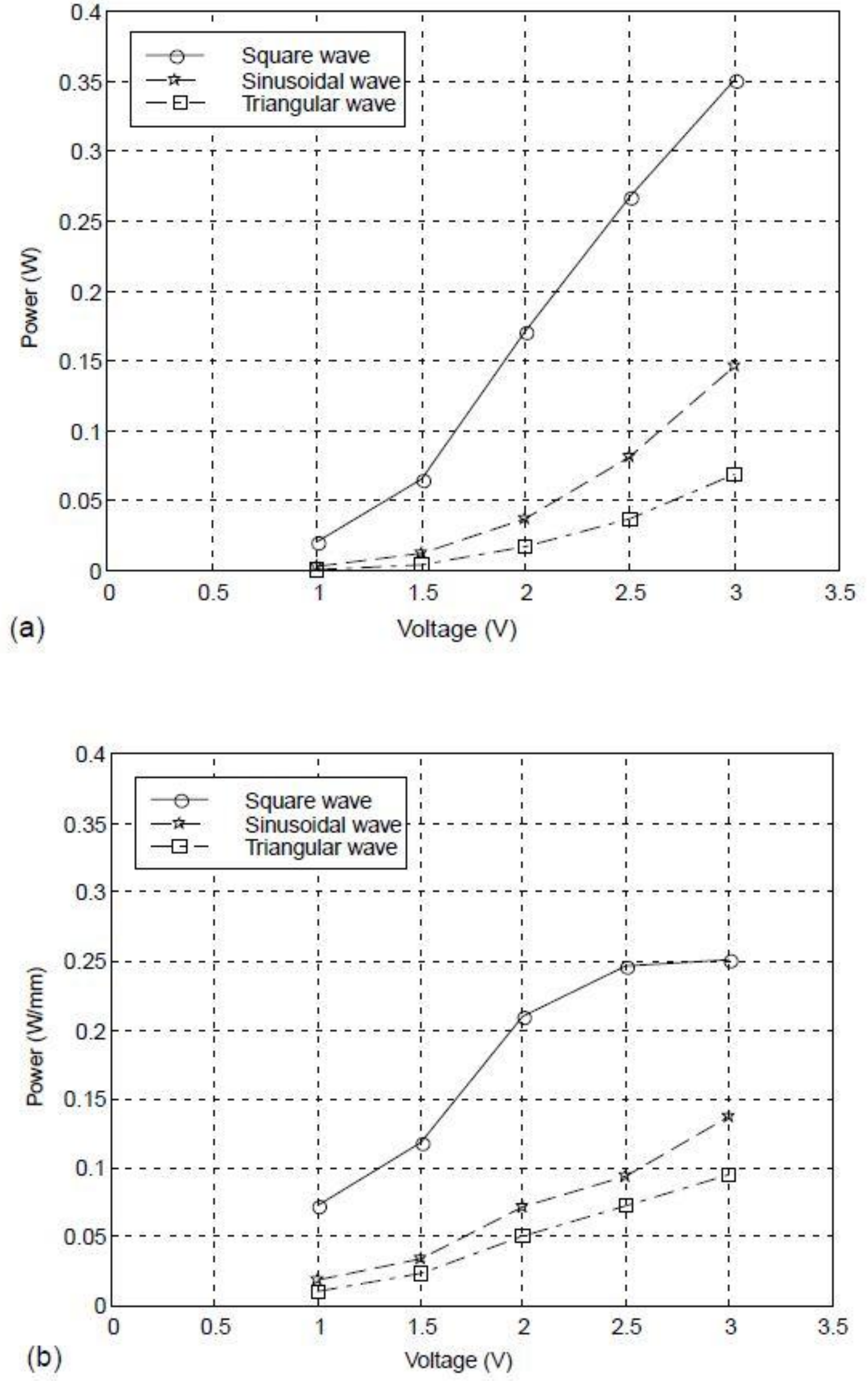

Figure 3.8: Power consumption by IPMC. (a) power consumption per cycle of waveform; (b) power consumption per unit displacement [105] (Copyright © 2003, Elsevier)

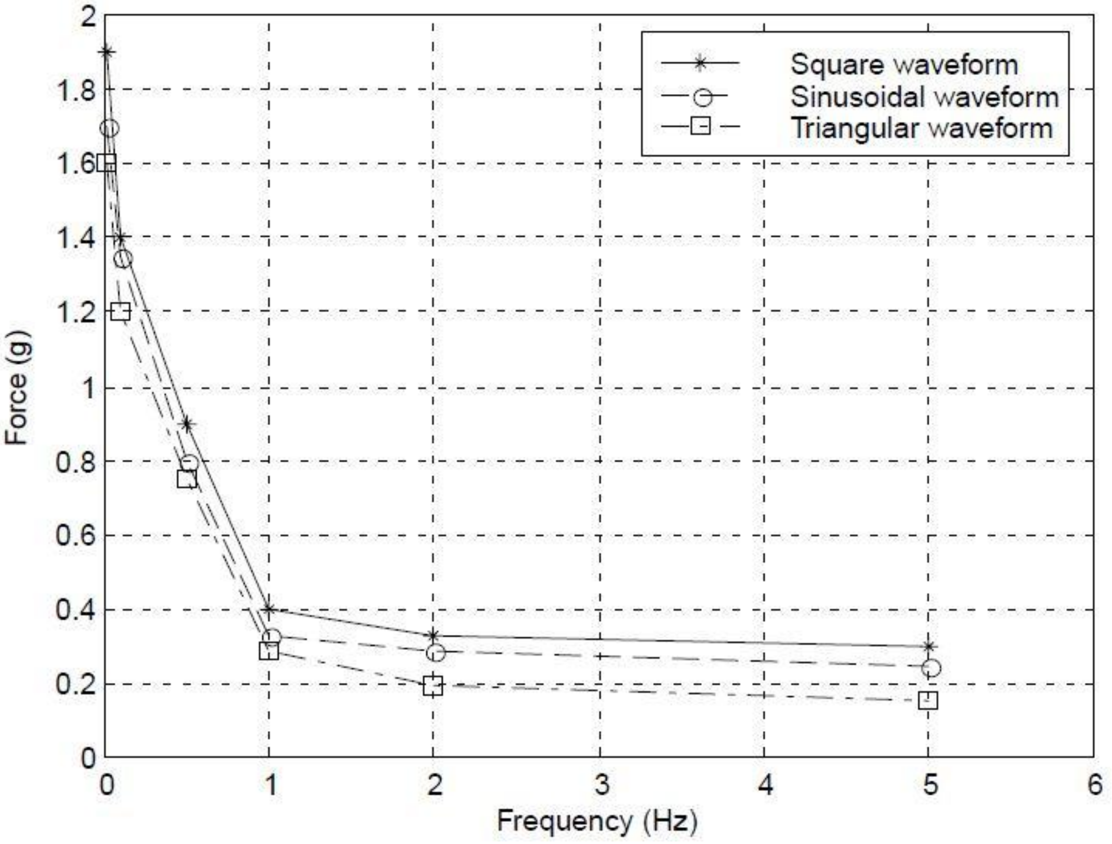

Figure 3.9: Force generated by IPMC under various waveforms [105] (Copyright © 2003, Elsevier)

Figures 3.6, 3.7, 3.8 and 3.9 [105] show the actuation characteristics of an IPMC strip of dimensions 20 mm (L) x 5 mm (W) under three waveforms- square, sinusoidal and triangular. It can be seen from Figure 3.6 that the displacement is higher for higher input voltages. As the frequency of the input signal increases, the amount of displacement decreases. Figure 3.6 also shows that the amount of displacement generated by the square input is slightly more than that generated by the sinusoidal or triangular inputs, but the difference is not significant [105]. Figure 3.7 shows that there is no apparent relationship between the displacement and the square input voltage. On the other hand, there exists a linear relationship between displacement and sinusoidal input voltage and a pseudo linear relationship between displacement and triangular input voltage. Figure 3.8 shows that the power consumed is highest for square wave inputs and lowest for triangular input. Figure 3.9 shows that force generated by the IPMC actuator is almost the same as for each waveform. It also shows that the force is inversely proportional to the frequency of the input voltage: higher the frequency, lower the force. The actuation characteristics also depend on the dimensions of the IPMC film. It is intuitive that a longer IPMC film produces larger displacements. The thickness of the IPMC film also plays an important role. A thicker film produces higher actuation force but lower displacement compared to a thinner film.

3.4 IPMC-based Actuator for AID

Considering the actuation requirements, a donut shaped actuator was designed with an outer diameter of 15 mm, an inner diameter of 5 mm and a thickness of 1 mm. The IPMC actuator has been manufactured by Environmental Robotics Inc (ERI)[3]. Figure 3.10 shows the donut shaped actuator. It can be seen in Figure 3.10 that the shape of the IPMC actuator is irregular - the outer circumference of the actuator is not concentric with the inner circumference of the actuator. The irregularity in the shape deteriorates the amount of displacement by the IPMC and decreases the accuracy of motion.

Figure 3.10: Donut-shaped IPMC actuator compared to a Canadian quarter

3.5 Controller for IPMC Actuator

The aim of this section is to develop a controller for the IPMC actuator which calculates the amount of voltage (${}^{C}V$) necessary to drive the actuator to deflect the needle tip. In

---

[3] Environmental Robots Inc (ERI) is one of the few companies that manufacture custom IPMCs. ERI was the only company that we were able to obtain IPMC actuator in the required shape for our application. However, there were irregularities in the shape of the IPMC actuator fabricated by ERI.

the previous chapter, the control input (${}^{C}P$) for the controller is formed using the position of the needle tip due to tremor (${}^{S}P_{tremor}$) and is governed by the following equation:

$$ {}^{C}P = -({}^{S}P_{tremor}) \tag{3.1} $$

As presented in Chapter 2, the position of the needle tip (${}^{S}P_{tremor}$) is sinusoidal, thus, the control input (${}^{C}P$) is also sinusoidal. From the previous section, we have seen that the displacement is almost linear to the voltage input if the input is sinusoidal. Therefore, an open-loop controller has been designed for the AID as shown in Figure 3.11.

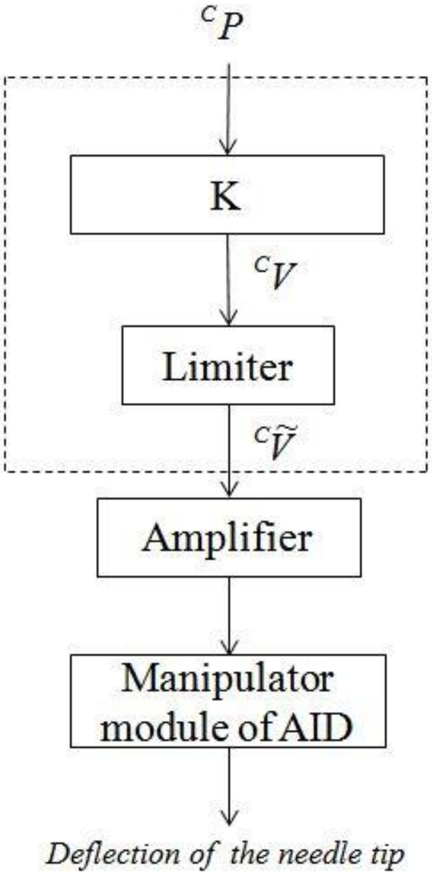

Figure 3.11: Open-loop controller for AID

Since there exists a linear relationship between the desired trajectory and the input voltage in the case of sinusoidal input as presented in the previous section, the following conversion of the displacement to voltage can be used:

$$ {}^{C}V_{k} = K\,{}^{C}P_{k} \tag{3.2} $$

The control input (${}^{C}P$) is converted to voltage (${}^{C}V$) by multiplying it with a transformation factor (*K*). The limiter block shown in Figure 3.11 limits the voltage to ±3.6 V. This is added as a safety feature for the IPMC actuator because Environmental Robots Inc. specified the maximum input voltage as ±3.75 V. The output of the limiter is sent to an amplifier, UPMC 2405 (Quanser Consulting). The gain by the amplifier is set to 1. The output of the amplifier is sent to the IPMC based manipulator module which deflects the tip of the needle. The design of the manipulator module is presented in Chapter 4. The value of *K* is 85715 and is obtained by applying sinusoidal voltage input to the IPMC based manipulator module with different frequencies and amplitudes and observing the displacement of the needle-tip.

The advantage of the open controller is its simplicity in the implementation. However, the limiting factor is its inaccuracy of motion tracking under the action of disturbances such as higher forces at the needle-tip. The performance of the AID with the proposed controller is tested for compensating vibratory motions. The results are presented in Chapter 5.

Chapter 4

4 Accuracy Improvement Device: System Integration

This chapter describes the complete system of the AID. Section 4.1 presents the design of the AID instrument followed by a description of the system hardware and software in Section 4.2.

4.1 AID: Hand-held Instrument

Figure 4.1 shows the prototype of the AID. It weighs 23.56 gm and is 192 mm long (including the needle). The AID can be divided into three parts: sensor module, manipulator module and body. The following sections describe these three parts in detail.

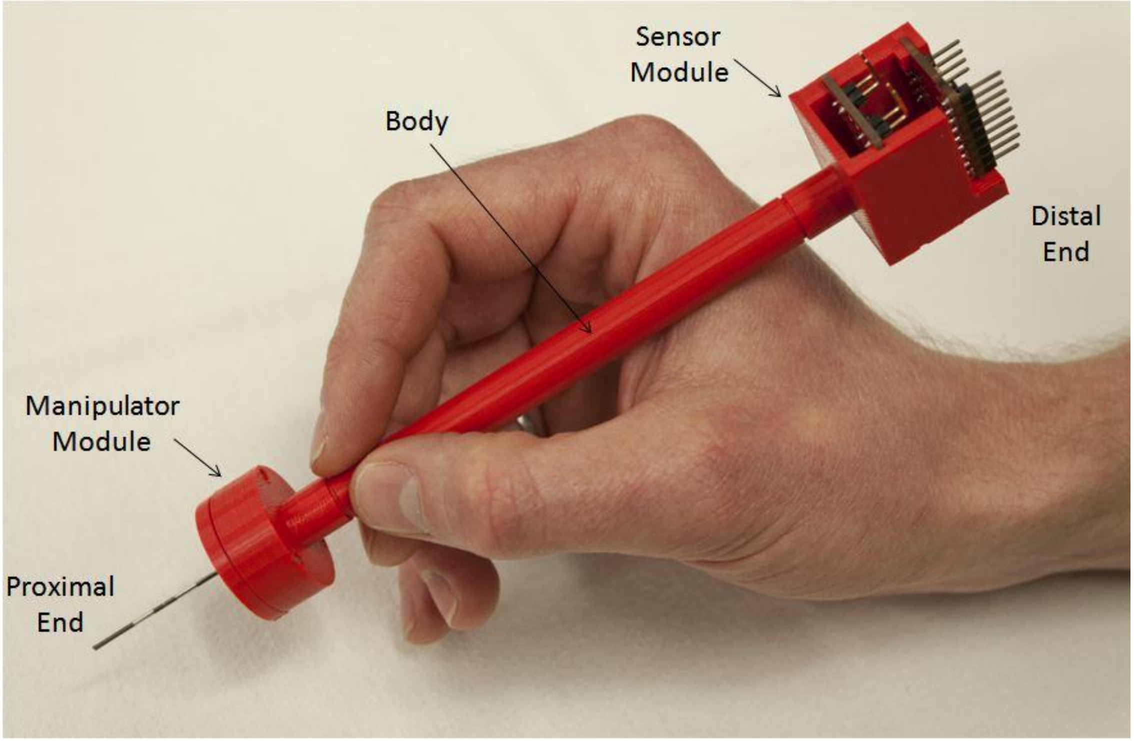

Figure 4.1: Accuracy Improvement Device (AID). The user holds the device using the body to which the sensor module and the manipulator module are attached. The sensor module, located at the distal end, contains the inertial sensors that sense the motion of the device in 6 DOF. The manipulator module, located at the proximal end, deflects the needle tip to compensate for the physiological tremor

4.1.1 Body

The body of the AID, shown in Figure 4.2, is where the user holds the device. It is a shaft and is made hollow so that the wires from the manipulator module can reach the distal end of the device. It is 122 mm long with an inner diameter of 6 mm and an outer diameter of 10 mm. The body is made of ABS thermoplastic and is fabricated using the rapid prototyping system, Dimension Elite 3D Printer (Stratasys).

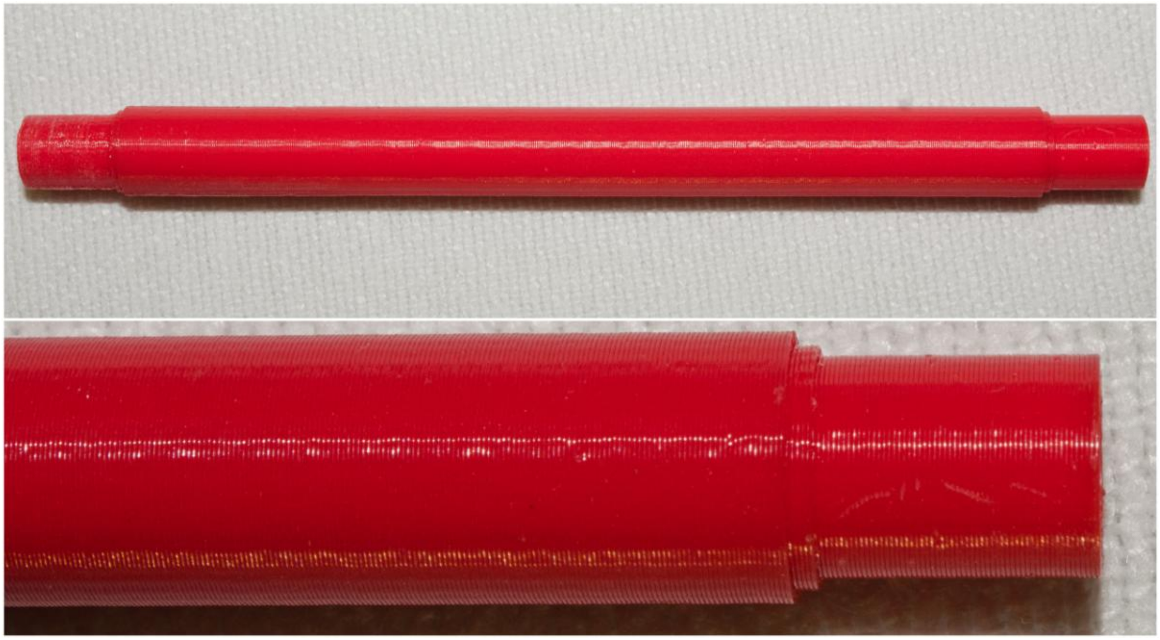

Figure 4.2: (Top) Body of the AID; (Bottom) The reduction of the diameter across the ends of the body. The outer surface of the ends mates with the inner surface of the shafts of the sensor module and the manipulator module.

4.1.2 Sensor Module

The sensor module of the AID, shown in Figure 4.3, contains the inertial sensors that sense the motion of the device in 6 DOF. It has two slots and a hollow shaft and is located at the distal end of the device. It measures 25 mm x 28 mm x 23.6 mm (without the shaft). The upper slot (near the distal-most end of the device) is used for fixing the 5-DOF IMU board that consists of a triple-axis accelerometer (ADXL 335) and a dual-axis gyroscope (IDG 500) and the lower slot is used for fixing the board containing the single-axis gyroscope (MLX 90609).

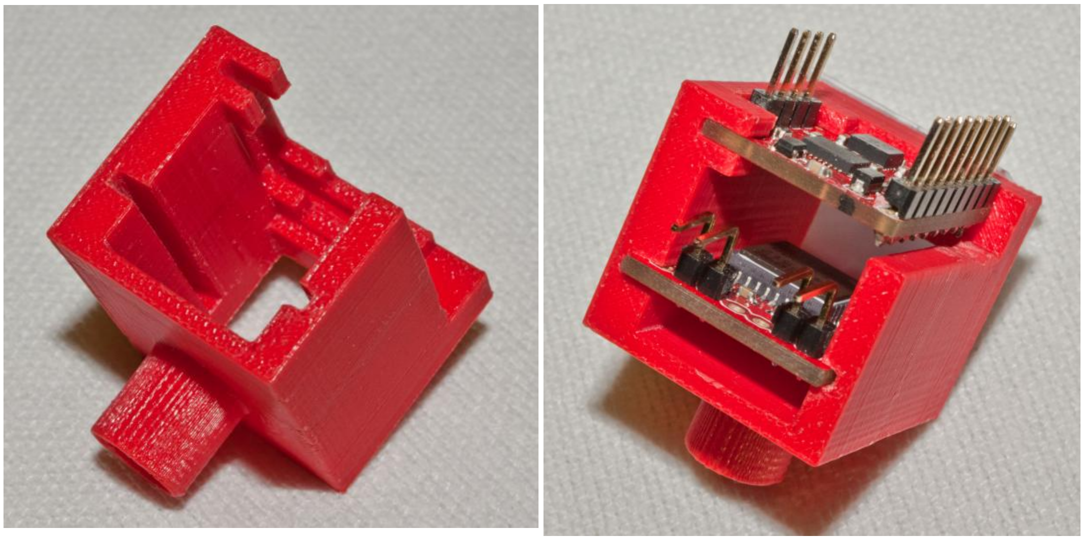

Figure 4.3: (Left) The sensor module of the AID showing the slots for the sensors and the shaft; (Right) The sensor module of the AID with the sensor boards fixed in the slots.

The shaft is 10 mm long with an outer diameter of 10 mm and inner diameter of 8.1 mm. It is hollow so that the wires from the manipulator module can reach the distal end through the body. The inner surface of the shaft mates with the outer surface of one end of the body and fixes the sensor module to the body as shown in Figure 4.1. The sensor module is designed such that the longitudinal axis of the shaft (or of the body) coincides with the center of the triple-axis accelerometer (ADXL 335).

4.1.3 Manipulator Module

The manipulator module of the AID, shown in Figure 4.4, is an IPMC based manipulator which deflects the tip of the needle to compensate for the physiological tremor. In the current implementation of the device, the manipulator module is designed to deflect the needle tip in 1 DOF only. The manipulator module has a diameter of 27 mm and a thickness of 13.3 mm (without the shaft and the needle). The manipulator module can be divided into three parts: needle holder, actuator and actuator holder. The manipulator module incorporates a donut-shaped IPMC actuator having an inner diameter of 5 mm, an outer diameter of 15 mm and a thickness of 1 mm as shown in Figure 4.5.

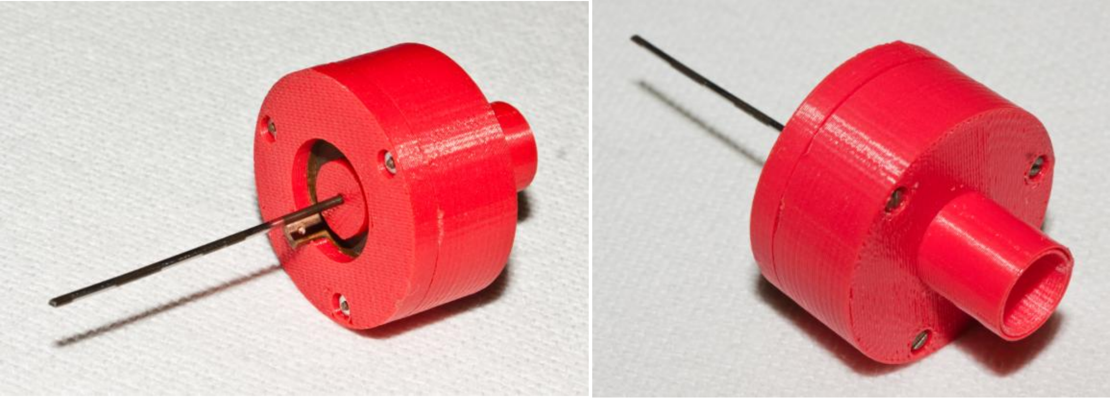

Figure 4.4: Manipulator Module of the AID

Figure 4.5: Donut shaped IPMC actuator compared to a Canadian quarter

Figure 4.6 shows the CAD rendering of the needle holder (shown in grey) attached on the IPMC actuator (shown in gold). The IPMC actuator is squeezed between two ring-shaped copper electrodes (shown in dark brown) which provide the necessary voltage to drive the actuator. Figure 4.6 shows the location of the needle holder and the electrodes with respect to the IPMC actuator in the manipulator module. The electrodes are attached to the actuator holder (not shown in Figure 4.6).

Figure 4.7 shows the components of the needle holder. The part at the bottom of Figure 4.7 has a hole to which the needle is attached as shown in Figure 4.8.

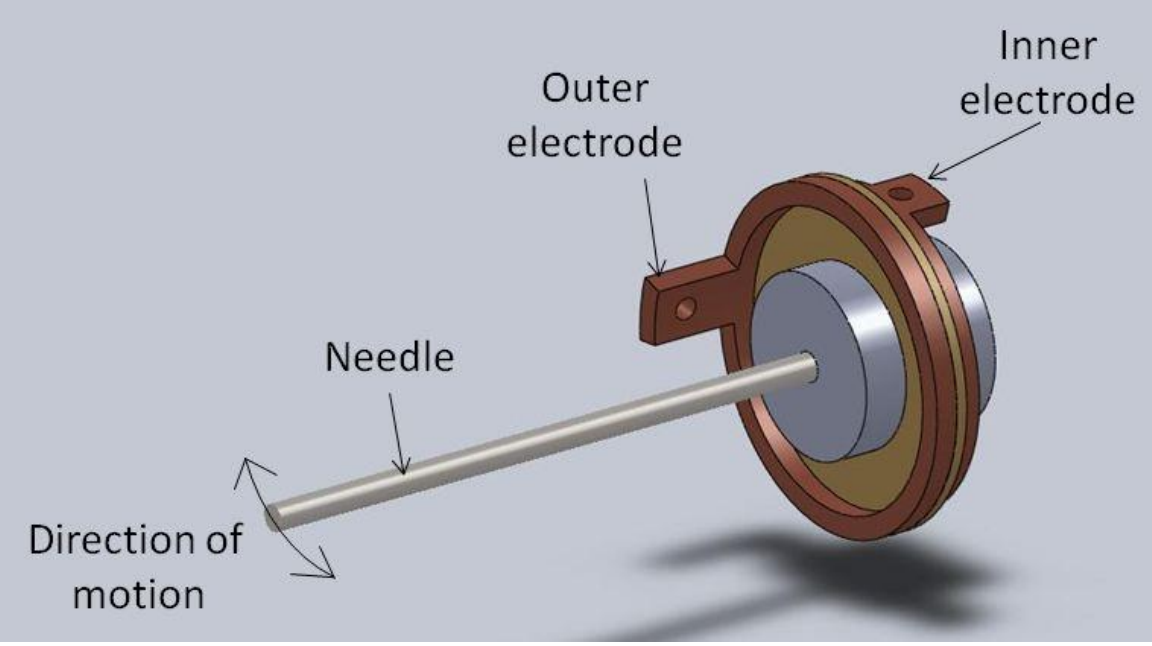

Figure 4.6: CAD rendering of the needle holder attached on the IPMC actuator. The needle is shown in silver. The parts in grey are the needle holder. The IPMC actuator is shown in gold. The ring-shaped electrodes are shown in dark brown. The one close to the needle tip is the outer electrode and the one away from the needle tip is the inner electrode. The direction of motion of the needle is also shown.

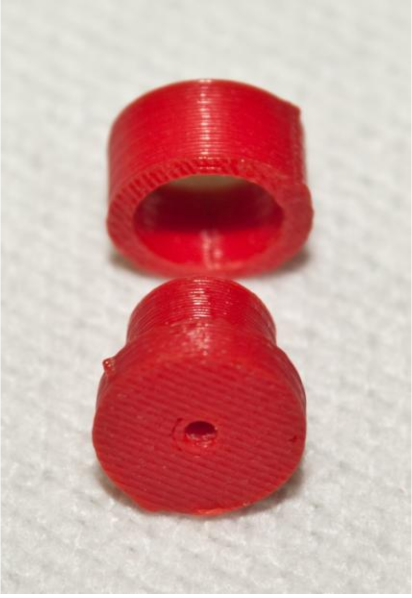

Figure 4.7: Components of the needle holder

The needle holder is attached to the IPMC actuator as shown in Figure 4.9.

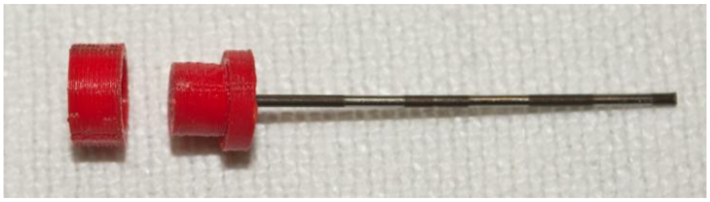

Figure 4.8: Needle holder with the needle

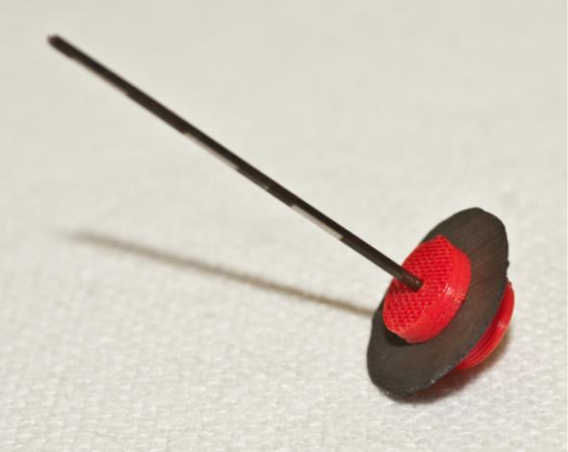

Figure 4.9: Needle holder attached on the IPMC actuator

The IPMC actuator is driven using two ring-shaped electrodes as shown in Figure 4.6. Figure 4.10 shows the inner and the outer electrode. The thickness of both the electrodes is 1 mm.

Figure 4.10: Electrodes that drive the IPMC actuator. (Left) Inner electrode (away from the needle tip); (Right) Outer electrode (near the needle tip)

The inner electrode has an outer diameter of 14 mm and an inner diameter of 12 mm. The outer electrode has an outer diameter of 15 mm and an inner diameter of 13 mm. An extension with a hole of diameter 1mm is provided to attach wires to the electrodes. The inner electrode is attached to the inner actuator holder and the outer electrode to the outer actuator holder as shown in Figure 4.11.

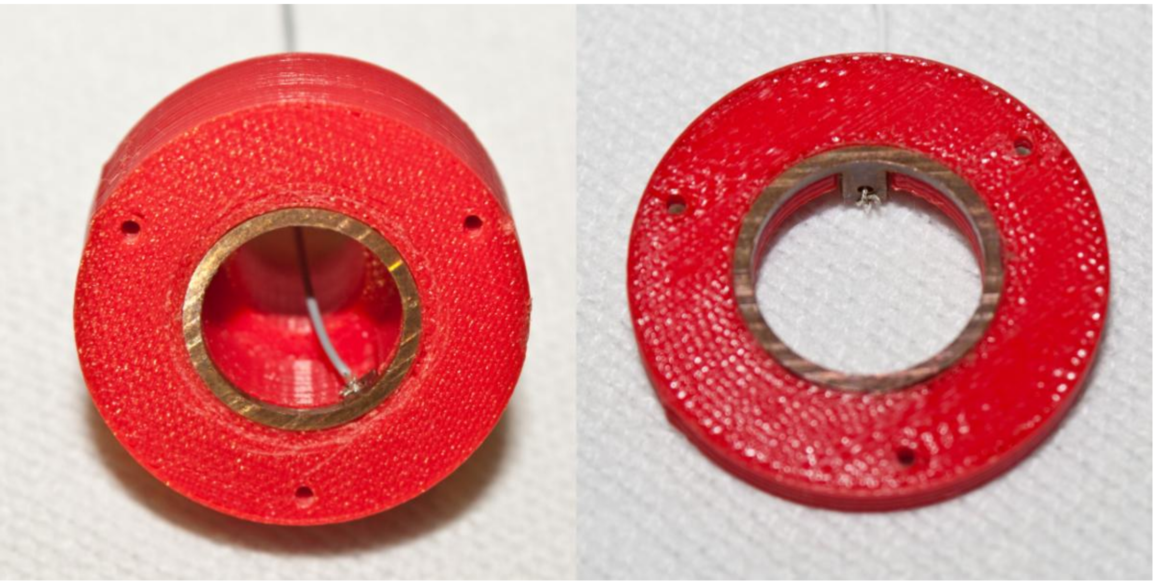

Figure 4.11: Actuator holder with electrodes. (Left) Inner actuator holder; (Right) Outer actuator electrode

The inner actuator holder, shown in Figure 4.12, has an outer diameter of 27 mm, an inner diameter of 12 mm and is 10 mm thick. It also contains the shaft that attaches the manipulator module with the proximal end of the body. The shaft is 10 mm long with an outer diameter of 10 mm and inner diameter of 8.1 mm. A slot of 1 mm thickness and 14 mm diameter at the front face of the inner actuator holder is incorporated so that the inner electrode can be attached.

The outer actuator holder, shown in Figure 4.13, has an outer diameter of 27 mm, an inner diameter of 13 mm and a thickness of 3 mm. It contains a slot of 1 mm thickness and 15 mm diameter which is used to attach the outer electrode.

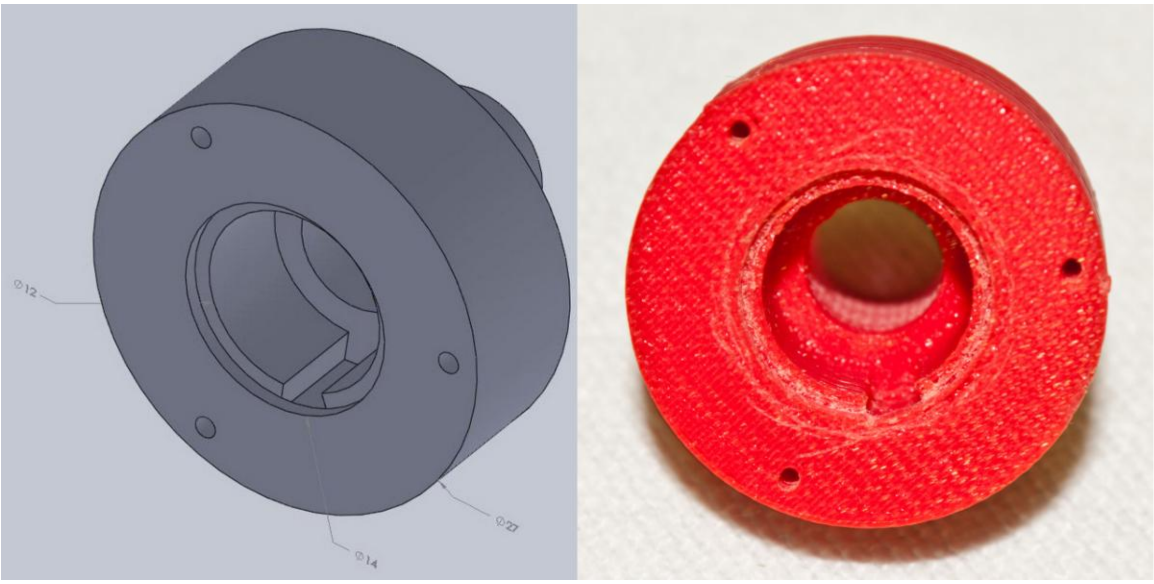

Figure 4.12: Inner actuator holder. (Left) CAD Rendering; (Right) Fabricated part

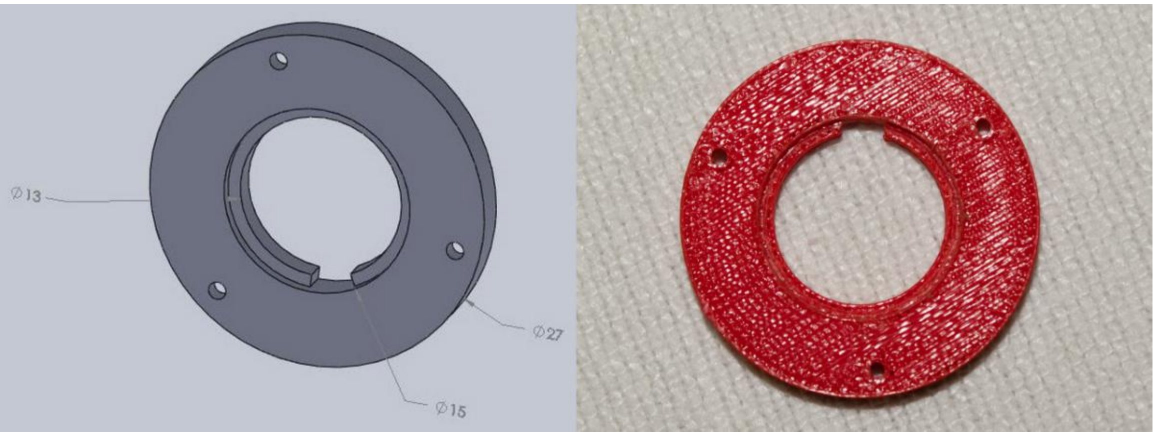

Figure 4.13: Outer actuator holder. (Left) CAD Rendering; (Right) Fabricated part

The needle holder is attached on the IPMC as shown in Figure 4.9. The electrodes are attached to the actuator holders as shown in Figure 4.11. The IPMC with the needle holder is placed between the inner actuator holder and the outer actuator holder. The two actuator holders are fixed together using three M1 fasteners to assemble the manipulator module as shown in Figure 4.4. The manipulator module is attached to one end of the body using the shaft in the inner actuator holder. The sensor module is attached to the other end of the body to completely assemble the AID.

One of the advantages of the AID is that the length and diameter of the gripping can be changed to enhance the comfort in using the device by changing the dimensions of the body since it does not contain any actuator or sensors.

4.2 The AID: System Hardware and Software

Figure 4.14 shows the overview of the complete system of the AID. The blocks inside the dashed lines in Figure 4.14 are executed in the host computer.

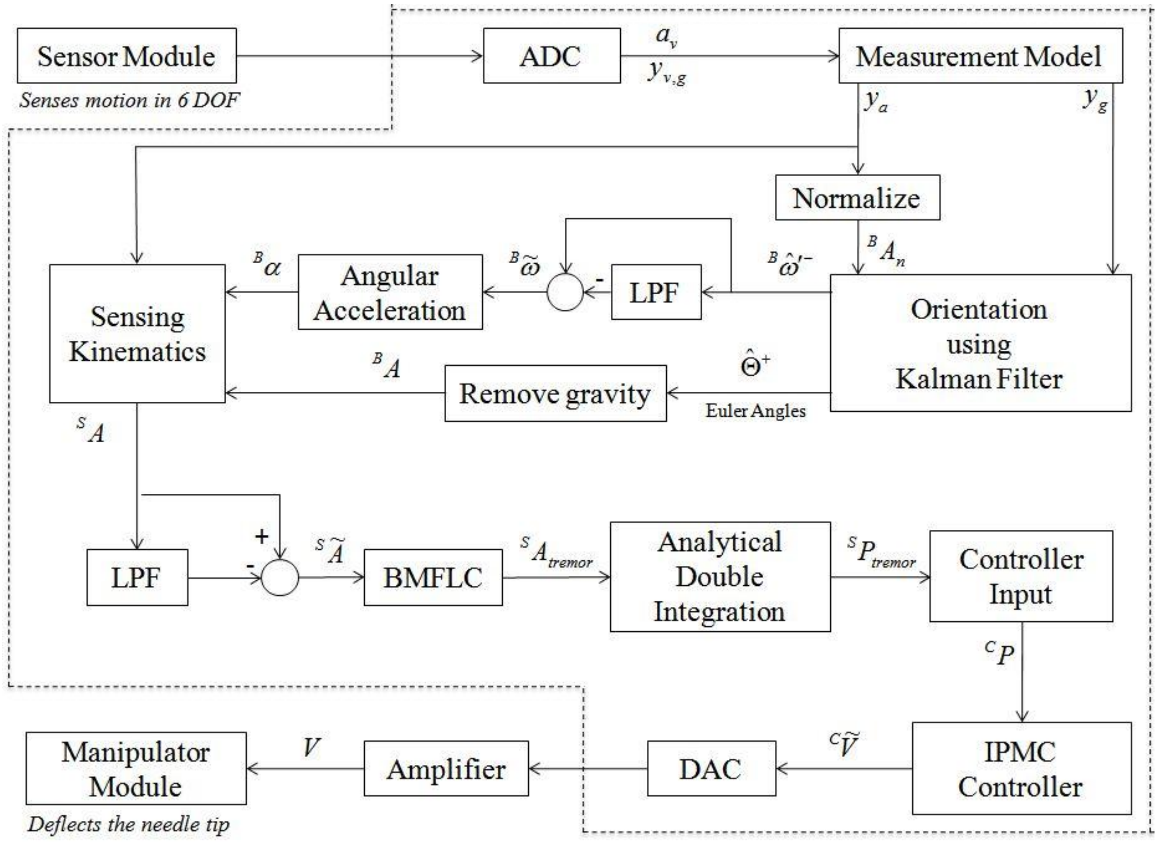

Figure 4.14: Overview of the complete system of the AID

The host computer is a Pentium 4 2.8 GHz 3 GB RAM desktop computer with Windows XP Professional as the operating system. ADC and DAC in Figure 4.14 stand for analog-to-digital converter and digital-to-analog converter respectively. The converter is a Sensoray 626 (Sensoray, Co. Inc.) data acquisition board. Sensoray 626 is a PCI bus card with 16 16-bit differential analog input channels and 4 14-bit analog output channels. The software is programmed using Simulink and Matlab on the host computer. A real-time hardware-in-the-loop environment is created using QuaRC (Quanser) [108].

The 6 DOF motion of the device is sensed by the sensor module as described in Chapter 2. The voltage output of the sensors is sent to the host computer via the ADC. This contains 3-DOF accelerometer readings (a_v) and 3-DOF gyroscope readings ($y_{v,g}$) which are sent to the measurement model (described in Appendix A) where the accelerometer readings are converted to units of m/sec^2 and the gyroscope readings are converted to units of rad/sec and are stored in y_a and y_g respectively. The acceleration (y_a) is then normalized as described in Appendix A. The normalized acceleration (${}^{B}A_n$) and the angular velocity (y_g) are fused together to calculate the Euler angles (Θ) using the augmented state complementary Kalman filter as described in Section 2.4, Chapter 2. The effective body acceleration (${}^{B}A$) is calculated by removing the gravity factor from the acceleration sensed by the accelerometer using the orientation provided by the augmented state complementary Kalman filter. The Kalman filter also provides un-biased angular velocity (${}^{B}\hat{\omega}'$). The low frequency voluntary motions and the residual bias is removed from ${}^{B}\hat{\omega}'$ using the low pass filtering technique presented in Chapter 2. The angular acceleration (${}^{B}\alpha$) is calculated from angular velocity (${}^{B}\tilde{\omega}$) that only contains angular velocity due to tremor, residual low frequency components and the noise. The acceleration of the needle-tip (${}^{S}A$) is calculated by applying the kinematic relationships as described in Section 2.3.1.1, Chapter 2. The low frequency voluntary motions and the residual gravity is removed from ${}^{S}A$ using the low pass filtering technique. The acceleration of the needle tip due to tremor (${}^{S}A_{tremor}$) is estimated using the Band-limited Multiple Fourier Linear Combiner (BMFLC) algorithm as described in Section 2.5. The position of the needle tip due to tremor (${}^{S}P_{tremor}$) is calculated by analytically double integrating the acceleration of the needle tip due to tremor as described in Section 2.5.2. The negative of ${}^{S}P_{tremor}$ forms the control input (${}^{C}P$) and is sent to the IPMC controller. The controller computes the amount of voltage (${}^{C}\tilde{V}$) necessary to actuate the IPMC actuator to deflect the needle tip by ${}^{C}P$. This voltage is sent to an amplifier (UPM 2405-

Quanser) via the DAC (Sensoray 626). The output of the amplifier is sent to the IPMC actuator which drives the manipulator and deflects the needle tip to compensate for the physiological tremor.

Chapter 5

5 Experimental Validation and Results

This chapter presents the experimental set-up for testing the device and its sub-systems followed by a discussion of the results. Section 5.1 describes the experiments conducted to test the proposed augmented state complementary Kalman filter (ACKF) to compute the orientation. Section 5.2 presents the physiological tremor in the hand calculated using the AID. Section 5.3 presents the experimental design to test the AID in compensating vibrations in 1 DOF.

5.1 Kalman Filter

This section presents the experimental design to test the proposed ACKF followed by an analyses of the results.

5.1.1 Experimental Design

The experimental setup consists of a precision motor rotary stage, T-RS60A (Zaber Technologies). Figure 5.1 shows the experimental set-up. The sensor module of the AID (marked as 'S' in Figure 5.1) is fixed on the rotary stage (marked as 'R' in Figure 5.1). The experimental setup allows to change the pitch (θ) by rotating the sensor module about Y_B axis with various angular velocities (${}^{B}\omega_y$).

Four sets of experiments were conducted. The amplitude of rotation (θ_{p-p}) and the angular velocity (${}^{B}\omega_y$) for each set is listed in Table 5.1. The angular velocity of 3 deg/s is chosen for two sets since the maximum angular velocity encountered during hand-held motion was 3.02 deg/s as previously explained in Chapter 2. The angular velocity of 10 deg/s was also chosen for two sets to test the effects of higher angular velocities on the calculation of angles by ACKF. The amplitude of rotation (θ_{p-p}) was also varied to test the effects of the amplitude on ACKF. For each set, the experiment was conducted for 3 min at a sampling frequency of 500 Hz.

Table 5.1: Amplitude and angular velocity for 4 sets

Set	θ_{p-p} (deg)	${}^{B}\omega_{y}$ (deg/s)
1	60	±3
2	60	±10
3	90	±3
4	90	±10

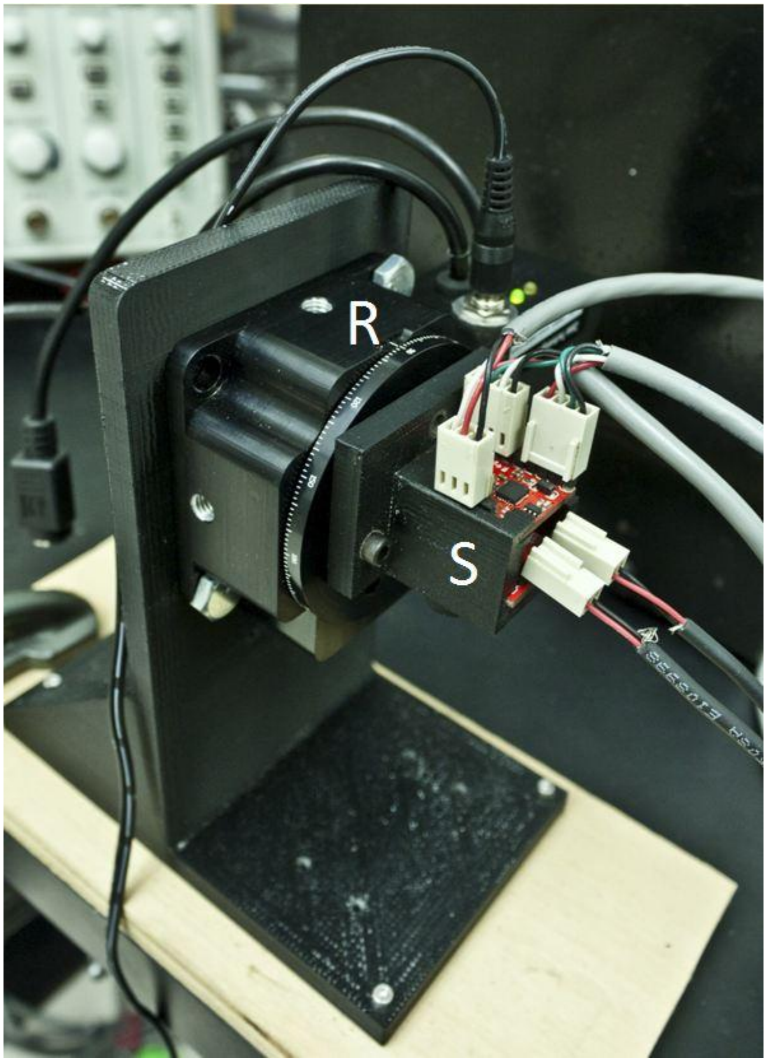

Figure 5.1: Experimental set-up for testing the proposed ACKF. The sensor module, marked as 'S', is mounted on a motor rotary stage, marked as 'R'.

The turning motion was started after 5 seconds during which time the sensor module was left to rest at its original horizontal position ($\theta = \phi = 0$). After reaching the peaks, the module was left idle before turning in the opposite direction. The motion allowed to test for any overshoots in the calculation of the angles by the ACKF. The following quantities were measured in the experiments:

- the roll ($\hat{\phi}^{+}$) and the pitch ($\hat{\theta}^{+}$) using the ACKF
- the roll ($\hat{\phi}_{a}^{-}$) and the pitch ($\hat{\theta}_{a}^{-}$) using the tri-axial accelerometer
- the predicted gyro rate or the angular velocity (${}^{B}\hat{\omega}_{y}^{-}$) using the ACKF
- the predicted gyro rate or the angular velocity (${}^{B}\omega_{y}'$) calculated when the bias is kept constant, i.e., $b_k = b_{k-1}$.

5.1.2 Results and Analyses

Figure 5.2 shows the pitch ($\hat{\theta}^{+}$) and the roll ($\hat{\phi}^{+}$) calculated using the augmented state complementary Kalman filter for set 2. Figure 5.3 shows the pitch ($\hat{\theta}_{a}^{-}$) and the roll ($\hat{\phi}_{a}^{-}$) calculated using the tri-axial accelerometer for set 2.

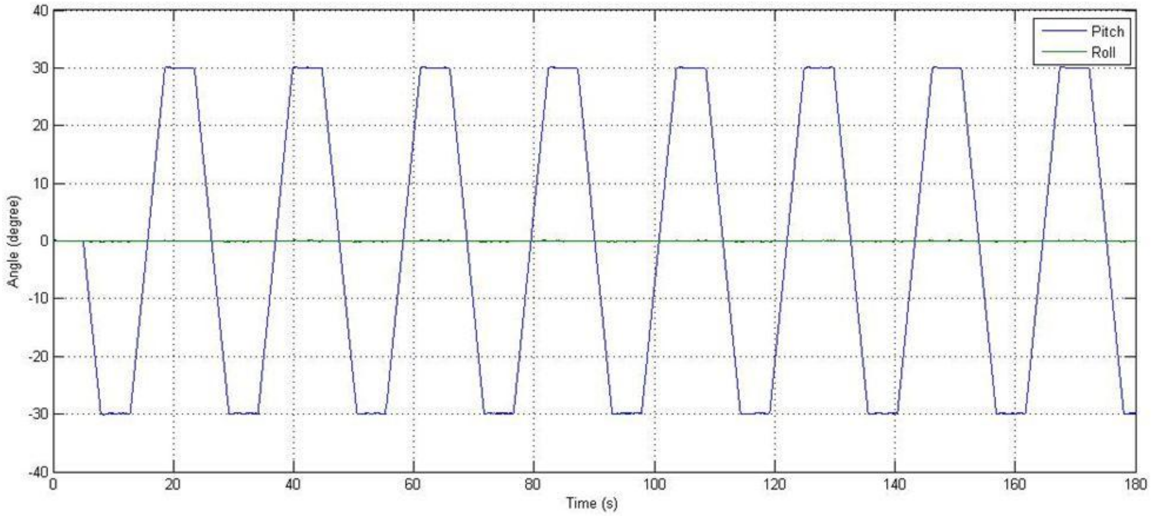

Figure 5.2: Pitch ($\hat{\theta}^{+}$) and roll ($\hat{\phi}^{+}$) using the ACKF for set 2

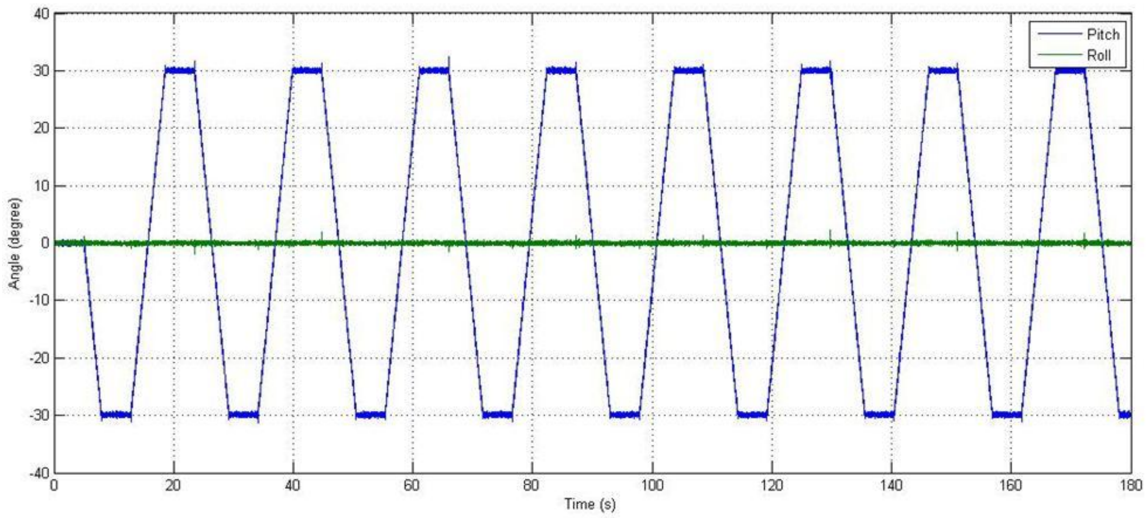

Figure 5.3: Pitch ($\hat{\theta}_a^-$) and roll ($\hat{\phi}_a^-$) using the tri-axial accelerometer for set 2

It is clear from Figure 5.3 that the angles, $\hat{\theta}_a^-$ and $\hat{\phi}_a^-$ are noisy. Overshoots in $\hat{\theta}_a^-$ and $\hat{\phi}_a^-$ can also be seen at the starting of the rotary motion after the resting state at the peaks. As shown in Figure 5.2, the proposed ACKF provides overshoot-free angles ($\hat{\theta}^+$ and $\hat{\phi}^+$) that does not incorporate the noise from the accelerometers or gyroscopes. Similar results were obtained for other sets. Figure 5.4 shows $\hat{\theta}^+$ for a period of 0-2 second.

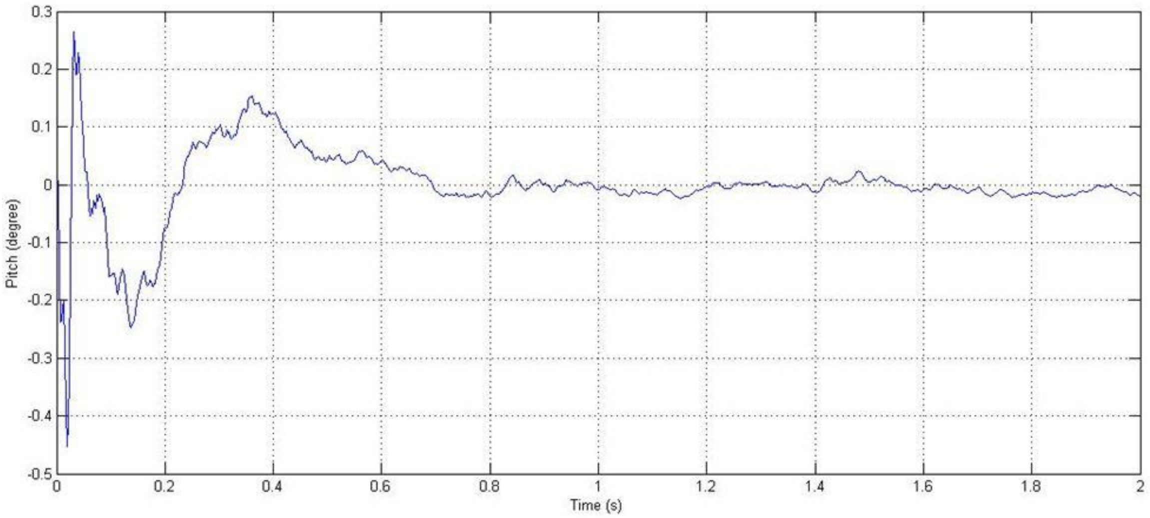

Figure 5.4: Pitch ($\hat{\theta}^+$) using the ACKF for a time period of 0-2 s for set 2

Figure 5.5 shows $\hat{\phi}^{+}$ for a period of 0-1 second. Figure 5.4 and 5.5 shows that $\hat{\theta}^{+}$ converges in 0.8 seconds (or 400 iterations) and $\hat{\phi}^{+}$ converges in 0.5 seconds (or 250 iterations). The settling time for other sets are listed in Table 5.2.

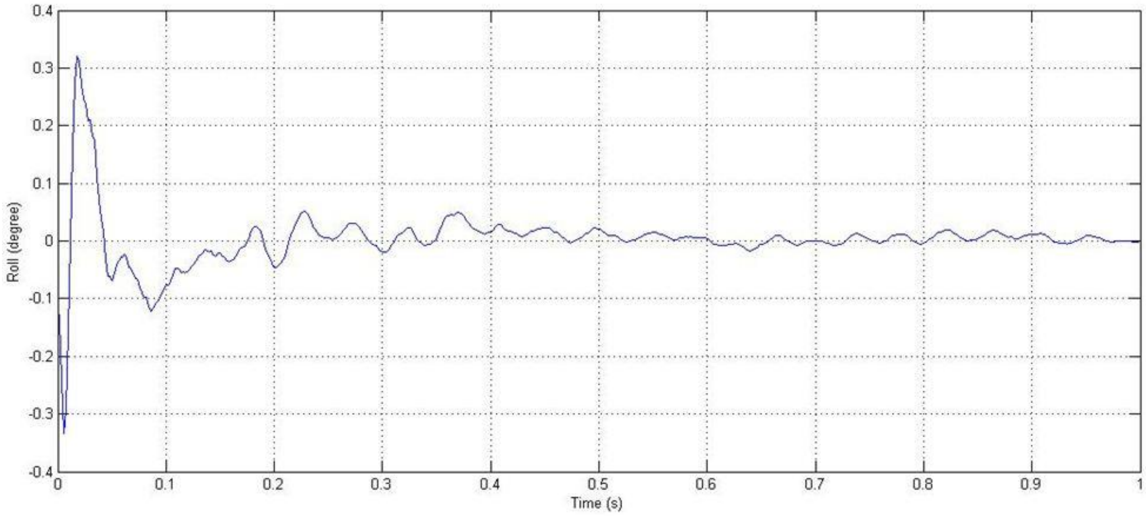

Figure 5.5: Roll ($\hat{\phi}^{+}$) using the ACKF for a time period of 0-1 s for set 2

Figure 5.6 and 5.7 shows the un-biased angular velocity (${}^{B}\hat{\omega}_{y}^{-}$) provided by the ACKF and the angular velocity (${}^{B}\omega_{y}'$) when the bias was kept constant respectively.

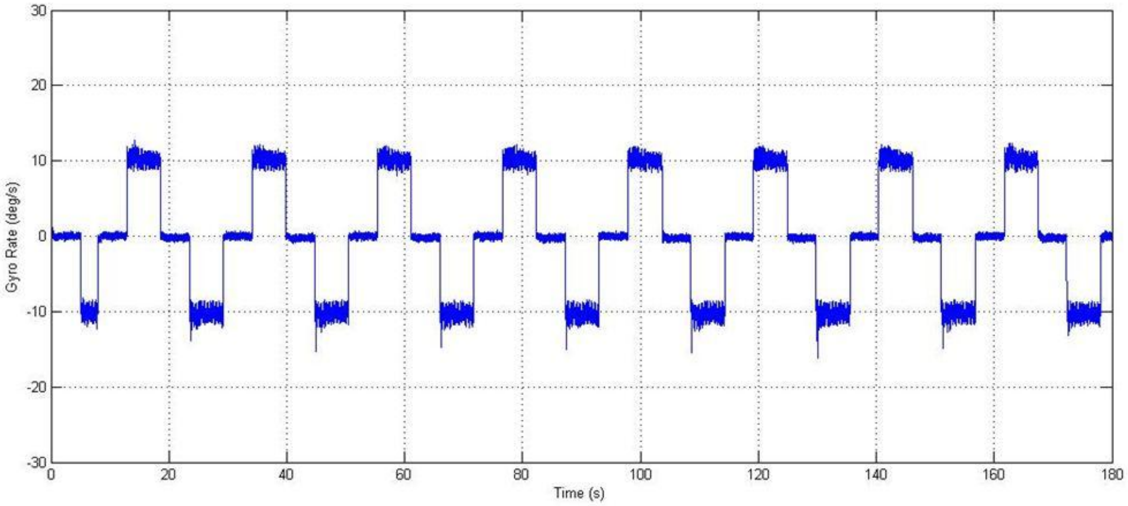

Figure 5.6: Angular velocity (${}^{B}\hat{\omega}_{y}^{-}$) calculated using the ACKF for set 2

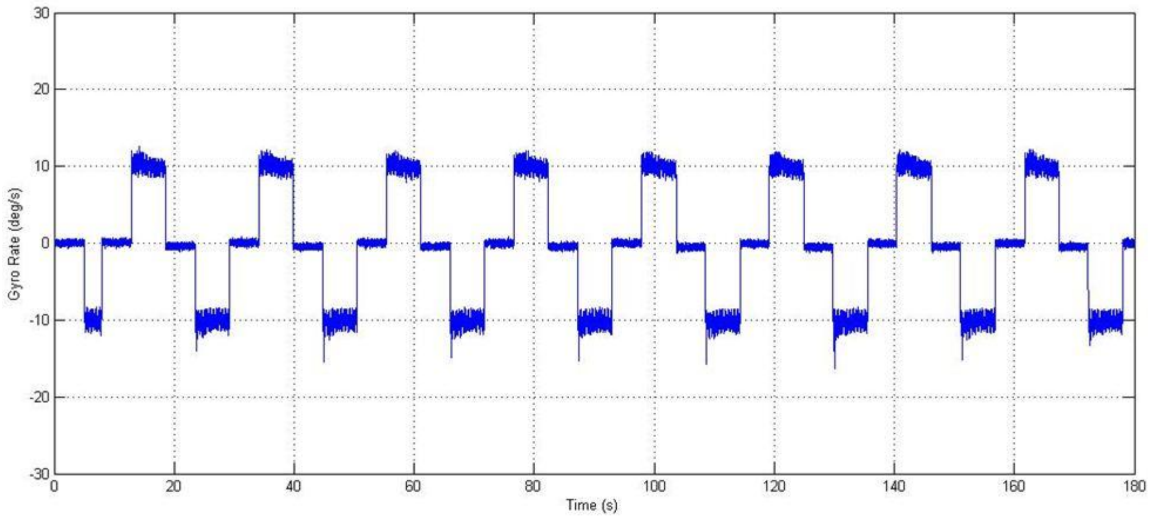

Figure 5.7: Angular velocity (${}^{B}\omega'_{y}$) when the bias was kept constant for set 2

Figure 5.7 shows that ${}^{B}\omega'_{y}$ drifts when the module is in motion and the mean is non-zero during the time instants when the module is idle after completing positive rotations. As shown in Figure 5.6, the ACKF provides a drift-free and corrected angular velocity, ${}^{B}\hat{\omega}_{y}^{-}$. Similar results were obtained for other sets. Figure 5.8 shows ${}^{B}\hat{\omega}_{y}^{-}$ for a time period of 0-1 second. It shows that ${}^{B}\hat{\omega}_{y}^{-}$ converges in approximately 0.4 seconds (or 200 iterations).

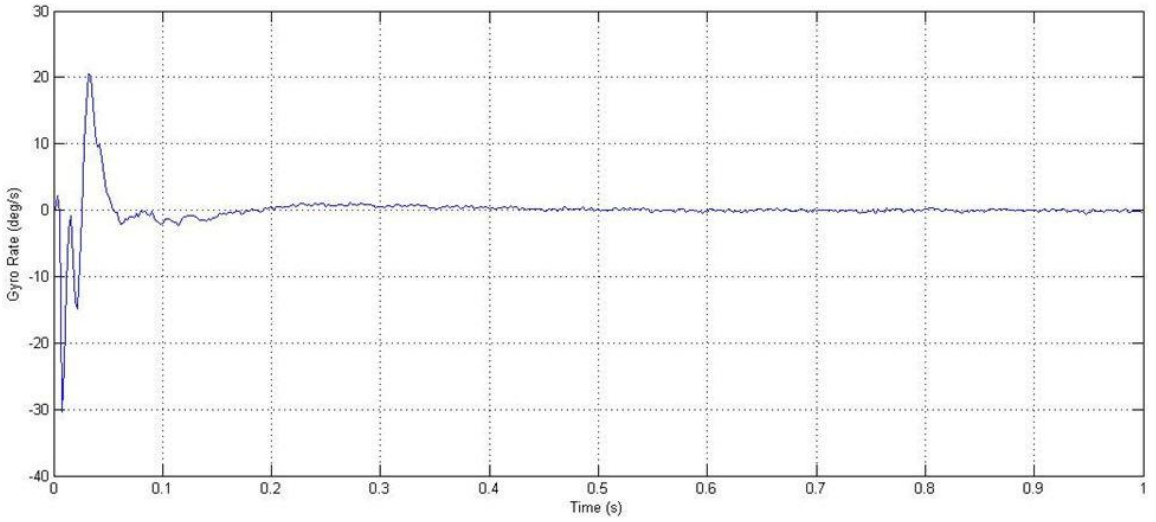

Figure 5.8: Angular velocity using the ACKF for a time period of 0-1 s for set 2

The root mean squared (rms) errors in calculating θ and ϕ and the settling times in θ, ϕ and ${}^{B}\hat{\omega}_y^{-}$ using the ACKF for the four sets are listed in Table 5.2. The rms errors in calculating the angles are always less than 0.1^0. The errors in calculating θ and ϕ are slightly higher for higher amplitudes of rotations as shown in Table 5.2. It is clear from the figures and Table 5.2 that the proposed ACKF quickly converges and provides a reduced noise drift-free calculation of the angles that have high accuracy and are free from overshoots.

Table 5.2: RMS Errors and settling times in calculating θ and ϕ

Set	$\theta_{\varepsilon,rms}$	$\phi_{\varepsilon,rms}$	Settling Time $\hat{\theta}^{+}$	Settling Time $\hat{\phi}^{+}$	Settling Time ${}^{B}\hat{\omega}_y^{-}$
1 (30-3)	0.0539^0	0.0438^0	0.5 s	0.5 s	0.2 s
2 (30-10)	0.0555^0	0.0518^0	0.8 s	0.5 s	0.4 s
3 (45-3)	0.0602^0	0.0953^0	0.6 s	0.5 s	0.3 s
4 (45-10)	0.0669^0	0.0785^0	0.6 s	0.6 s	0.3 s

The error in measuring the angular velocity, when the bias is kept constant, is shown in Figure 5.7. The errors occur due to the bias drift associated with the gyroscopes. This emphasizes on the need for modeling the gyro bias in the Kalman filter for effective calculation of the orientation. The ACKF proposed in Chapter 2 models the gyro bias and provides a drift-free and corrected angular velocity as shown in Figure 5.6.

5.2 Physiological Tremor in Hand

This section presents the experimental design to test the algorithm presented in Chapter 2 in sensing the physiological tremor in the hand followed by analyses of the results.

5.2.1 Experimental Design

In this experiment, the user held the device in his hand with the wrist and the elbow resting on the table as shown in Figure 5.9. The user was asked to keep the device as steady as possible, i.e., not to produce any motion voluntarily. The experiment was carried out for 90 seconds with a sampling frequency of 500 Hz. The tremor in the user's hand was measured in 3 DOF with respect to the body frame $\{B\}$ and the steady frame $\{S\}$ using the algorithm proposed in Chapter 2. Fast Fourier transforms (FFTs) were carried out on the sensed accelerations and the calculated displacements using the BMFLC, with respect to $\{B\}$ and $\{S\}$. The FFTs were obtained to identify the frequency components in the sensed motion, particularly to identity the frequency of the physiological tremor and the amount of attenuation by the BMFLC.

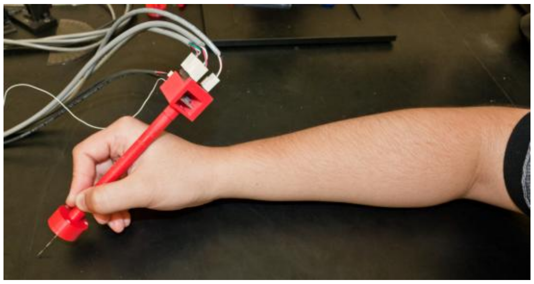

Figure 5.9: User holding the AID

5.2.2 Results and Analyses

Figures 5.10, 5.11 and 5.12 shows the single-sided frequency spectrum of (${}^{B}\tilde{A}$) i.e., the acceleration with respect to $\{B\}$ after filtering out the low frequency (< 4 Hz) components using the low pass filtering technique presented in Chapter 2.

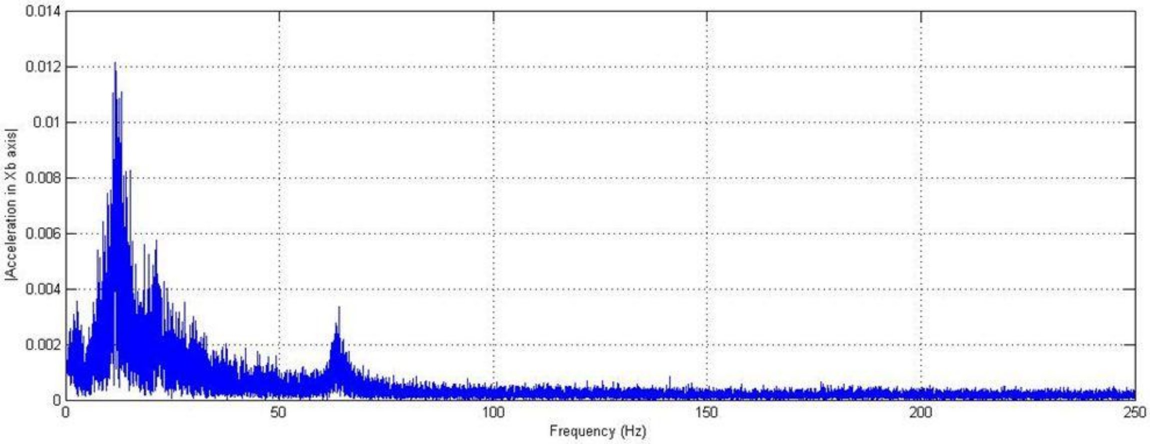

Figure 5.10: Single-sided frequency spectrum of ${}^{B}\tilde{a}_x$

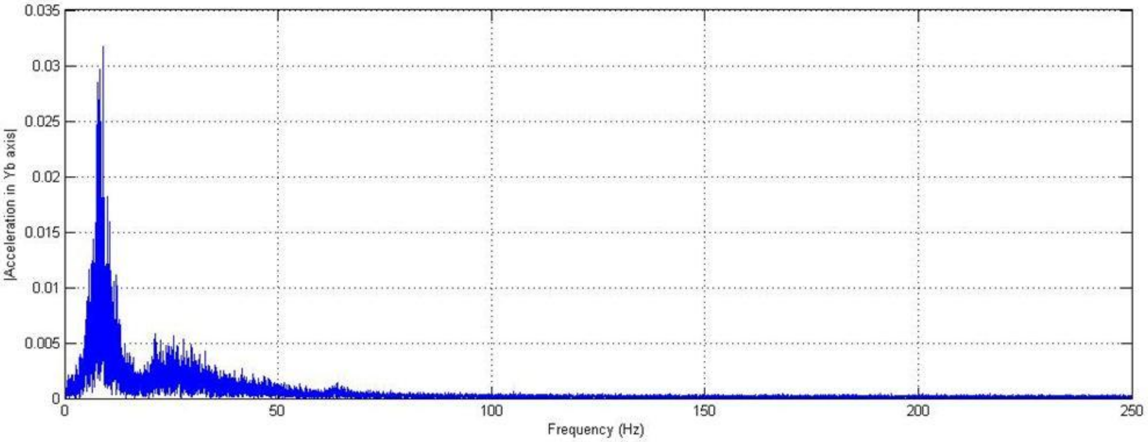

Figure 5.11: Single-sided frequency spectrum of $^{B}\tilde{a}_y$

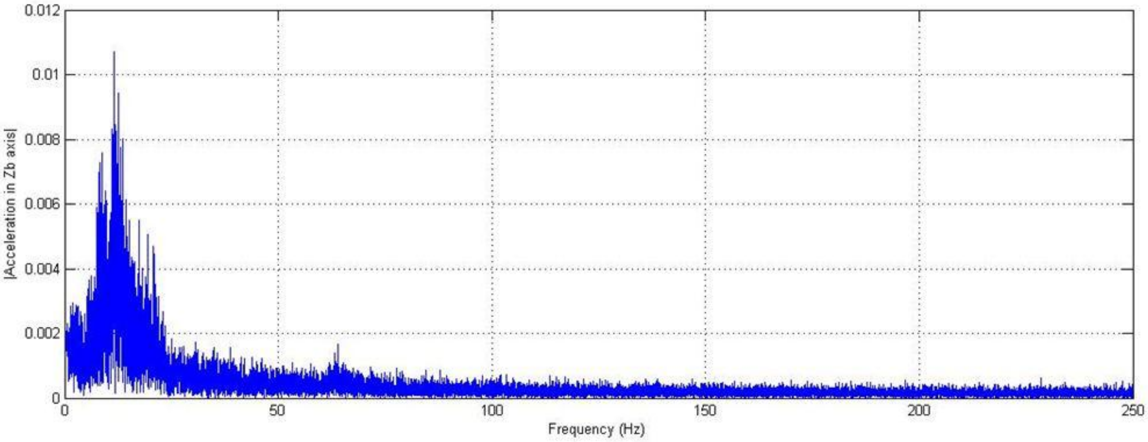

Figure 5.12: Single-sided frequency spectrum of $^{B}\tilde{a}_z$

Figures 5.10, 5.11 and 5.12 clearly show that $^{B}\tilde{A}$ is composed of the acceleration due to physiological tremor, residual low frequency components and noise. The figures also show that the frequency of the physiological tremor ranges from 8 to 12 Hz. Figure 5.13 shows the displacement due to tremor for a period of 7 seconds in the principal axes of the frame $\{B\}$. Figure 5.14 shows the displacement of the needle tip due to tremor for a period of 7 seconds with respect to the principal axes of the frame $\{S\}$. Figure 5.15 shows the single-sided frequency spectrum of the displacement due to tremor with respect to the principal axes of $\{B\}$. Figure 5.16 shows the single-sided frequency spectrum of the displacement due to tremor at the needle tip with respect to the principal axes of $\{S\}$.

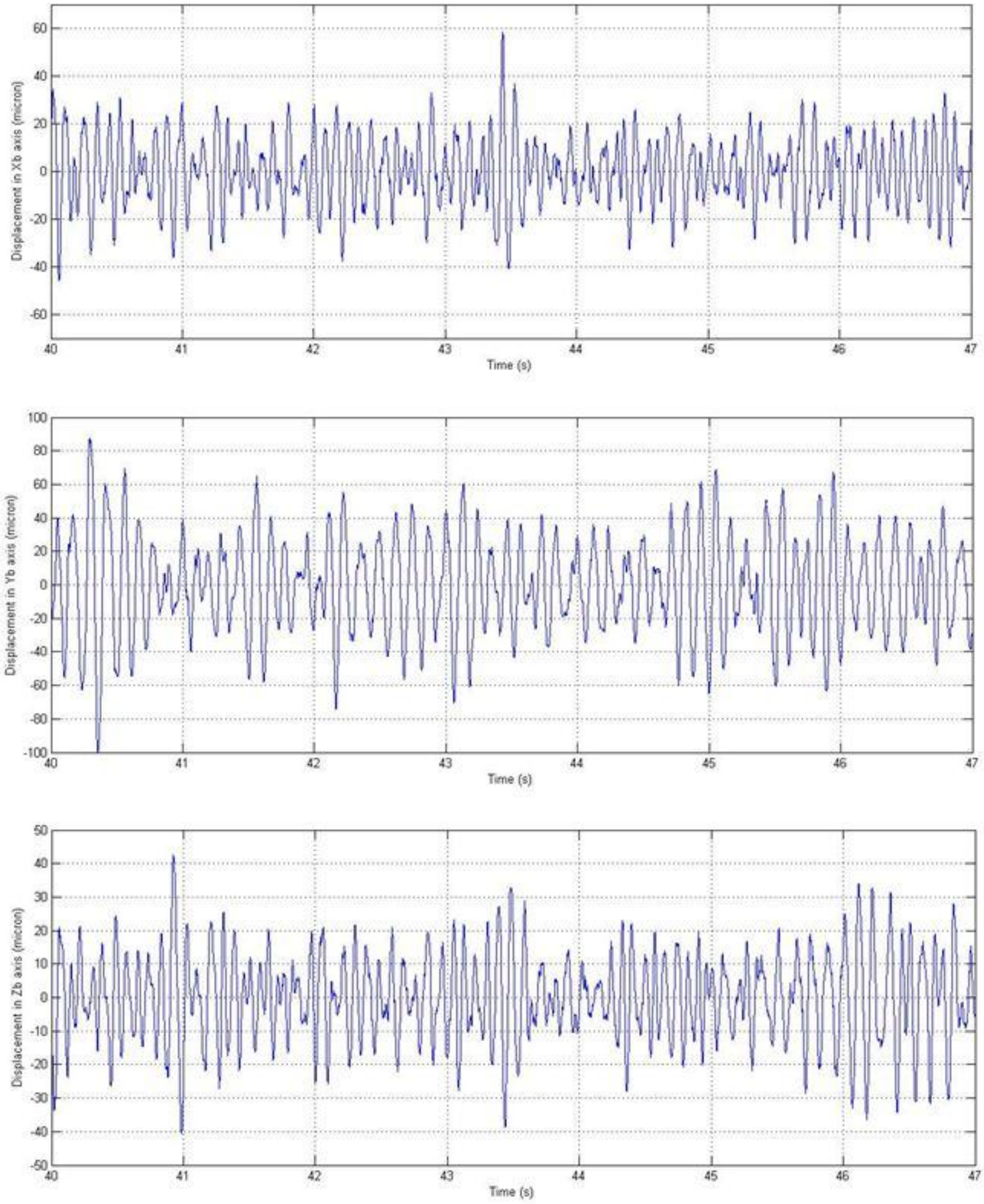

Figure 5.13: Displacement due to tremor with respect to {*B*}. (Top) X_B axis; (Middle) Y_B axis; (Bottom) Z_B axis

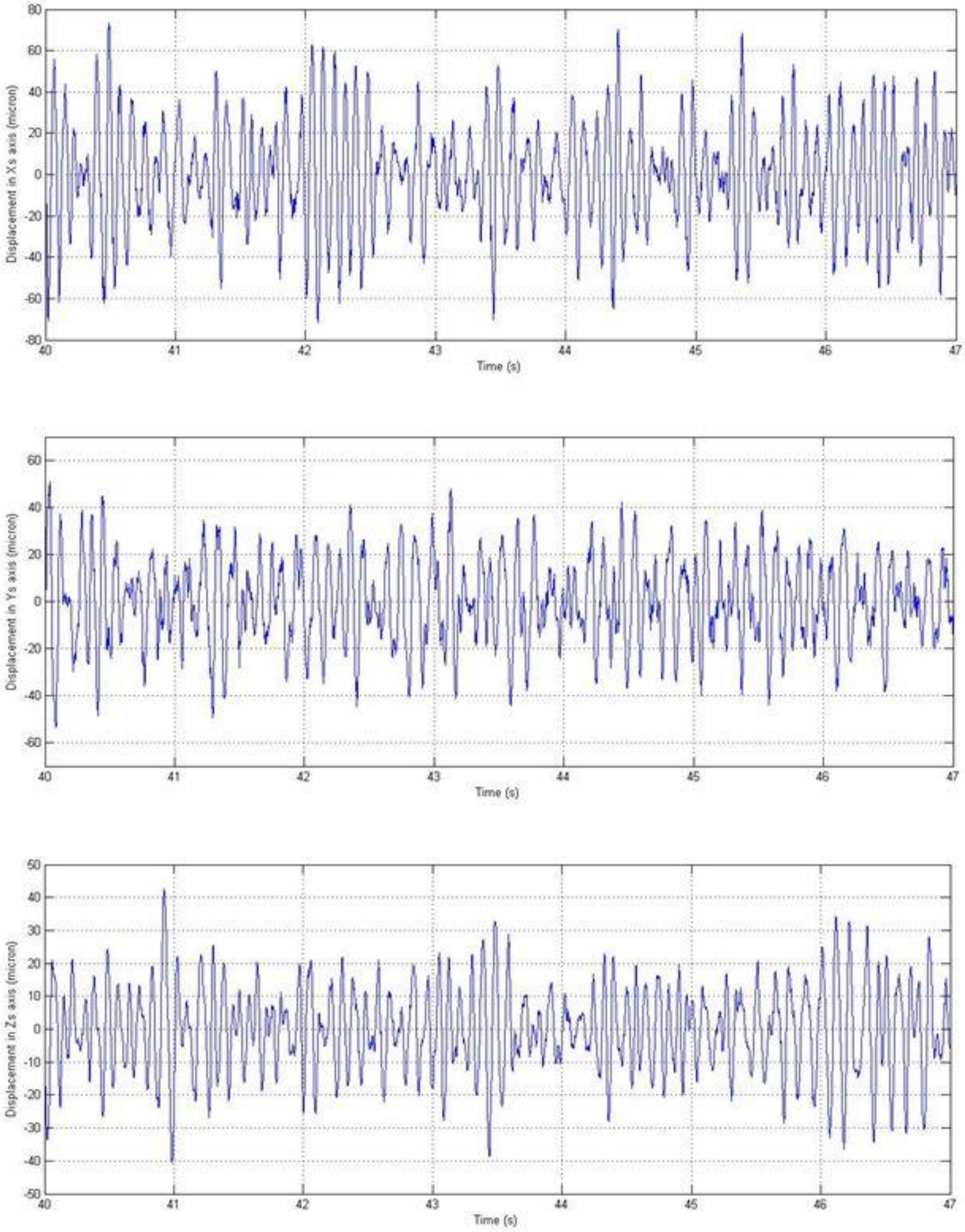

Figure 5.14: Displacement due to tremor at the needle tip with respect to {*S*}. (Top) *Xs* axis; (Middle) Y_S axis; (Bottom) Z_S axis

The pass-band frequency for the adaptive filter, BMFLC, is 7-13 Hz. Comparing Figure 5.10 and Figure 5.15, it is clear that the BMFLC adapts to the 7-13 Hz frequency band.

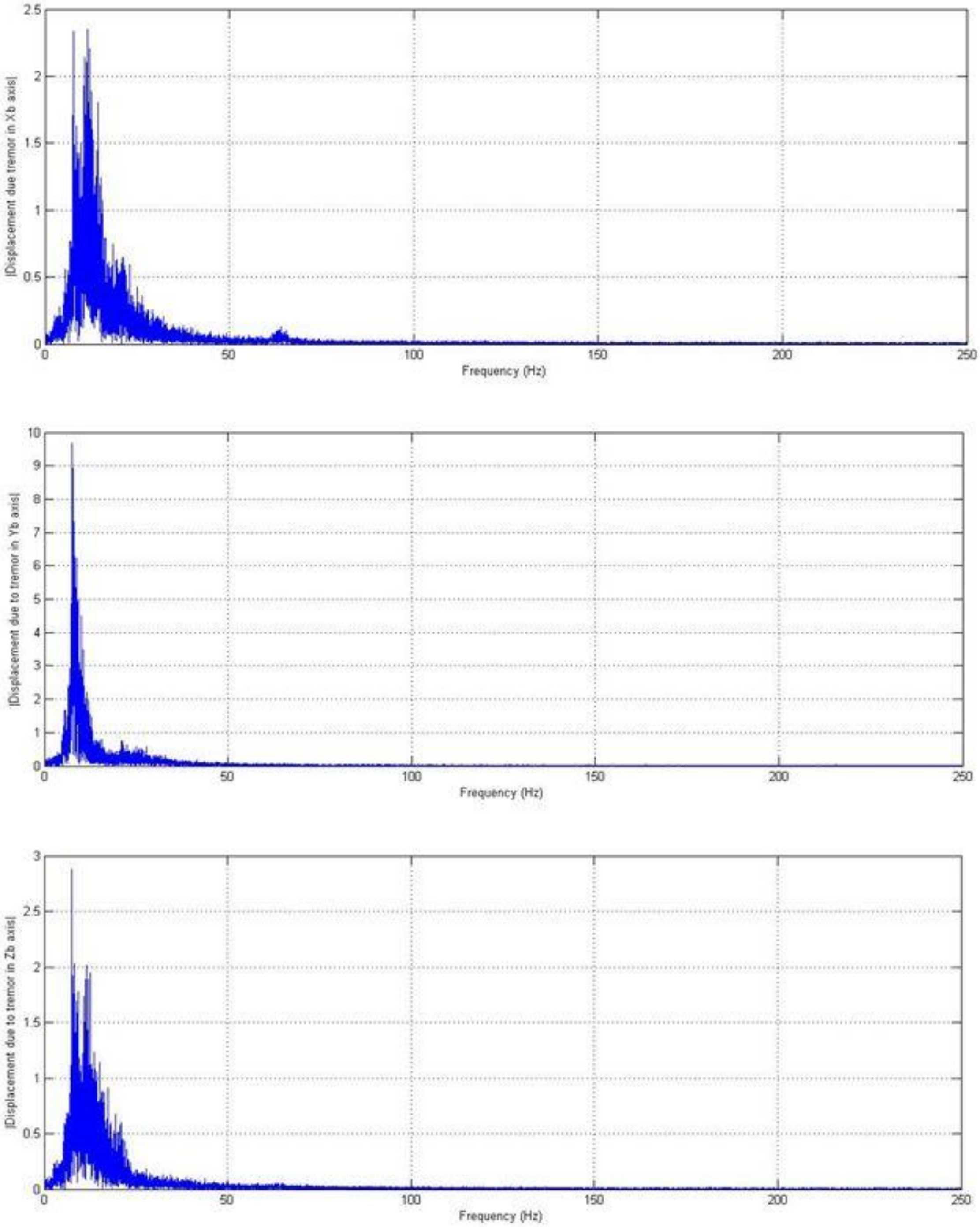

Figure 5.15: Single-sided frequency spectrum of displacement due to tremor with respect to {*B*}. (Top) X_B axis; (Middle) Y_B axis; (Bottom) Z_B axis

The displacement due to tremor contains negligible amount of the components outside of the pass-band as shown in Figure 5.15 and 5.16.

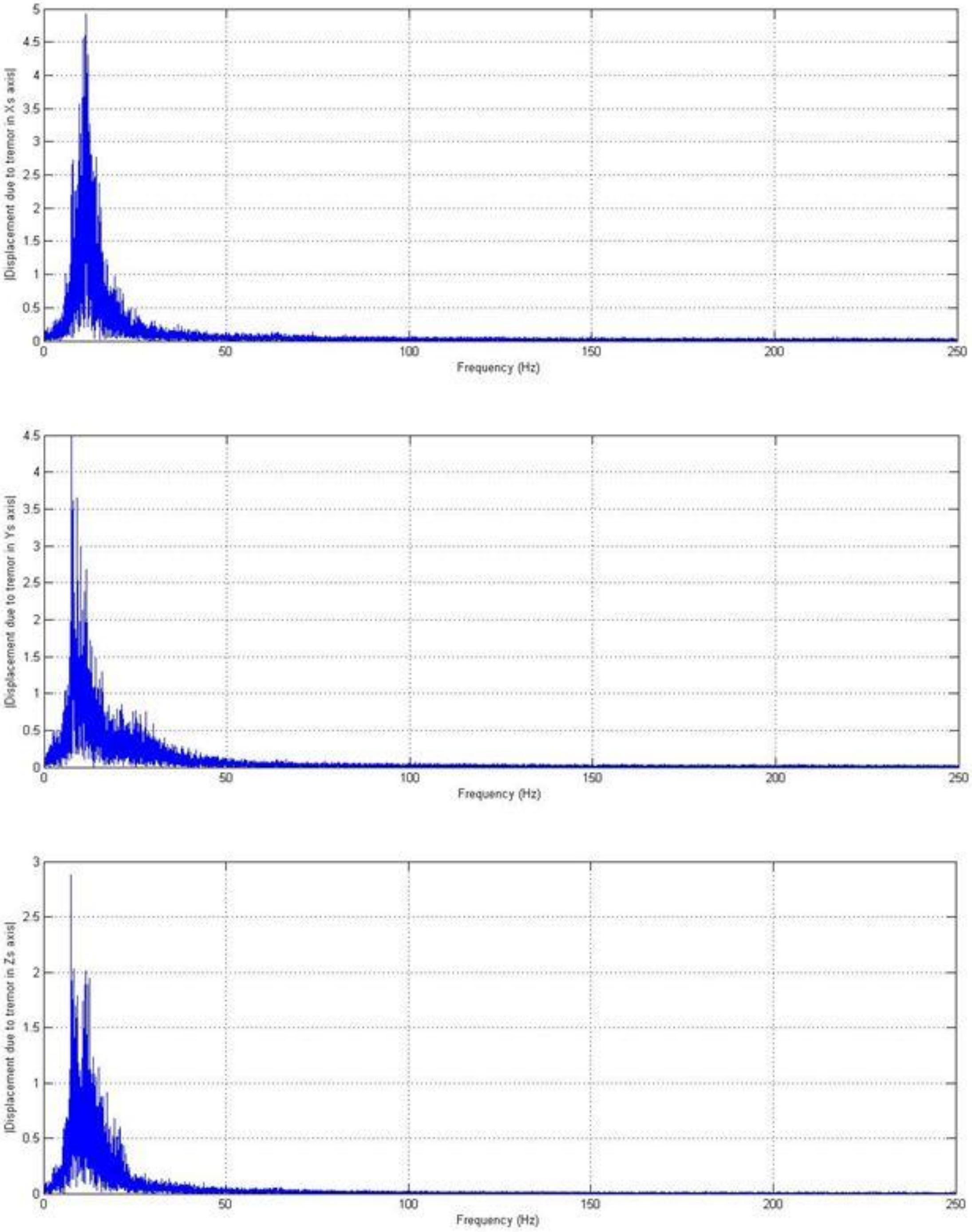

Figure 5.16: Single-sided frequency spectrum of displacement of the needle tip due to tremor with respect to {S}. (Top) X_S axis; (Middle) Y_S axis; (Bottom) Z_S axis

5.3 Tremor Compensation

This section presents the experimental design followed by an analysis of the results for testing the AID for compensating vibrations in 1 DOF.

5.3.1 Experimental Design

A parallel-plate capacitive sensing method was used to measure the amount of tremor compensation achieved by the AID. The method includes measuring the capacitance between two conducting parallel plates as shown in Figure 5.17.

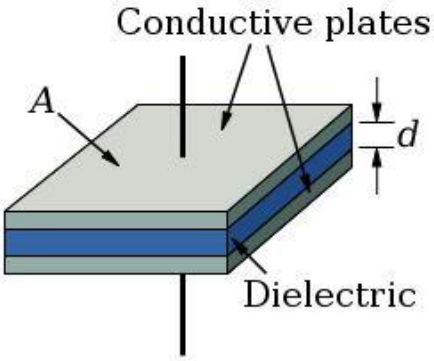

Figure 5.17: A parallel-plate capacitor

The relationship between the capacitance and the distance between the plates is given by:

$$C = \frac{k\varepsilon_0 A}{d} \tag{5.1}$$

where k is the relative permittivity of the dielectric material between the plates, ε_0 is the permittivity of space, A is the area of the plate, C is the capacitance and d is the distance between the plates. Vibrations between the two plates can be calculated by keeping one of the plates fixed and vibrating the other plate and measuring the capacitance. The capacitance can, then, be converted to the displacement using equation 5.1.

In the experiment, the AID was attached to a precision motor linear stage (marked as 'LS'), TLSM 50A (Zaber Technologies), as shown in Figure 5.18. The set-up allowed vibrating the AID along Y_S axis (the axis is shown in Figure 5.18). A copper plate was attached to the manipulator of the AID (marked as 'M') and another plate was kept fixed (marked as 'F') and kept parallel to the plate attached to the manipulator of the AID as shown in Figure 5.18. The plates were made up of copper and the area of the plates was 600 mm^2. The weight of plate attached to the AID (plate M) was 5.5 gm which was significantly heavier than the needle holder (the weight of the needle holder was 0.7 gm).

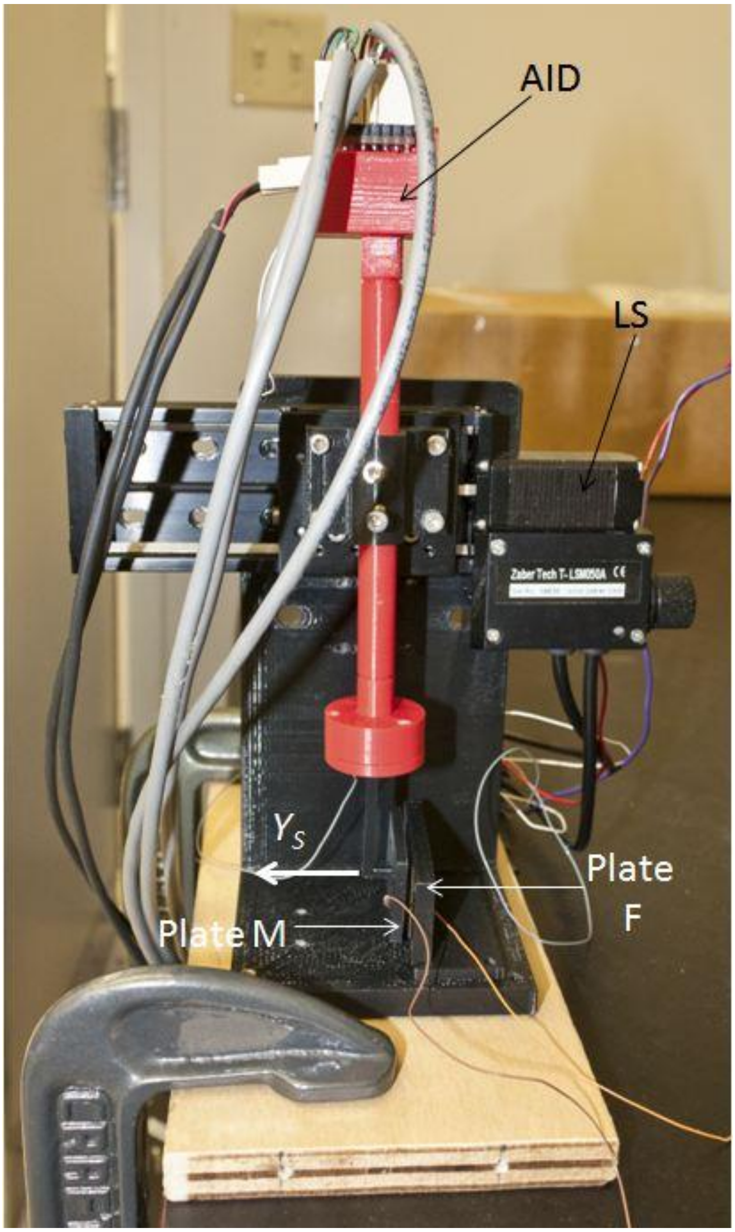

Figure 5.18: Experimental set-up for testing amount of compensation using the AID

The capacitance between these two plates was measured using PICOCAP evaluation kit (Acam) [109]. Four sets of experiments were carried out. The frequency, the peak-to-peak (p-p) amplitude and the rms value of the sinusoidal input to the linear stage for each set are listed in Table 5.3. The experimental set-up allowed testing the effects of different frequencies and amplitudes of vibration on the amount of tremor compensation by the AID. The compensation was started at ten seconds.

Before starting the experiments, the two plates (M and F) were kept at a known distance ($d_{initial}$). The linear stage was vibrated with the frequencies and the magnitudes listed in Table 5.3. The capacitance was measured using PICOCAP evaluation kit at a sampling frequency of 391 Hz. The manipulator of the AID gives angular motion to the plate 'M'. Since the magnitude of the motion was very low, the errors due to the angular motion in the measurement of the capacitance were also low and, thus, were not accounted for in the experiments. The measured capacitance was converted to displacement using eq. 5.1 and the initial distance ($d_{initial}$) between the plates was subtracted to calculate the displacement due to the vibration created by the linear stage (LS).

Table 5.3: Frequency, amplitude and rms value of the input to the linear stage

Set	Freq. of input (Hz)	Amplitude (p-p) (µm)	RMS of input to LS (µm)
1	8	80	28.28
2	10	75	26.52
3	12	80	28.28
4	12	100	35.35

5.3.2 Results and Analyses

Figure 5.19 shows the displacement of the copper plate fixed on the manipulator of the AID calculated using the capacitive method for set 2. The displacement before ten seconds is the uncompensated vibration of the plate while the displacement after 10 seconds is the compensated vibration of the plate.

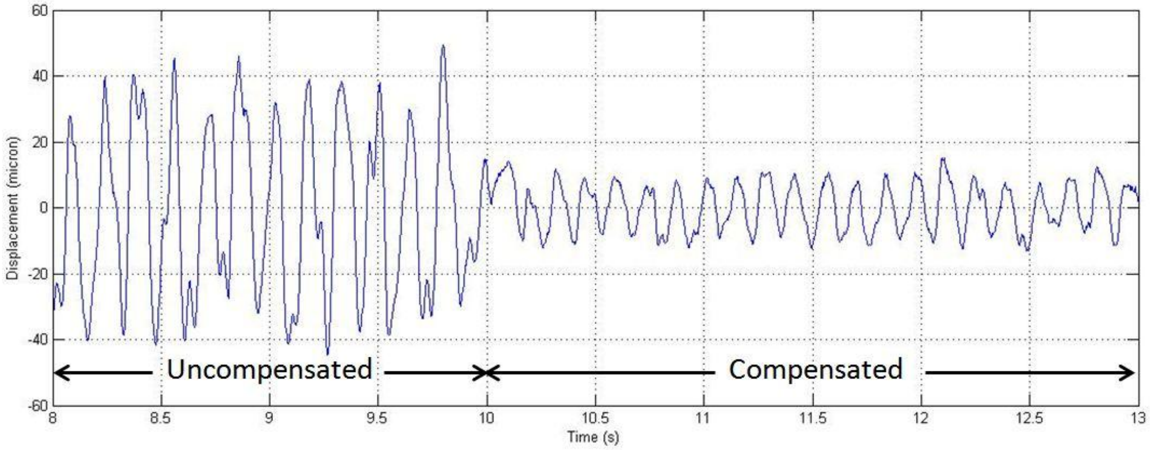

Figure 5.19: Displacement of the plate fixed on the manipulator of the AID measured using the capacitive method for set 1.

Figure 5.19 clearly shows that the AID compensates from the vibrations after ten seconds. The rms of the displacement using the capacitive method (CM) due to the vibration before and after the compensation was calculated to measure the amount of compensation by the AID. Table 5.4 lists the frequency and the rms value of the input to LS, the rms value of the vibration calculated by the AID, the rms value of the vibration before the compensation using CM (P_{LS}), the rms value of the vibration after the compensation using CM (P_{AID}) and the amount of compensation by the AID for each set of the experiments.

Table 5.4: Amount of compensation by AID for each set of experiment

Set	Freq. of input to LS (Hz)	RMS of input vibrations to LS (µm)	RMS of vibration using the AID (µm)	RMS of vibration before compensation using CM (µm)	RMS of vibration after compensation using CM (µm)	Amount of compensation (%)
1	8	28.28	23.69	25.45	7.393	70.95
2	10	26.52	22.09	24.7	7.217	70.78
3	12	28.28	23.63	26.84	10.5	60.87
4	12	35.35	29.2	33.81	14.81	56.19

The amount of compensation in percentage was calculated using:

$$\text{Compensation}\,(\%) = \frac{P_{LS} - P_{AID}}{P_{LS}} \text{ x } 100 \tag{5.2}$$

Comparing the results of Sets 1 and 3 from Table 5.3, it is clear that when the rms value of the input vibrations was kept constant and the frequency was increased from 8 Hz to 12 Hz, the amount of compensation was reduced. Although the accuracy of sensing the vibrations by the AID was similar for both cases, the amount of compensation by the AID was less in the case of higher frequency. The reason is that the displacement by the IPMC actuator is lower for higher frequencies as presented in Chapter 3. In Sets 3 and 4, the frequency of the input vibration was kept constant and the amplitude of the vibration was increased from 28.28 µm (rms) to 35.35 µm (rms). It is clear from Table 5.3 that the amount of compensation by the AID was higher in the case of lower amplitude. Although, the accuracy of sensing the vibrations by the AID for both the cases was the same (the attenuation in sensing the vibrations by the AID is 16.4% for Set 3 and 17.39% for Set 4), the amount of compensation was lower in Set 4 as compared to Set 3. Therefore, it can be concluded that the limiting factor in achieving higher compensation is the IPMC actuator.

Figure 5.20 shows the input to the IPMC actuator calculated by the AID.

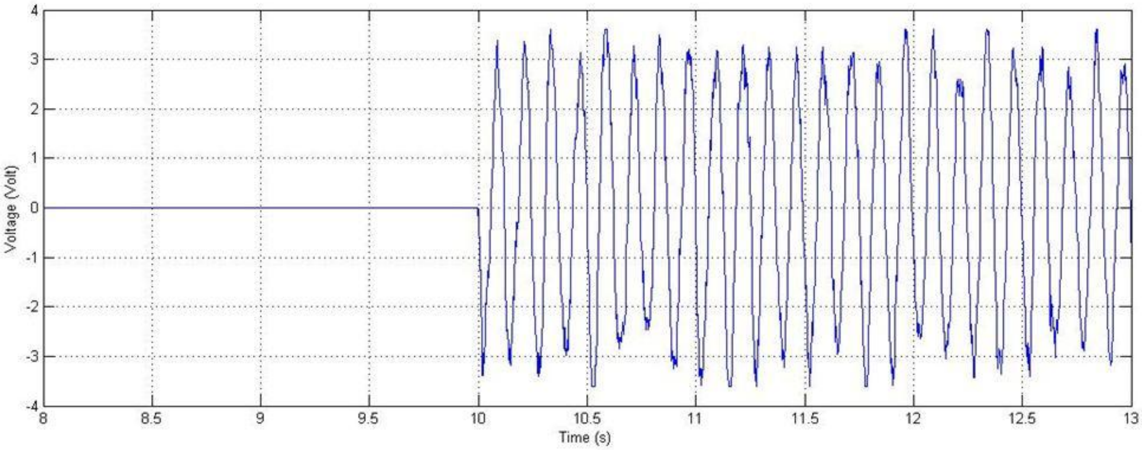

Figure 5.20: Input to the IPMC actuator calculated by the AID

As it can be seen from Figure 5.20, the peak-to-peak input voltage to the IPMC was approximately 3.2 V for Set 1. Since the controller limits the voltage to ±3.6 V, it is clear that the IPMC was driven by an input voltage that was close to the maximum rated voltage. As listed in Table 5.3, the amount of compensation for Set 1 was 70.95%. This also concludes that the limiting factor in achieving higher compensation is the IPMC actuator. However, in the experiments, a copper plate that weighed 5.5 gm was attached to the manipulator instead of a lighter needle holder. Since the displacement of the IPMC actuator decreases for higher loads, higher amount of compensation can be achieved in compensating tremor using the needle because of its light weight.

Comparing Set 1 and 2, it is clear that when the amplitude of the vibration was reduced from 28.28 µm (rms) to 26.52 µm (rms) and the frequency of the vibrations was increased from 8 Hz to 10 Hz, there is negligible effect on the amount of compensation by the AID. It is evident from Table 5.3 that the AID compensates for the vibrations: the amount of compensation depends on the frequencies and the amplitudes of the vibrations.

Chapter 6

6 Conclusion & Future work

This chapter presents concluding remarks including a statement of the key contributions of the thesis and a discussion of the limitations of the system. This is followed by a presentation of some ideas for improving the performance of the system.

6.1 Conclusion

As discussed in Chapter 1, the involuntary motions in the hand due to the physiological tremor can have a significant deteriorating effect on the performance of microsurgical procedures such as vitreoretinal microsurgery or intraocular cannulation. The chapter presented an overview of the previous technologies developed to compensate for the involuntary motions followed by a brief description of active compensation of the physiological tremor using a handheld instrument. In the thesis, system design and experimental results were presented for a novel active handheld device, AID, that senses the physiological tremor in the hand and compensates for it. In the thesis, compensation in only 1 DOF has been considered by deflecting the tool-tip appropriately.

The sensing system for the device was presented in Chapter 2. It incorporates MEMS based tri-axial accelerometer and gyroscopes to sense the motion of the hand in 6 DOF. The challenge was to filter the physiological tremor in real-time from the sensed hand motion, which has low signal-to-noise ratio. An algorithm was presented that estimates the physiological tremor in the sensed motion. Since gyroscopes, which suffered from drifting bias, were used, the challenge was to estimate the angular motion of the hand accurately. The orientation tracking was implemented using an augmented state complementary Kalman filter. Since the orientation calculated using the gyroscopes suffers from integration drift due to the noise and the orientation calculated using the tri-axial accelerometer is noisy and is susceptible to vibrations, the proposed Kalman filter fuses these two measurements to provide a drift-free and reduced-noise estimation of the orientation. The physiological tremor was estimated using a zero-phase adaptive filtering algorithm, band-limited multiple Fourier linear combiner (BMFLC) [70].

Ionic polymer metallic composite (IPMC) material was chosen as the actuator to deflect the needle-tip of the device because of its lower voltage requirement, light weight, compact size and the ability to be fabricated in any size and shape. This was discussed in Chapter 3 and an open-loop controller was presented in the chapter to drive the IPMC actuator.

The design, specifications, hardware and software components for the tremor compensation (AID) were described in Chapter 4. The validation of the AID was carried out via a number of experiments whose results were presented in Chapter 5.

6.2 Thesis Contributions

The major contributions of the thesis can be summarized as follows:

1. Development of a novel handheld device for active compensation of physiological tremor in the hand that is relatively inexpensive, light in weight (weighs 23.56 gm) and compact in size.

2. Design and implementation of an IPMC based 1 DOF manipulation system. To the author's knowledge, IPMC actuators have not been utilized for tremor compensation to date.

3. Design and implementation of an algorithm to measure the physiological tremor in 3 DOF using MEMS based tri-axial accelerometer and gyroscopes.

6.3 Future work

The prototype of the AID presented in the thesis has not yet reached its full design and, therefore, has not yet realized its full potential in terms of compensating for physiological tremor in the human hand. As a result of the difficulty encountered in obtaining appropriately designed IPMC actuators, the design of the AID was limited to a 1 DOF manipulation and, thus it can only compensate for physiological tremor in 1 DOF. A complete 3 DOF manipulation system needs to be designed which will allow compensating for the tremor in all three degrees of freedom. Nevertheless, based on the results presented in the thesis, the current prototype has demonstrated the feasibility of using IPMC actuators for active tremor compensation. Compared to other smart-material-based actuators such as piezoelectric, the use of IPMCs allow the design of a device that is light in weight, compact in size and cost effective. More engineering effort will be required to perform 3-DOF manipulation using IPMCs. A 3-DOF system could also allow the incorporation of other surgical tools such as forceps. As presented in the thesis, the current prototype employs an open-loop controller for the IPMCs. A more sophisticated closed-loop controller can be designed to enhance the motion tracking capability and, thus, increase the amount and robustness of the compensation.

As presented in Chapter 5, the current prototype of the AID was tested for compensating vibrations composed of single frequencies (ranging from 8 Hz to 12 Hz). Therefore, the device needs to be tested for compensating for modulated vibrations containing multiple frequencies. The device has not yet been tested for compensation during handheld conditions. For this, a more sophisticated experimental setup is necessary to assess the effectiveness of the AID in compensating for actual physiological tremor in the hand. More comprehensive experimental methods such as using optical tracking of the needle-tip will also be required for this purpose.

One of the limitations of the system is that the software is programmed using Matlab and QuaRC running on a Windows PC. This only allows a soft real-time implementation of the algorithm. A better solution is to use a real-time operating system such as QNX that allows true real-time implementation of hardware-in-the-loop environments.

In terms of comfort in using the AID, the cables from the sensor module restrict the motion of the hand somewhat because of their high stiffness. This can be addressed by using softer cables or re-designing the sensor module with wireless communication with the host computer.

Although, the thesis focuses on compensating the physiological tremor for a surgical device, the concept of tremor compensation using IPMCs can be applied in areas that require micromanipulation such as handheld photography. The proposed augmented state complementary Kalman filter can be utilized in human body orientation tracking. With tweaking of the parameters and the filter model, it can also be utilized in aerospace and robotic applications where 2 DOF orientation is required.

References

[1] J.H. McAuley and C.D. Marsden, "Physiological and Pathological Tremors and Rhythmic Central Motor Control," *Brain*, vol. 123, no. 8, pp. 1545-1567, 2000.

[2] M. Hallet, "Overview of Human Tremor Physiology," *Movement Disorders*, vol. 13, no. S3, pp. 43-48, 1998.

[3] S. Sagma, "Tremor," *American Family Physician*, vol. 68, no. 8, pp. 1545-1552, 2003.

[4] D.P. Charles, G.J. Esper, T.L. Davis, R.J. Macinuas, and Robertson D., "Classification of Tremor and Update of Tremor," *American Family Physician*, vol. 59, no. 6, pp. 1565-1572, 1999.

[5] G. Grimaldi and M. Manto, *Tremor: From Pathogenesis to Treatment*, John D. Enderle, Ed.: Morgan & Claypool Publishers, 2008.

[6] M. Maria, G. Grimaldi, T. Lorivel, D. Farina, and L. Popvic, "Bioinformatics Approaches Used in Modelling Human Tremor," *Current Bioinformatics*, vol. 4, no. 2, pp. 154-172, 2009.

[7] G. Deuschi, M. Lauk, and J. Timmer, "Tremor Classification and Tremor Time Series Analysis," *Chaos*, vol. 5, no. 1, pp. 48-51, 1995.

[8] E. Rocon, J.M. Belda-Lois, J.J. Sanchez-Lacuesta, and J.L. Pons, "Pathological Tremor Management: Modelling, Compensatory Technology and Evaluation," *Technology and Disability*, vol. 16, no. 1, pp. 3-18, 2004.

[9] R.J. Elble, "Essential Tremor Frequency Decreases with Time," *Neurology*, vol. 55, no. 10, pp. 1547-1551, 2000.

[10] V.G. Evidente, "Understanding Essential Tremor. Differential Diagnosis and Options for Treatment," *Postgraduate Medicine*, vol. 108, no. 5, pp. 138-149, 2000.

[11] Brown University. DBS: Deep Brain Simulation. [Online]. http://biomed.brown.edu/Courses/BI108/BI108_2008_Groups/group07/Parkinsons.html

[12] M. Rosen, "Tremor suppressing hand controls," 4689449, August 25, 1987.

[13] Neater Solutions Ltd. [Online]. http://www.neater.co.uk/main.htm

[14] E. Rocon et al., "Design and Validation of a Rehabilitation Robotic Exoskeleton for Tremor Assessment and Suppression," *IEEE Transactions on Neural Systems and Rehabilitation Engineering*, vol. 15, no. 3, pp. 367-378, September 2007.

[15] A.F. Ruiz, A. Forner-Cordero, E. Rocon, and J.L. Pons, "Exoskeletons for Rehabilitation and Motor Control," in *IEEE/RAS-EMBS International Conference on Biomedical Robotics and Biomechatronics (BioRob)*, 2006, pp. 601-606.

[16] E. Rocon, A.F. Ruiz, F. Brunetti, and J.M. Belda-Lois, J.J. Sanchez-Lacuesta J.L. Pons, "On the use of an active wearable exoskeleton for tremor suppression via biomechanical loading," in *Proceedings of the 2006 IEEE Internation Conference on Robotics and Automation (ICRA)*, 2006, pp. 3140-3145.

[17] J.L. Levine and M.A. Schappert, "A mouse adapter for people with hand tremor," *IBM Systems Journal*, vol. 44, no. 3, pp. 621-628, 2005.

[18] The Robotics Institute, Carnegie Mellon University. [Online]. http://www.cs.cmu.edu/~micron/index.htm

[19] R.J. Elble, "Central Mechanism of tremor," *Journal of Clinical Neurophysiology*, vol. 13, no. 2, pp. 133-144, 1996.

[20] R.J. Elble, "Characteristics of physiologic tremor in young and elderly adults," *Journal of Clinical Neurophysiology*, vol. 114, no. 4, pp. 624-635, 2003.

[21] R.J. Elble and J.E. Randall, "Mechanistic components of normal hand tremor," *Journal of Electroencephalography and Clinical Neurophysiology*, vol. 44, no. 1, pp. 72-82, 1978.

[22] C.D. Marsden, J.C. Meadows, G.W. Lange, and R.S. Watson, "The role of ballistocardiac impulse in the genesis of physiological tremor," *Brain*, vol. 92, no. 3, pp. 647-662, 1969.

[23] F.R. Fox and F.E. Randall, "Relationship between forearm tremor and the biceps electromyogram," *Journal of Applied Physiology*, vol. 29, no. 1, pp. 103-108, 1970.

[24] R.N. Stiles and J.E. Randall, "Mechanical factors in human tremor frequency," *Journal of Applied Physiology*, vol. 23, no. 3, pp. 324-330, 1967.

[25] H. Bengi and J.G. Thomas, "Studies on human ocular tremor," *Perspectives in Biomedical Engineering*, pp. 281-292, 1973.

[26] G.C. Higgins and K.F. Stultz, "Frequency and amplitude of ocular tremor," *Journal of Optical Society of America*, vol. 43, no. 12, pp. 1136-1150, 1953.

[27] P.S. Slack and X. Ma, "Tremor amplitude determination for use in clinical application," *Measurement Science and Technology*, vol. 18, no. 11, pp. 3471-3478, 2007.

[28] W. Growdon et al., "Effects of proximal and dsital muscles' group contraction and mental stress on the amplitude and frequency of physiological finger tremor. An accelerometric study," *Journal of Electromyography and Clinical Neurophysiology*, vol. 40, no. 5, pp. 295-303, 2000.

[29] D. Brei, J. Vendlinski, D.K. Lindner, H. Zhu, and C. LaVigna, "Development and Demonstration of INSTAR- Inertially Stabilized Rifle," in *Proceedings of SPIE, Smart Structures and Materials 2003: Smart Structures and Integrated Systems*, 2003, pp. 255-266.

[30] R.V. Wahlde, M. Kregel, T. Haug, and T. Brosseau, "Application of an Inertial Reticle System to an Objective Personal Weapon," Army Research Laboratory, Aberdeen Proving Ground MD, ARL-MR-289, 1996.

[31] H. Furukawa, "Image Stabilizing Optical System having a variable prism," 3942862, March 9, 1976.

[32] Nikon. [Online]. http://www.nikon.com/about/technology/rd/core/software/vr_e/index.htm

[33] P.K. Burian. (2005) Shutterbug. [Online]. http://www.shutterbug.com/content/konica-minolta-maxxum-7d-brfirst-d-slr-camera-built-anti-shake-system-page-2

[34] J.Y. Chang, W.F. Hu, M.H. Cheng, and B.S. Chang, "Digital Image Translation and Rotational Motion Stabilization using Optical Flow Technique," *IEEE Transactions on Consumer Electronics*, vol. 48, no. 1, pp. 108-115, 2002.

[35] A. Levin, P.Sand, T.S. Cho, F. Durand, and W.T. Freeman, "Motion-Invariant Photography," *ACM Transations on Graphics- Proceedings of ACM SIGGRAPH 2008*, vol. 27, no. 3, pp. 71:1-9, 2008.

[36] W.M. Tang and D.P. Han, "A study of surgical approaches to retinal vascular occlusions," *Archives of Ophthalmology*, vol. 118, no. 1, pp. 138-143, 2000.

[37] J.N. Weiss, "Treatment of central retinal vein occlusion by injection of tissue plasminogen activator into a retinal vein," *American Journal of Ophthalmology*,

vol. 136, no. 1, pp. 142-144, 1998.

[38] M. Patkin, "Ergonomics applied to the practice of microsurgery," *Australian and New Zealand Journal of Surgery*, vol. 47, no. 3, pp. 320-329, 1977.

[39] M.U. Humayun, R.S. Rader, D.J. Pieramici, C.C. Awh, and E. Juan Jr., "Quantitative Measurement of the effects of caffeine and propranolol on surgeon hand tremor," *Archives of Ophthalmology*, vol. 115, no. 3, pp. 371-374, 1997.

[40] M.J. Elman et al., "The effect of propranolol versus placebo on resident surgical performance," *Transactions of the American Ophthalmological Society*, vol. 96, pp. 283-294, 1998.

[41] S.P.N. Singh and C.N. Riviere, "Physiological Tremor Amplitude during Retinal Surgery," in *Proceedings of the IEEE 28th Annual Northeast Bioengineering Conference*, 2001, pp. 171-172.

[42] P.S. Schenker, H. Das, and T.R. Ohm, "Development of a new high-dexterity manipulator for robot-assisted microsurgery," in *Proceedings of SPIE Conference on Telemanipulator and Telepresence Technologies*, vol. 2351, 1994, pp. 191-198.

[43] P.S. Schenker et al., "Development of a Telemanipulator for Dexterity Enhanced Microsurgery," in *Proceedings of the 2nd International Symposium on Medical Robotics and Computer Assisted Surgery*, 1995, pp. 81-88.

[44] P.S. Schenker, H. Das, and T.R. Ohm, "A New Robot for High Dexterity Microsurgery," in *First International Conference in Computer Vision, Virtual Reality and Robotics in Medicine*, vol. 905, 1995, pp. 115-122.

[45] H. Das et al., "Telerobotics for Microsurgery," in *Proceedings of the 18th Annural International Conference of the IEEE Engineering in Medicine and Biology Society*, vol. 1, 1996, pp. 227-228.

[46] H. Das, T. Ohm, C. Boswell, G. Rodriguez, and R. Steele, "Dexterity-enhanced Telerobotic Microsurgery," in *Proceedings of the 8th International Conference on Advanced Robotics*, 1997, pp. 5-10.

[47] H. Das, H. Zak, J. Johnson, J. Crouch, and D. Frambach, "Evaluation of a Telerobotic System to Assist Surgeons in Microsurgery," *Computer Aided Surgery*, vol. 4, no. 1, pp. 15-25, 1999.

[48] M. Siemionow, K. Ozer, W. Siemionow, and G. Lister, "Robotic Assistance in Microsurgery," *Journal of Reconstruction Microsurgery*, vol. 16, no. 8, pp. 643-650, 2000.

[49] B.D. Krapohl, B. Reichert, and H.G. Machens, "Computer-guided Microsurgery: Surgical Evaluation of a Telerobotic Arm," *Microsurgery*, vol. 21, no. 1, pp. 22-29, 2001.

[50] P. LeRoux, H. Das, S. Esquenazi, and R. Kelly, "Robot-assisted Microsurgery: A Feasibility Study in the Rat," *Neurosurgery*, vol. 48, no. 3, pp. 584-589, 2001.

[51] R.H. Taylor et al., "A Steady-hand Robotic System for Microsurgical Augmentation," *The International Journal of Robotics Research*, vol. 18, no. 2, pp. 1201-1210, 1999.

[52] B. Mitchell et al., "Development and Application of a New Steady-hand Manipulator for Retinal Surgery," in *Proceedings of the IEEE International Conference on Robotics and Automation*, 2000, pp. 623-629.

[53] R. Kumar, P. Jensen, and R.H. Taylor, "Experiments with a Stedy Hand Robot in Constrained Compliant Motion and Path Following," in *Proceedings of the 1999 IEEE International Workshop on Robot and Human Interaction*, 1999, pp. 92-97.

[54] R. Kumar et al., "Performance of Robotic Augmentation in Microsurgery- Scale

Motions," in *Medical Image Computing and Computer-Assisted Interventions*, vol. 1679, 1999, pp. 1108-115.

[55] W.T. Ang, C.N. Riviere, and P.K. Khosla, "An Active Hand-held Instrument for Enhanced Microsurgical Accuracy," in *Proceedings of the 3rd International Conference on Medical Image Computing and Computer-assisted Intervention*, vol. 1935, 2000, pp. 878-886.

[56] W.T. Ang, C.N. Riviere, and P.K. Khosla, "Design and Implementation of Active Error Canceling in Hand-held Microsurgical Instrument," in *Proceedings of the 2001 IEEE/RSJ International Conference on Intelligent Robots and Systems*, 2001, pp. 1106-1111.

[57] W.T. Ang, P.K. Khosla, and C.N. Riviere, "An intelligent hand-held microsurgical instrument for improved accuracy," in *Proceedings of the 23rd Annual International Conference of the IEEE Engineering in Medicine and Biology Society*, vol. 4, 2001, pp. 3450-3453.

[58] C.N. Riviere, W.T. Ang, and P.K. Khosla, "Toward Active Tremor Canceling in Handheld Mircosurgical Instruments," *IEEE Transactions on Robotics and Automation*, vol. 19, no. 5, pp. 793-800, 2003.

[59] C.N. Riviere, R.S. Rader, and N.V. Thakor, "Adaptive Canceling of Physiological Tremor for Improved Precision in Microsurgery," *IEEE Transactions of Biomedical Engineering*, vol. 45, no. 7, pp. 839-846, 1998.

[60] L. Hotraphinyo and C.N. Riviere, "Precision measurement for microsurgical instrument evaluation," in *Proceedings of the 23rd Annual Conference on IEEE Engineering in Medicine and Biology Society*, vol. 4, 2001, pp. 3454-3457.

[61] W.T. Ang, P.K. Pradeep, and C.N. Riviere, "Active Tremor Compensation in Microsurgery," in *Proceedings of the 26th Annual International Conference of the IEEE Engineering in Medicine and Biology Society*, 2004, pp. 2378-2741.

[62] D.Y. Choi and C.N. Riviere, "Flexure-based Manipulator for Active Handheld Microsurgical Instrument," in *Proceedings of IEEE-EMBS 27th Annual Conference of Engineering in Medicine and Biology Society*, 2005, pp. 2325-2328.

[63] R.A. MacLachlan, B.C. Becker, and C.N. Riviere, "Control of an Active Handheld Instrument for Microsurgery and Micromanipulation," in *Proceedings of IEEE International Conference on Robotics and Automation*, 2009, pp. 29-31.

[64] B.C. Becker, S. Voros, R.A. MacLachlan, G.D. Hager, and C.N. Riviere, "Active guidance of a handheld micromanipulator using visual serviong," in *IEEE International Conference on Robotics and Automation*, 2009, pp. 339-344.

[65] B.C. Becker, C.R. Valdivieso, J. Biswas, L.A. Lobes, and C.N. Riviere, "Active Guidance for Laser Retinal Surgery with a Handheld Instrument," in *Proceedings of the Annual International Conference on the IEEE Engineering in Medicine and Biology Socity*, 2009, pp. 5587-5590.

[66] B.C. Becker, R.A. MacLachlan, L.A. Lobes, and C.N. Riviere, "Semiautomated Intraocular Laser Surgery using Handheld Instrument," *Lasers in Surgery and Medicine*, vol. 42, no. 3, pp. 264-273, March 2010.

[67] B.C. Becker et al., "Retinal Vessel Cannulation with an Image-Guided Handheld Robot," in *Proceedings of the Annual International Conference of the IEEE Engineering in Medicine and Biology Society*, 2010, pp. 5420-5423.

[68] J.C. Tabares, R.A. MacLachlan, C.A. Ettensohn, and C.N. Riviere, "Cell Manipulation with an Active Handheld Micromanipulator," in *Proceedings of the Annual International Conference of the IEEE Engineering in Medicine and Biology Society*, 2010, pp. 4363-4366.

[69] K.C. Veluvolo, U.X. Tan, W.T. Latt, C.Y. Shee, and W.T. Ang, "Bandlimited

Mutiple Fourier Linear Combiner for Real-time Tremor Compensation," in *Proceedings of the Annual International Conference of the IEEE EMBS*, 2007, pp. 2847-2850.

[70] U.X. Tan et al., "Estimating Displacement of Periodic Motion with Inertial Sensors," *IEEE Journal of Sensors*, vol. 8, no. 8, pp. 1385-1388, 2008.

[71] W.T. Latt, U.X. Tan, K.C. Veluvolo, C.Y. Shee, and W.T. Ang, "Physiological Tremor Sensing using only Accelerometers for Real-time Compensation," in *Proceedings of the IEEE International Conference on Robotics and Automation*, 2009, pp. 474-479.

[72] J.J. Craig, *Introduction to Robotics Mechanics and Control*, 3rd ed.: Pearson Education, Inc., 2009.

[73] E. Foxlin, M. Harrington, and Y. Altshuler, "Miniature 6-DOF inertial system for tracking HMDs," in *SPIE Helmet and Head-Mounted Displays III, AeroSense*, vol. 3362, Orlando, 1998.

[74] E. Foxlin, "Inertial Head-Tracker Fusion by a Complementary Separate-Bias Kalman Filter," in *Proceedings of VRAIS*, 1996, pp. 185-194.

[75] E.R. Bachmann et al., "Orientation Tracking for Humans and Robots using Inertial Sensors," in *IEEE International Symposium on Computational Intelligence in Robotics and Automation*, 1999, pp. 187-194.

[76] J.L. Marins, X. Yun, E.R. Buchmann, R.B. McGhee, and M.J. Zyada, "An Extended Kalman Filter for Quaternion-Based Orientation Estimation using MARG Sensor," in *Proceedings of 2001 IEEE/RSJ International Conference on Intelligent Robots and Systems*, vol. 4, 2001, pp. 2003-2011.

[77] X. Yun, M. Lizarraga, E.R. Buchmann, and R.B. McGhee, "An Improved Quaternion-Based Kalman Filter for Real-Time Tracking of Rigid Body

Orienation," in *Proceedings of IEEE/RSJ International Conference on Intelligent Robots and Systems*, vol. 2, 2003, pp. 1074-1079.

[78] E.R. Buchmann, X. Yun, D. McKinnery, R.B. McGhee, and M.J. Zyada, "Design and Implementation of MARG Sensors for 3 DOF Orientation Measurement of Rigid Bodies," in *Proceedings of IEEE International Conference on Robotics and Automation*, 2003, pp. 1171-1178.

[79] X. Yun, C. Aparicio, E.R. Buchmann, and R.B. McGhee, "Implementation and Experimental Results of a Quaternion-Based Kalman Filter for Human Body Motion Tracking," in *Proceedings of IEEE International Conference on Robotics and Automation*, 2005, pp. 317-322.

[80] M.D. Shuster and S.D. Oh, "Three-axis Attitude Determination from Vector Observations," *Journal of Guidance and Control*, vol. 4, no. 1, pp. 70-77, 1981.

[81] Robert B. McGhee, "The Factored Quaternion Algorithm for Orientation Estimation from Measured Earth Gravity and Magnetic Field," MOVES Institute, Naval Postgraduate School, Monterey, CA, Technical Memorandum 2004.

[82] Conrado Aparicio, "Implementation of a Quaternion-based Kalman Filter for Human Body Motion tracking using MARG Sensors," Naval Postgraduate School, Monterey, CA, Master's Thesis 2004.

[83] H.J. Luinge, P.H. Veltink, and C.T. Baten, "Estimating orientation with gyroscopes and accelerometers," *Journal of Technology and Health Care*, vol. 7, no. 6, pp. 455-459, 1999.

[84] H.J. Luinge, "Inertial Sensing of Human Movement," University of Twente, Enschede, Netherlands, PhD Thesis 2002.

[85] H.J. Luinge and P.H. Veltink, "Inclination measurement of human movement using a 3-D accelerometer with autocalibration," *IEEE Transactions on Neural*

Systems and Rehabilitation Engineering, vol. 12, no. 1, pp. 112-121, 2004.

[86] D. Roetenberg, H.J. Luinge, T.M. Baten, and P.H. Veltink, "Compensation of magnetic disturbances improves inertial and magnetic sensing of human body segment orientation," *IEEE Transactions on Neural Systems and Rehabilitation Engineering*, vol. 13, no. 3, pp. 395-405, 2005.

[87] D. Roetenberg, P.J. Slycke, and P.H. Veltink, "Ambulatory Position and Orientation Tracking Fusing Magnetic and Inertial Sensing," *IEEE Transactions on Biomedical Engineering*, vol. 54, no. 5, pp. 883-890, 2007.

[88] H.J. Luinge, P.H. Veltink, and C.T.M. Baten, "Ambulatory measurement of arm orientation," *Journal of Biomechanics*, vol. 40, no. 1, pp. 78-85, 2007.

[89] W.T. Ang, P.K. Khosla, and C.N. Riviere, "Design of All-Accelerometer Inertial Measurement Unit for Tremor Sensing in Hand-held Microsurgical Instrument," in *IEEE International Conference on Robotics and Automation*, 2003, pp. 1781-1786.

[90] W.T. Ang, P.K. Khosla, and C.N. Riviere, "Kalman Filtering for Real-Time Orientation Tracking of Handheld Microsurgical Instrument," in *IEEE/RSJ International Conference on Intelligent Robots and Systems*, vol. 3, 2004, pp. 2574-2580.

[91] H. Rehbinder and X. Hu, "Drift-free Attitude Estimation of Accelerated Rigid Bodies," *Automatica, Journal of the International Federation of Automatic Control*, vol. 40, no. 4, pp. 653-659, 2004.

[92] C. Vaz and N. Thakor, "Adaptive Fourier estimation of time-varying evoked potentials," *IEEE Transactions on Biomedical Engineering*, vol. 36, no. 4, pp. 448-455, 1989.

[93] C. Vaz, X. Kong, and N. Thakor, "Adaptive estimation of periodic signals using a

Fourier linear combiner," *IEEE Transactions on Signal Processing*, vol. 42, no. 1, pp. 1-10, 1994.

[94] B. Widrow and S.D. Stearns, *Adaptive Signal Processing*. Englewoods Cliffs, NJ, Unites States of America: Prentice-Hall, 1985.

[95] C.N. Riviere and N. Thakor, "Modeling and canceling tremor in human-machine interface," *IEEE Engineering in Medicine and Biology*, vol. 15, no. 3, pp. 29-36, 1996.

[96] P.K. Gupta, P.S. Jensen, and E. de Juan, "Surgical Forces and Tactile Perception During Retinal Microsurgery," in *Medical Image Computing and Computer-Assisted Interventions*, vol. 1679, 1999, pp. 1218-1225.

[97] J.E. Huber, N.A. Fleck, and M.F. Ashby, "The selection of mechanical actuators based on performance indices," *Proc. R. Soc. Lond. A*, vol. 453, no. 1965, pp. 2185-2205, October 1997.

[98] Barbar J. Akle, "Characterization and Modeling of the Ionomer-Conductor Interface in Ionic Polymer Transducers," Virginia Polytechnic Institute and State University, Blacksburg, Virginia, PhD Thesis 2005.

[99] Mohsen Shahinpoor and Kwang J. Kim, "Ionic Polymer-metal Composites: IV. Industrial and Medical Applications," *Smart Materials and Structures*, vol. 14, no. 1, pp. 197-214, 2005.

[100] H.P. Monner, "Smart Materials for Active Noise and Vibration Reduction," in *Proceedings of Novem- Noise and Vibration: Emerging Methods*, France, 2005.

[101] Tadasse Yonas, Thayer Nicholas, and Priya Shashank, "Tailoring the Response Time of Shape Memory Alloy Wires through Actie Cooling and Pre-stress," *Journal of Intelligent Material Systems and Structures*, vol. 21, no. 1, pp. 19-40, January 2010.

[102] Yoseph Bar-Cohen, *Electroactive Polymer (EAP) Actuators as Artifical Muscles-Reality, Potentional, and Challenges*, 2nd ed. Bellingham, Washingtom, United States of America: SPIE- The International Society for Optical Engineering, 2004.

[103] K. Oguro, Y. Kawami, and H. Takenaka, "Bending of an Ion-Conducting Polymer Film-Electrode Composite by an Electric Stimulus at Low Voltage," *Trans. Journal of Micro-machine Society*, vol. 5, pp. 27-30, 1992.

[104] K. Sadeghipour, Salomon R., and S. Neogi, "Development of a Novel Electrochemically Active Membrane and 'Smart' Material Based Vibration Sensor/Damper," *Smart Materials and Structures*, vol. 1, no. 2, pp. 172-179, June 1992.

[105] Kwangmok Jung, Jaedo Nam, and Hyoukryeol Choi, "Investigations on actuation characteristics of IPMC artifical muscle actuator," *Sensors and Actuators A: Physical*, vol. 107, no. 2, pp. 183-192, October 2003.

[106] Mohsen Shahinpoor and Kwang J Kim, "Ionic Polymer-metal Composites I: Fundamentals," *Smart Materials and Structures*, vol. 10, no. 4, pp. 819-833, August 2001.

[107] Mohsen Shahinpoor, Y. Bar-Cohen, J.O. Simpson, and J. Smith, "Ionic polymer-metal composites (IPMCs) as biomimetic sensors, actuator and artifical muscles-a review," *Smart Materials and Structures*, vol. 7, no. 6, pp. R15-R30, 1998.

[108] Control Design Software. [Online]. http://quanser.com/english/html/solutions/fs_soln_software.html

[109] Acam. [Online]. http://www.acam.de/products/picocap/

Appendix A: Calibration and Measurement Model for Inertial Measurement Unit

This section presents the calibration process and the measurement model of the inertial measurement unit (IMU) used in the AID. The calibration process measures the scale factors, axes misalignments and biases of the tri-axial accelerometer (ADXL 335), the initial offset and the sensitivity of the dual-axis gyroscope (IDG 500) and the single-axis gyroscope (MLX 90609). Figure A.1 shows the set-up for calibrating the IMU. It consists of two precision motor rotary stages, T-RS60A (Zaber Technologies). The sensor module is attached to rotary stage '2' and rotary stage '2' is mounted on rotary stage '1' as shown in the Figure A.1.

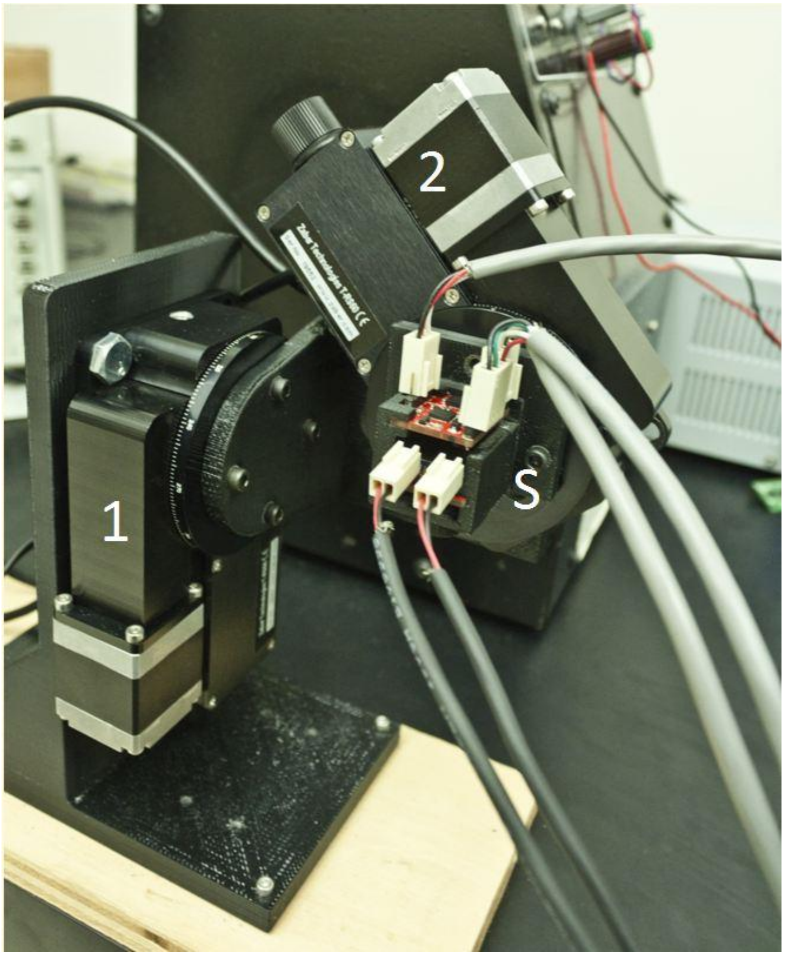

Figure A.1: Set-up for the IMU calibration process. The two rotary stages are marked as '1' and '2' and the sensor module is marked as 'S'.

In matrix form, the output of the tri-axial accelerometer can be written as:

$$a_v = \tilde{M} y_{a,g} + b_a \tag{A.1}$$

$$\begin{bmatrix} a_{x,v} \\ a_{y,v} \\ a_{z,v} \end{bmatrix} = \begin{bmatrix} s_{a,x} & m_{xy} & m_{xz} \\ m_{yx} & s_{a,y} & m_{yz} \\ m_{zx} & m_{zy} & s_{a,z} \end{bmatrix} \begin{bmatrix} y_{a,g,x} \\ y_{a,g,y} \\ y_{a,g,z} \end{bmatrix} + \begin{bmatrix} b_{a,x} \\ b_{a,y} \\ b_{a,z} \end{bmatrix} \tag{A.2}$$

where a_v represents the raw output of the tri-axial accelerometer (in volt), $y_{a,g}$ represents the acceleration in units of g[4] and b_a represents the corresponding biases. The off-diagonal elements of matrix $\tilde{M}$ represents the axes misalignments and $s_{a,i}$ ($i = x,y,z$) represents the scale factors. The goal of the section is to convert the signals measured using the tri-axial accelerometer in units of volt (a_v) to acceleration in units of m/s^2. Since the accelerometer measures the g-force, the signals from the accelerometer in units of volt are, first, converted to acceleration in units of g using equation A.2 and, then, to acceleration in m/s^2 using equation A.3. For this purpose, the twelve unknowns in equation A.2 needs to obtained using the calibration process. The acceleration in units of m/s^2, y_a, can be obtained using the following equation:

$$y_a = 9.804 \begin{bmatrix} y_{a,g,x} \\ y_{a,g,y} \\ y_{a,g,z} \end{bmatrix} \tag{A.3}$$

Equation A.2 can be written as:

$$\begin{bmatrix} a_{x,v} \\ a_{y,v} \\ a_{z,v} \end{bmatrix} = \begin{bmatrix} s_{a,x} & m_{xy} & m_{xz} & b_{a,x} \\ m_{yx} & s_{a,y} & m_{yz} & b_{a,y} \\ m_{zx} & m_{zy} & s_{a,z} & b_{a,z} \end{bmatrix} \begin{bmatrix} y_{a,g,x} \\ y_{a,g,y} \\ y_{a,g,z} \\ 1 \end{bmatrix} \tag{A.4}$$

---

[4] Accelerometers sense the g-force acting on each of the axis.

$$a_v = M a_g \tag{A.5}$$

The aim of the calibration process is to find the 12 unknown elements of matrix *M* so that the acceleration measured by the tri-axial accelerometer can be calculated in units of m/s^2. Six static known positions are used to calibrate the accelerometer and find the matrix *M* using the least squares method. These positions are shown in Figure A.2 and are listed in Table A.1. At each position, the raw data (in units of volt) is recorded. Since the position are known and the accelerometer measure the g-force, the ideal accelerations in units of g are known for each position and are listed in Table A.1.

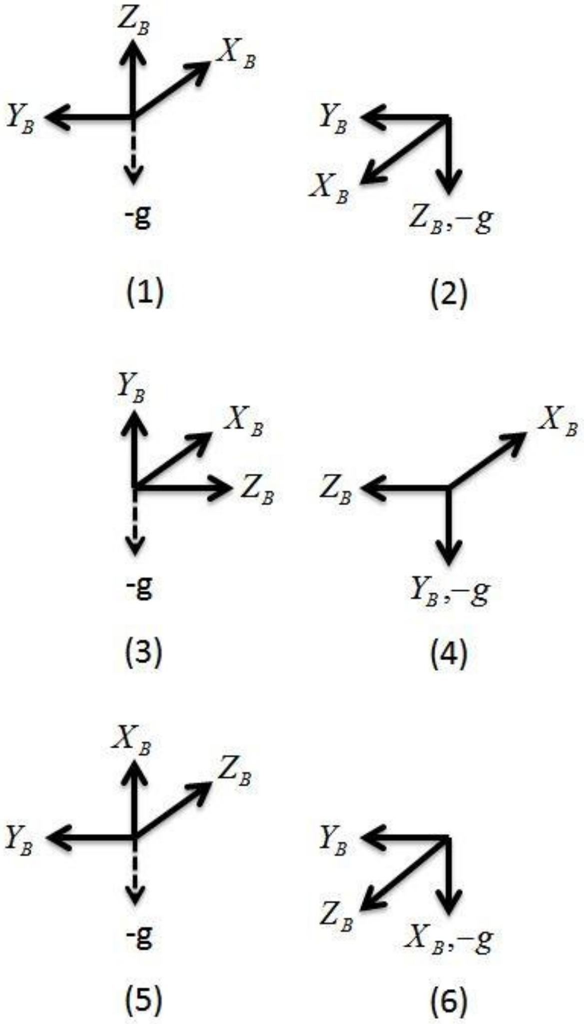

Figure A.2: Six positions in the body coordinate frame {*B*}

The precision motor rotary stages shown in Figure A.1 are used to achieve these positions accurately. The sensor module is leveled using a digital level having an accuracy of 0.1^0.

Table A.1: The ideal accelerations in the body coordinate frame in six positions in units of g

Position	$a_{g,x}$	$a_{g,y}$	$a_{g,z}$
1	0	0	1
2	0	0	-1
3	0	1	0
4	0	-1	0
5	1	0	0
6	-1	0	0

For each position, the ideal accelerations (in units of g) can be written as:

$$\tilde{a}_{g,1} = \begin{bmatrix} 0 \\ 0 \\ 1 \end{bmatrix}; \quad \tilde{a}_{g,2} = \begin{bmatrix} 0 \\ 0 \\ -1 \end{bmatrix}; \quad \tilde{a}_{g,3} = \begin{bmatrix} 0 \\ 1 \\ 0 \end{bmatrix}; \quad \tilde{a}_{g,4} = \begin{bmatrix} 0 \\ -1 \\ 0 \end{bmatrix}; \quad \tilde{a}_{g,5} = \begin{bmatrix} 1 \\ 0 \\ 0 \end{bmatrix}; \quad \tilde{a}_{g,6} = \begin{bmatrix} -1 \\ 0 \\ 0 \end{bmatrix}$$

A matrix (A_g) containing the six vectors of ideal accelerations is formed such that:

$$A_g = \begin{bmatrix} \tilde{a}_{g,1} & \tilde{a}_{g,2} & \tilde{a}_{g,3} & \tilde{a}_{g,4} & \tilde{a}_{g,5} & \tilde{a}_{g,6} \\ 1 & 1 & 1 & 1 & 1 & 1 \end{bmatrix} \tag{A.6}$$

At each position, the raw output of the tri-axial accelerometer is measured for 10s at a sampling frequency of 500 Hz. Then, the data for each axis is averaged and stored in a vector. The six vectors containing the averaged raw output of the tri-axial accelerometer at six positions can be written as:

$$a_{v,1} = \begin{bmatrix} a_{v,x,1} \\ a_{v,y,1} \\ a_{v,z,1} \end{bmatrix}; \; a_{v,2} = \begin{bmatrix} a_{v,x,2} \\ a_{v,y,2} \\ a_{v,z,2} \end{bmatrix}; \; a_{v,3} = \begin{bmatrix} a_{v,x,3} \\ a_{v,y,3} \\ a_{v,z,3} \end{bmatrix}; \; a_{v,4} = \begin{bmatrix} a_{v,x,4} \\ a_{v,y,4} \\ a_{v,z,4} \end{bmatrix}; \; a_{v,5} = \begin{bmatrix} a_{v,x,5} \\ a_{v,y,5} \\ a_{v,z,5} \end{bmatrix}; \; a_{v,6} = \begin{bmatrix} a_{v,x,6} \\ a_{v,y,6} \\ a_{v,z,6} \end{bmatrix}$$

A matrix (A_v), containing these six vectors, is formed such that:

$$A_v = \begin{bmatrix} a_{v,1} & a_{v,2} & a_{v,3} & a_{v,4} & a_{v,5} & a_{v,6} \end{bmatrix} \tag{A.7}$$

The matrix M is obtained by least-squares method:

$$M = A_v . A_g^T . (A_g A_g^T)^{-1} \tag{A.8}$$

With the knowledge of the matrix M, the acceleration measured by the tri-axial accelerometer a_v (in volts), at any instant of time, can be converted to y_a (in units of m/s^2) using the equation A.1 and A.3.

The normalized acceleration vector (${}^{B}A_n$) is obtained using the acceleration in the units of g ($y_{a,g}$). Since the vector, $y_{a,g}$ is composed of the acceleration in the units of g, ${}^{B}A_n$ simply limits the upper limit to +1 and lower limit to -1 for each element of the vector, $y_{a,g}$.

The gyroscope has been modeled as shown in the following equation:

$$y_g = \omega + \tilde{b} \tag{A.9}$$

where $y_g = [{}^{G1}y_{g,x} \quad {}^{G1}y_{g,y} \quad {}^{G2}y_{g,z}]^T$ is a vector containing the gyro rates measured by the gyroscopes (in rad/s), $\omega = [\omega_x \quad \omega_y \quad \omega_z]^T$ is a vector containing the angular velocities (in rad/s) and $\tilde{b} = [\tilde{b}_x \quad \tilde{b}_y \quad \tilde{b}_z]^T$ is a vector containing the gyro biases (in rad/s). The raw output of the gyroscopes can be written in a vector form as:

$$y_{g,v} = \begin{bmatrix} y_{g,v,x} \\ y_{g,v,y} \\ y_{g,v,z} \end{bmatrix} \tag{A.10}$$

The sensitivity of the gyroscopes (s_g) can be written as:

$$s_g = \begin{bmatrix} s_{g,x} \\ s_{g,y} \\ s_{g,z} \end{bmatrix} \tag{A.11}$$

The elements of y_g are calculated using the following equation:

$$y_{g,i} = \frac{y_{g,v,i}}{s_{g,i}} \tag{A.12}$$

where $i = x, y$ and z. The initial bias of the gyroscopes b_0 (in rad/s) can be written as:

$$b_0 = \begin{bmatrix} b_{0,x} \\ b_{0,y} \\ b_{0,z} \end{bmatrix} \tag{A.13}$$

The aim of the calibration process for gyroscopes is to find the six unknowns - gyro bias (b_0) and the sensitivity (s_g) of the three axes. The initial bias of the gyroscopes $b_{v,0}$ (in volt) can be written as:

$$b_{0,v} = \begin{bmatrix} b_{0,v,x} \\ b_{0,v,y} \\ b_{0,v,z} \end{bmatrix} \tag{A.14}$$

The raw output of the two axes of the dual-axis gyroscope, IDG 500 and the raw output of the gyroscope, MLX90609 are recorded at a sampling frequency of 500 Hz by keeping the IMU idle for 10s. The data of each axis is then averaged and stored in the vector, $b_{0,v}$.

Each element of the vector, s_g, is calculated by rotating the sensor module about the corresponding axis by known angular velocity (ω_{known}) using the rotary stages for 10s and recording the raw output of the corresponding axis of the gyroscope. The data is then averaged ($y'_{g,v}$) and the sensitivity of that axis is calculated using the following equation:

$$s_{g,i} = \frac{y'_{g,v,i} - b_{0,v,i}}{\omega_{known,i}} \tag{A.15}$$

where $i = x, y$ and z. The initial bias (in rad/s) is obtained using the following equation:

$$b_{0,i} = \frac{b_{0,v,i}}{s_{g,i}} \tag{A.16}$$

Curriculum Vitae

Name	Abhijit Saxena
Education	The University of Western Ontario London, Ontario, Canada M.E.Sc. (Electrical and Computer Engineering) 2009-2012
	The University of Pune Pune, India B.E. (Mechanical Engineering) 2005-2009
Work Experience	Research Assistant Canadian Surgical Technologies & Advanced Robotics London, Ontario, Canada 2009-2012
	Teaching Assistant The University of Western Ontario London, Ontario, Canada 2010-2011
	Research Trainee Defense Institute of Advanced Technologies Pune, India 2008-2009
	Engineering Intern Whirlybird Electronics Ltd. Kanpur, India 2006-2006